
Angelina Orthacker, BSc

**Focused Ion Beam Processing of
Polymers: The Influence of Material
Properties**

MASTER THESIS

For obtaining the academic degree
Diplom-Ingenieurin

Master Programme of
Technical Physics



Graz University of Technology

Supervisor:

Ao.-Univ.-Prof. Dipl.-Ing. Dr. techn. Ferdinand Hofer

Co-Supervisor:

Dipl.-Ing. Dr. techn. Harald Plank

Institute of Electron Microscopy and Nanoanalysis

Graz, May 2013

Abstract

The focused ion beam (FIB) microscope enables 3D surface structuring with spatial nanometer resolution and therefore has attracted increasing attention as a rapid prototyping tool. However, when combined with soft matter, such as polymers or biological materials, morphological instabilities and severe chemical damage are often observed results. A detailed look at typically used processing strategies reveals a technically induced heating component, which can be eliminated by an alternative patterning process. To demonstrate this effect different polymers (PP, HDPE, PMMA, PEG and EVA) have been investigated in dependence on processing parameters and patterning strategies.

Methods treating not only physical but also chemical behaviour were used, including scanning electron microscopy, atomic force microscopy, Raman spectroscopy and simultaneous thermal analysis. These investigations revealed not only a difference in removal rates, that could not simply be related to thermodynamic quantities of the materials, but also showed very different morphological behaviour when processed with the ion beam. We found, that the investigated materials could roughly be divided in two classes: polymers that would mainly undergo cross-linking when exposed to thermal stress, and others that would rather react by chain scission under the same conditions. This kind of reaction to thermal stress has a great influence on the structures received when patterning.

A variety of patterning strategies was used to follow the evolution of morphological instabilities and chemical degradation and to confine the origin of the different polymer behaviour. Complementary simulations of the same patterning strategies revealed good agreement with the experimental results and supported the main hypothesis of the study.

It was demonstrated that the alternative patterning strategy mentioned above stabilizes the patterning process for all investigated polymers. Therefore, a software was created, that can apply the alternative patterning strategy to any pattern. It represents the first step to make the alternative patterning strategy easily applicable.

Kurzfassung

Das Focused-Ion-Beam Mikroskop ermöglicht die 3D Strukturierung von Oberflächen mit räumlichen Auflösungen im Nanometer-Bereich und hat dadurch zunehmend Aufmerksamkeit als Instrument zur schnellen Prototypenentwicklung erlangt. Allerdings treten in Kombination mit weichen Materialien, etwa Polymere oder biologische Materialien, oft morphologische Instabilitäten und starke chemische Schädigungen auf. Eine detaillierte Betrachtung der typischerweise verwendeten Prozessierungsstrategien zeigt eine technisch induzierte Temperaturkomponente auf, die durch einen alternativen Strukturierungsprozess eliminiert werden kann. Um diesen Effekt zu demonstrieren wurden verschiedene Polymere (PP, HDPE, PMMA, PEG und EVA) in Abhängigkeit von Prozessierungsparametern und Abtaststrategien untersucht.

Zur Untersuchung des physikalischen und chemischen Verhaltens wurden Rasterelektronenmikroskopie, Rasterkraftmikroskopie, Raman-Spektroskopie und simultane thermische Analyse eingesetzt. Diese Untersuchungen zeigten nicht nur unterschiedliche Abtragraten, die nicht mit thermodynamischen Größen korreliert werden konnten, sondern auch unterschiedliches morphologisches Verhalten, welches bei der Prozessierung mit dem fokussierten Ionenstrahl auftritt. Es zeigte sich, dass die untersuchten Materialien grob in zwei Klassen aufgeteilt werden können, je nachdem, ob durch die thermische Belastung in der Umgebung des Ionenstrahls eher Quervernetzung oder Kettenspaltung auftritt, was großen Einfluss auf die resultierenden Strukturen hat.

Es wurde eine Vielzahl an Abtastmöglichkeiten verwendet um, die Evolution der morphologischen Instabilitäten und der chemischen Degradation zu verfolgen und den Ursprung des unterschiedlichen Verhaltens der Polymere einzugrenzen. Simulationen der verwendeten Strukturierungsstrategien zeigten sehr gute Übereinstimmung mit den experimentellen Ergebnissen und unterstützten die Hypothese dieser Untersuchung.

Es konnte gezeigt werden, dass die oben erwähnte alternative Strukturierungsstrategie bei den untersuchten Polymeren den Strukturierungsprozess für Polymere stabilisiert. Aus diesem Grund wurde eine Software entwickelt, welche diese alternative Abtaststrategie auf jedes beliebige Muster anwenden kann. Damit legt diese Arbeit den ersten Schritt, um diese alternative Strukturierungsstrategie einfach anwendbar zu machen.

Acknowledgements

First I would like to thank **Prof. Ferdinand Hofer** as head of the institute for giving me the chance to do my master thesis at his institute. I would also like to thank him for his support and being my supervisor.

My greatest thanks go to **Dr. Harald Plank** for his incredible support, his great ideas and the encouragement. I would like to thank him for teaching me, for taking his time, for being patient and for caring. I'd also like to thank him for accepting me in his work group and giving me the chance to be part of such an exciting project.

I want to express my appreciation to **DI Roland Schmied**, who also taught me a lot, took his time and always offered a helping hand. I'm very grateful for the Raman measurements and simulations he performed.

My gratitude also goes to **Dr. Boril Chernev** for performing the Raman measurements.

I'd also like to thank **Dr. Karin Wewerka, Claudia Mayrhofer, Sebastian Rauch, Martina Dienstleder, Manuel Paller** and the **lab crew** for advice and sample preparation.

Robert Winkler prepared the stream files and I want to thank him for that.

Prof. Gregor Trimmel and **Josefine Hobisch** performed the STA measurements and therefore I would like to express my gratitude to them.

I would like to thank **DI Thomas Ganner** for being such a pleasant office mate and being so helpful.

I also want to express my appreciation to all the other **FELMI staff members** for help and advice.

With **my colleagues and friends at the institute** I have spent some really good times, which I am deeply grateful for. We experienced some very special moments I will remember a lifetime. Enjoying lunch together has been real pleasure, which has made me feel at home.

I also want to thank my **fellow students** for the fun we had together and for cooperatively working and studying together. I will remember those years as a student as a good time, because of them.

I want to express my deepest appreciation to **the people I am closest with**. I feel the strong need to thank **my parents, my boyfriend, my family and my closest friends** for the unquestioning love they allow me to experience and for standing by me, when life shows its rougher sides. I'm also deeply grateful for all those little things they do for me, day after day and for the happy moments we have spent together.

Table of Contents

1	Introduction.....	7
2	Instrumentation	9
2.1	Dual Beam Microscope (DBM)	9
2.1.1	Basic Concept.....	9
2.1.2	Dual Beam Microscope (DBM) Setup and Eucentric Height.....	11
2.1.3	Scanning Electron Microscope (SEM)	11
2.1.4	Electron Source and Lenses	12
2.1.5	Electron – Matter Interaction and Detection	13
2.1.6	Image Formation and Magnification	14
2.1.7	Ion Beam Column	15
2.1.8	Axial Astigmatism	16
2.1.9	Ion beam – Matter Interaction and Detection	17
2.1.10	Variable Temperature Stage (VTS).....	20
2.1.11	Patterning Parameters and Classical Strategies.....	20
2.1.12	Beam Damage in Sensitive Materials.....	21
2.1.13	Previous Work at the FELMI: An Alternative Patterning Approach	22
2.2	Atomic Force Microscopy (AFM).....	28
2.2.1	Technical Setup.....	28
2.2.2	Motion System.....	28
2.2.3	Detection Systems	29
2.2.4	Cantilever and Tip.....	29
2.2.5	Functionality / Basic Principle.....	30
2.2.6	Tapping Mode.....	32
2.3	Raman Spectroscopy	33
2.4	Differential Scanning Calorimetry (DSC) and Thermogravimetric Analyses (TGA)	33
3	Materials.....	34
3.1	Damage.....	34
3.1.1	Thermally Assisted Degradation (Pyrolysis)	34
3.1.2	Degradation due to High Energy Radiation	35
3.2	GEL - SOL.....	36
3.3	Soft Matter	37
3.4	Materials Used	38

3.4.1	Poly(Methyl MethAcrylate) (PMMA).....	38
3.4.2	High Density PolyEthylene (HDPE).....	39
3.4.3	PolyPropylene (PP)	40
3.4.4	PolyEthylene Glycol (PEG)	41
3.4.5	Ethylene Vinyl Acetate (EVA).....	43
4	Experiments and Results	45
4.1	Correlation 1 – Thermodynamic Properties as Key Element	46
4.1.1	Introduction	46
4.1.2	Removal Rate (RR) Experiments	46
4.1.3	Chemical Damage	56
4.1.4	Simultaneous Thermal Analysis (STA)	57
4.1.5	Process Parameter to Material Property Relationships	59
4.1.6	Special Details.....	61
4.2	Correlation 2 – Chemical Processes as Major Influence	65
4.2.1	Introduction.....	65
4.2.2	Formulation of the Hypothesis.....	66
4.2.3	FIB Parameter Variation	69
4.2.4	Material Creeping.....	72
4.2.5	Further Experiments at the Dual Beam Microscope	77
4.2.6	Raman and STA.....	82
4.2.7	Second Conclusion – Chemical Processes as Major Influence	83
4.3	The SIL-Engine	85
5	Summary and Outlook.....	90
6	Appendix.....	93
6.1	Appendix 1 - Matlab Code of the SIL-Engine - Bitmap Version.....	93
6.2	Appendix 2 - Matlab Code of the SIL-Engine - Stream File Version	97

List of Abbreviations

AFM	...	<i>atomic force microscope</i>	PoP	...	<i>point pitch</i>
BSE	...	<i>back scattered electrons</i>	PP	...	<i>polypropylene</i>
CDT	...	<i>critical dwell time</i>	PR 1, 2, 3	...	<i>patterning regime 1, 2, 3</i>
CL	...	<i>cross-linking</i>	PSD	...	<i>position sensitive detector</i>
CPoP	...	<i>critical point pitch</i>	PTFE	...	<i>polytetrafluorethylene</i>
CR	...	<i>critical radius</i>	RR	...	<i>removal rate</i>
CRT	...	<i>critical refresh time</i>	RT	...	<i>refresh time</i>
CTR	...	<i>critical refresh time</i>	RTC	...	<i>refresh time condition</i>
DBM	...	<i>dual beam microscope</i>	SC	...	<i>scission</i>
DSC	...	<i>differential scanning calorimetry</i>	SE	...	<i>secondary electrons</i>
DT	...	<i>dwell time</i>	SEM	...	<i>scanning electron microscopy</i>
ETD	...	<i>Everhardt Thornley detector</i>	SIL	...	<i>smart interlacing</i>
EVA	...	<i>ethylene vinyl acetate</i>	STA	...	<i>simultaneous thermal analysis</i>
FE	...	<i>finite element</i>	STET	...	<i>specific total exposure time</i>
FEG	...	<i>field emission gun</i>	TEM	...	<i>transmission electron microscopy</i>
FIB	...	<i>focused ion beam</i>	TET	...	<i>total exposure time</i>
HDPE	...	<i>highly-dense polyethylene</i>	TGA	...	<i>thermogravimetric analysis</i>
IL	...	<i>interlacing</i>	TLD	...	<i>through the lens detector</i>
ILD	...	<i>interlacing distance</i>	UHV	...	<i>ultra high vacuum</i>
LIMS	...	<i>liquid ion metal source</i>	VT	...	<i>volatizing threshold</i>
MP	...	<i>melting point</i>	VTS	...	<i>variable temperature stage</i>
PE	...	<i>polyethylene</i>	VY	...	<i>variable Y</i>
PEG	...	<i>Polyethylene glycol</i>	ZZ	...	<i>zigzag</i>
PMMA	...	<i>poly-methylmethacrylate</i>			

1 Introduction

Organic materials have become more and more important in everyday life during the last decade. On the one hand we are all familiar with commodity plastics, which we encounter in our daily life. We permanently are confronted with polymers, no matter whether we think about food packaging, clothing, automotive applications or electronic housings. But on the other hand, polymers have also reached us in less obvious forms, far better hidden, like for example in the organic-LED displays of our smartphones. Due to the possibility to use polymers to create flexible devices a wide variety of applications is conceivable, which could give our world a whole new appearance and possibilities. First steps into that direction have already been taken, for example through the existence of rollable displays. Other great advantage of organic materials are that they can be used to create transparent electronics, or that they can be processed by printing. Due to all those reasons, and more, organic substances have made their way from macroscopic applications to microscopic components in the high-tech industry. In our modern world, devices are getting smaller, and smaller. Therefore also the need to investigate those materials on a far smaller length scale has arisen, moving from the micro to the nanometer range.

A very useful tool to conduct manifold investigations in the nanometer range, reaching from analysis to prototyping is the dual beam microscope (DBM), which is a combination of a focused ion beam microscope (FIB) and a scanning electron microscope (SEM). This on the one hand unifies the advantages of both microscopes within one, and on the other hand enables to use the electron beam to observe FIB patterning processes in-situ. This for example enables its use as a site specific preparation tool for ultrathin lamellas suitable for transmission electron microscopy on the atomic scale, which are often used for analysis in the classical semiconductor industry.

But the DBM also attracts more and more attention as a direct-write rapid prototyping tool. Its use is versatile due to the fact that both subtractive structuring through sputtering and positive structuring using precursor gases are possible in the nanometer range. The patterning engine, which allows the loading of stream files and bitmaps, enables the fabrication of nearly any structure, even in 3D and on non-flat surfaces, which is a clear advantage compared to lithography. Another indisputable benefit is that the process is a direct-write process and therefore maskless in contrast to resist based techniques. That implies that the operator has the possibility to repeatedly experiment with different patterns without further preparation steps.

While this technique is well established in the classical semiconductor industry, it has always been considered problematic in combination with soft matter such as polymers and biological materials. These materials are complicated due to a combination of low thermal conductivities and low melting points, which results in the heat not being transported away from the structured areas fast enough to avoid severe chemical and morphological instabilities. As these materials are not only interesting to investigate, but also have become more and more important in industry during the last decade, as described above, the motivation to investigate this subject further seems justified.

Preliminary studies performed at FELMI, conducted by Harald Plank and Roland Schmied, have shown that there is a technically induced heating component, which can be strongly reduced by using an alternative patterning procedure – the interlacing strategy. The materials investigated previously were mainly polypropylene (PP) but also high density polyethylene (HDPE). As the results of this study were extremely promising, the motivation to expand the investigation to even more

challenging materials with lower melting points, and to gain a better understanding of the interplay of material properties and processing parameters, was tremendous, which is the aim of this master thesis. Additionally to the above mentioned polymers PP and HDPE, the study was expanded by the use of poly(methyl methacrylate) (PMMA), commonly known as acrylic glass, poly(ethylene glycol) (PEG), which is often used in medical contexts and two versions of ethylene vinyl acetate (EVA), with different VA contents. With this choice of materials we went to melting points as low as 65°C for PEG. The materials also ranged from highly crystalline (PEG), to amorphous (PMMA). What proved to be a very important characteristic was the chemical reaction of those polymers to high energy radiation and the heat that accumulates in the beam proximity. Based on these findings a strongly improved patterning approach has been developed which compensates for the drawbacks.

As even extremely challenging samples were subject of this investigation, a successful patterning of those materials makes a whole new range of applications conceivable. Next to the use on polymers, also applications for biomaterials might be possible in future.

2 Instrumentation

2.1 Dual Beam Microscope (DBM)

2.1.1 Basic Concept

In general a focused ion beam (**FIB**) microscope works in a very similar way to a scanning electron microscope (**SEM**): it's got a particle source, a lens system, deflection coils and a number of different detectors. The biggest difference of an ion beam microscope lies in the interaction with the sample, which is mostly subtractive via material removal which is called sputtering. The possibility to position the beam, which can have a diameter smaller than 7 nm, very accurately, and to control the pulse duration of single points, enable the use of this microscope as a nano scalpel, as shown in Figure 1 by a FIB structured gold layer on SiO₂.

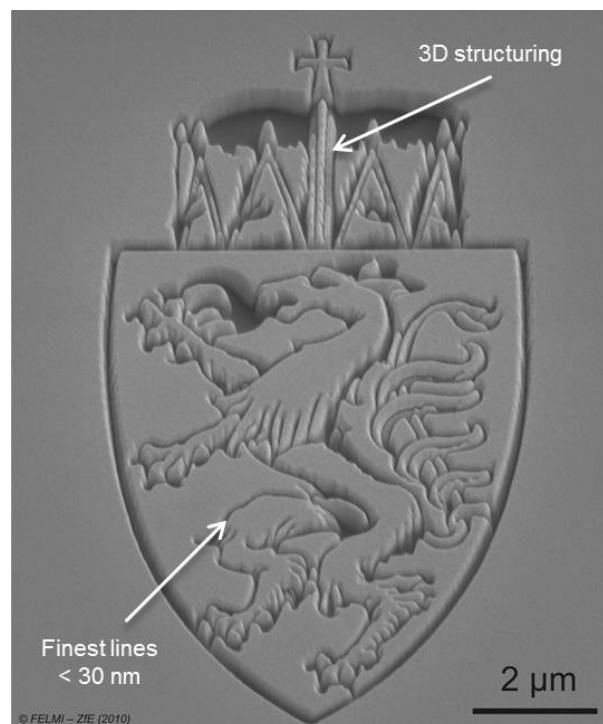


Figure 1: example for the FIB used as a nano scalpel: FIB based ion milling of a gold film on SiO₂ including 3D structures (centre parts of the crown) and very fine lines with widths below 30 nm [1, 2, 3, 4].

Another unique application is the site-specific analysis beneath the surface as can be seen in Figure 2a. That way defect analysis can easily be conducted and even 3D material distribution can be extracted via such instruments (see Figure 2b for the strategy and a 3D reconstruction in c). The most used application of FIB microscopes, however, is the site specific preparation of ultrathin lamellas (< 50 nm) which can be directly used for transmission electron microscopy (**TEM**) as representatively shown in Figure 2 by a TEM lamella front (d) and top view (e). The FIB microscope also enables the fabrication of positive nano structures, through the use of precursor gases, which are chemically decomposed during the interaction with the particles of the beam and thereby immobilized locally where the beam has been placed [4]. An example is shown in Figure 2f by a 3D structuring on a non-flat surface. Due to the possibility to structure very complex patterns with high spatial resolution on

even non-flat surfaces and adapt the process parameters rapidly towards ideal results, such instruments represent direct-write rapid prototyping tools for science and technology.

By that modern FIB microscopes have reached the status of nano-laboratories with partly unique possibilities, which makes them an essential component of modern science.

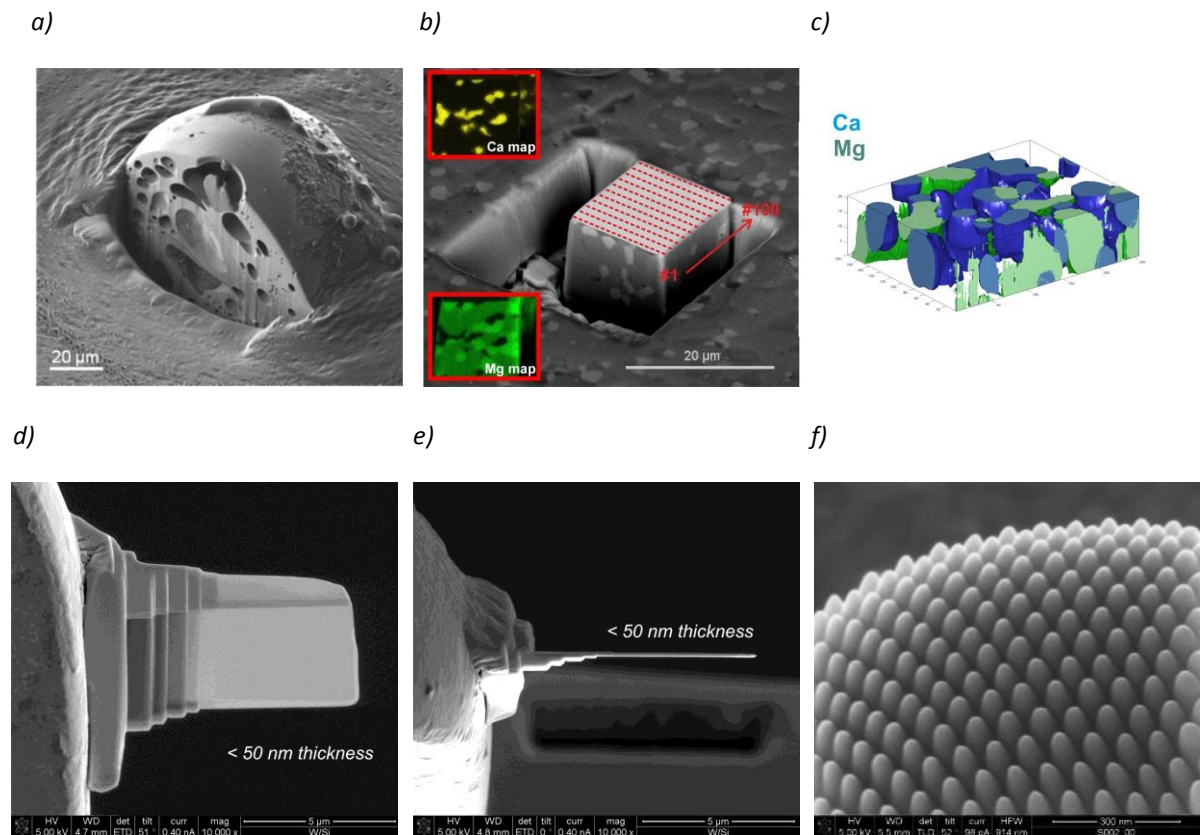


Figure 2: a) FIB cross section of a particle for sub-surface failure analysis; b) FIB based slice and view complemented via analytical elemental mapping analyses which allow 3D reconstruction of material distribution (c); d) FIB based fabrication of a TEM lamella in front and top view (e); f) particle induced 3D deposition of Pt on a non-flat surface [5,2].

To enhance the functionality of FIB microscopes, modern setups (like the one used during the course of this thesis) usually have an additional SEM installed, which makes the whole apparatus a dual beam microscope (**DBM**), shown in Figure 3a. The two columns are installed at an angle of 52° relative to each other. Therefore the two particle beams meet in a special point, which is called the eucentric height (see Figure 3b). If the sample is positioned in that height, it is possible to observe FIB based procedures simultaneously with the electron beam. Thus, critical actions can be adjusted or stopped.

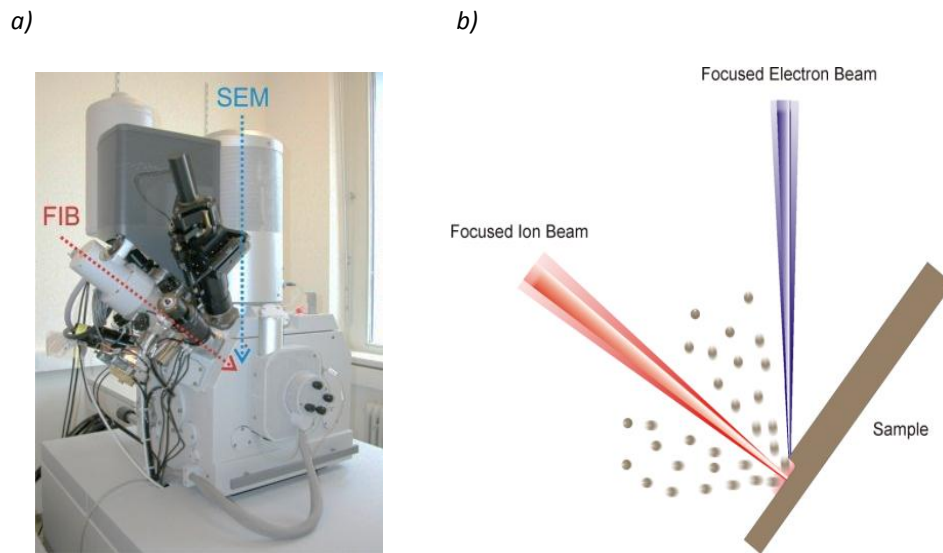


Figure 3: the dual beam microscope (a) and the basic concept of simultaneous dual beam processing (b) in the eucentric sample height.

2.1.2 Dual Beam Microscope (DBM) Setup and Eucentric Height

As described in section 2.1.1, modern dual beam microscopes consist of two individual microscopes by means of a SEM and a FIB microscope (see Figure 3). A special sample position in such dual beam microscopes (DBM) is the eucentric height. This height is the distance at which the electron beam and the ion beam work cooperatively in the same position (see Figure 3). This is important for various reasons, like SEM guided positioning of the ion beam or for simultaneous SEM imaging during FIB processing. Furthermore, the additional equipment like the gas injection systems or the micromanipulator is aligned according to the eucentric height which makes this position essential for ideal DBM processing. While FIB processing requires the eucentric height in any case, SEM imaging can also be done on larger or shorter distances for improved overview and high resolution imaging, respectively. For the microscope used, the eucentric height is approximately 4.9 mm and 19.3 mm with respect to the electron column and the ion column, respectively. Furthermore, in the eucentric height, a point in the SEM / FIB image will not move while the sample stage tilts. The eucentric height therefore can be found by selecting a distinct point on the sample, moving it to the centre of the electron beam image, tilting the stage while watching the live image (in which the distinct point will move up or down, unless the feature is already in the eucentric height) and then changing the z-coordinate manually, until this specific point is in the centre of the image again.

2.1.3 Scanning Electron Microscope (SEM)

Due to the short wavelengths of electrons [6,7] the SEM can achieve very high resolutions (down to about 5Å). The resolution powers of different kinds of microscopes are given in Figure 4. A SEM provides a fast way of overview inspection and allows morphological and analytical characterization in very short time. For classical high vacuum SEMs, the only demands are a conductive sample (or at least such coating), the vacuum compatibility and the suitability to inspect the sample via electrons. All SEMs consist of an electron source, electron lenses, and detectors which are described only briefly in the following sections since manifold literature is available for a detailed explanation.

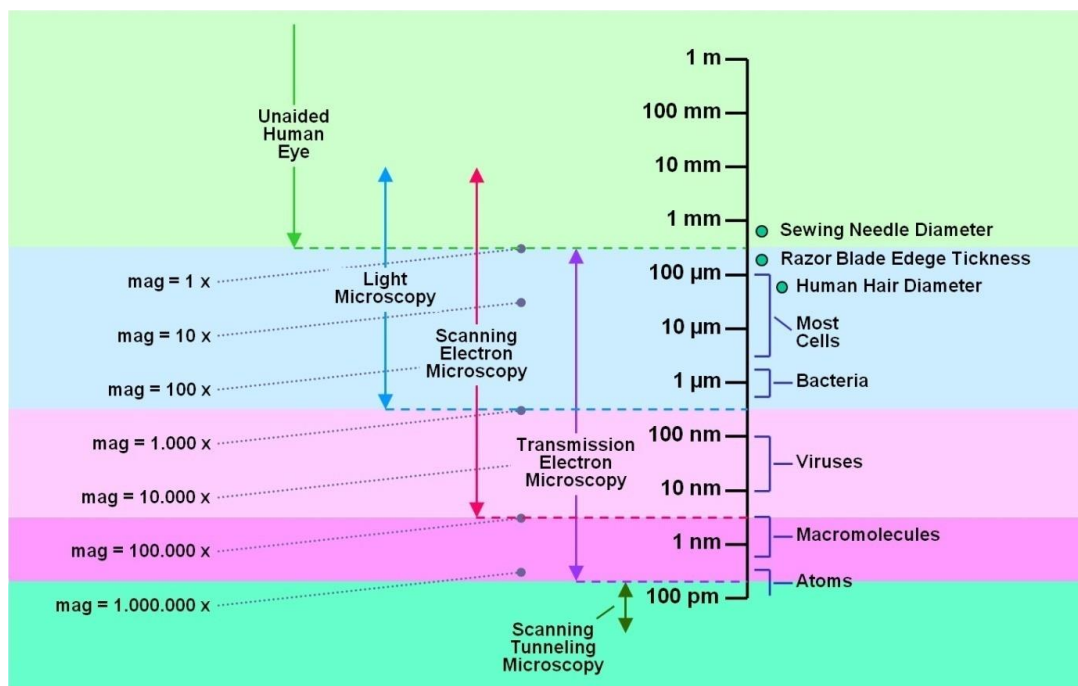


Figure 4: magnification ranges and resolution powers of different types of microscopes [1].

2.1.4 Electron Source and Lenses

The SEM in the used DBM is equipped with a field emission gun (**FEG**), which is kept in ultrahigh vacuum (**UHV**) conditions. The electrons are emitted at the end of a fine, heated tungsten tip, placed in a strong electric field, which makes the electrons tunnel through the strongly curved metal tip [6,7]. A so called Wehnelt cylinder bundles the electrons in the so called crossover which is then used as variable electron source for the SEM.

Then the electron beam is further accelerated to an energy of 30 keV and guided through two electromagnetic condenser lens systems (C1 and C2 in Figure 5), which make the beam smaller and align it parallel and central with respect to the optical main axis. These lens systems are also used to set electron beam current, which can be varied from 2 pA to 37000 pA by a varying acceptance area of the first crossover, explained before. After the C2 lens, the electron energy is adapted to the finally required beam energy (0.5 – 30 keV) and focused through an aperture. For a systematic rastering of the beam over the sample the beam is guided through two vertically arranged duplex-lenses (DC upper and DC lower in Figure 5), which allow a movement in X and Y direction. Those two lenses also compensate the axial astigmatism, which is an often encountered lens error and will be discussed later. The final lens the beam passes is the objective lens, which focusses the beam on the sample. A more detailed explanation of individual components, its function and limitation can be found in literature [6,7].

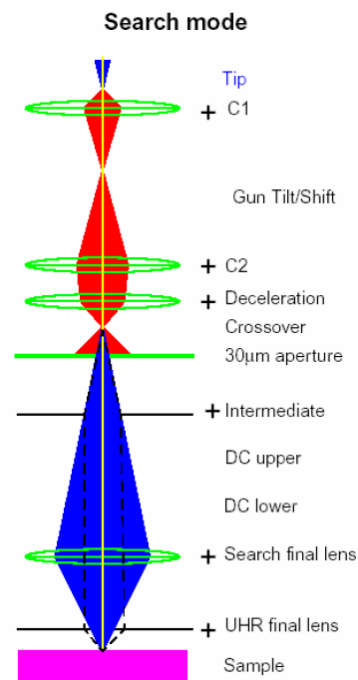


Figure 5: SEM lens system for the microscope used during this thesis (standard mode operation) [12].

2.1.5 Electron – Matter Interaction and Detection

Concerning the electron beam interaction with the sample we can basically differentiate between two possible forms of interaction: elastic and inelastic scattering. In both cases the direction of propagation is changed, which leads to a pear shaped volume of interaction displayed in Figure 6a via a Monte Carlo simulation [8]. Elastically scattered electrons don't lose energy during the interaction. The angle of deflection is typically large. They sometimes leave the sample again as back scattered electrons (**BSE**), which typically have a high energy. Inelastically scattered electrons (typically deflected in small angles) lose energy during the interaction, which can lead to a number of follow-up processes including the generation of phonons, the ionization of inner shells (again leading to characteristic X-rays and Auger electrons), and the generation of secondary electrons (**SE**).

The signals that are mostly used for detection are the characteristic X-rays (material identification), BSE and SE. An energy distribution of the detected electrons re-emitted from the surface is shown in Figure 6b. The detected SEs originate from a region close to the surface (only a few nm) as the ones from lower regions are not able to escape the surface due to their low energy (< 50 eV). Based on this spatial confinement, SEs provide best resolution and are therefore the most important electron species for the image formation.

The SEs are usually detected with the Everhart Thornley Detector (**ETD**). A positively biased cage attracts surface emitted SE and bundles them onto a scintillator. The signal is further enhanced by a photomultiplier. The fact the ETDs are typically mounted at a certain tilt angle and the low energy of the SE leads to the effect, that surfaces which face the detector give a higher signal. Therefore a kind of "shadow effect" can be seen, which gives the image 3D-character. By changing the cage voltage from positive to negative the ETD can be used to detect BSE (which are often used to get qualitative

material contrast), as the low energy SE are deflected away, while the energy of the BSE is too high to change their path.

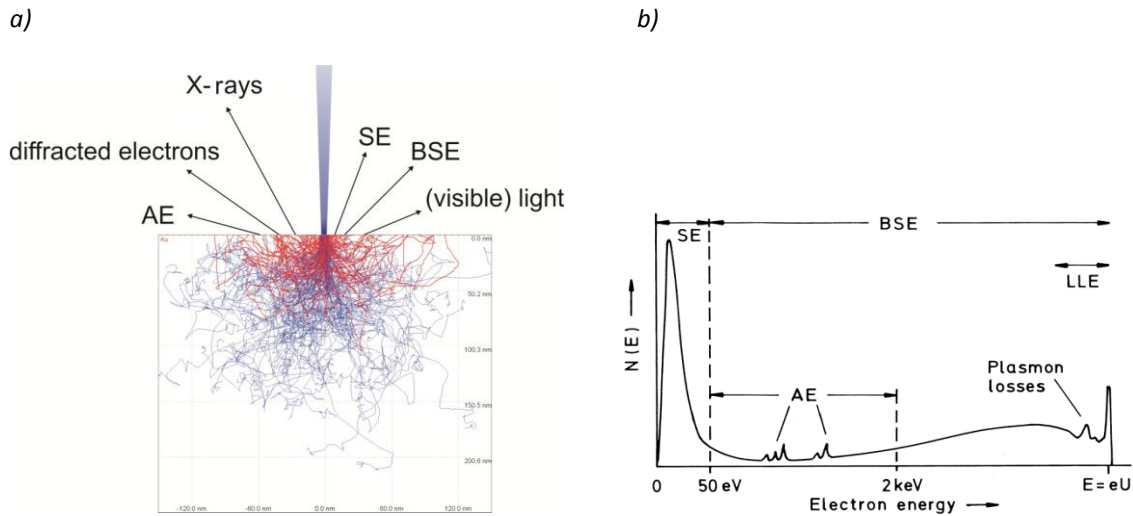


Figure 6: a) interaction of the electron beam with the sample visualized via Monte Carlo trajectory and interaction simulation; b) energy distribution of surface emitted electrons based on the primary energy E [8,1]

The used DBM is also equipped with a through the lens detector (**TLD**), which does not show shadowing effects as it is mounted straight above the sample. It is used for high resolution applications but often provides a lower efficiency due to a lower total collection angle.

Electron – matter interaction is a very complex topic and still not completely understood. A more detailed explanation including detector functionalities can be found in reference [6,7].

2.1.6 Image Formation and Magnification

To get an image of the surface the electron beam is systematically rastered over the sample surface. In every point the intensity of the emitted signal is stored and interpreted as intensity on the screen. At the end the image shows an intensity distribution of the surface based on the individually emitted signals due to the primary electron beam. If the signal is too weak, the pulse duration (dwell time) of each single point can be increased. But this can lead to drift problems due to local charging, or to material damage for (very) sensitive samples. Also the DBM software allows averaging approaches which combine a low single point exposure with high intensities via mathematical treatment. However, this method is also very sensitive to sample drifts. Finally, the ideal setting is an adapted dwell time in a single pass which has to be chosen accordingly by the operator.

To increase the magnification the rastered area is decreased by a reduction of the point to point distance (point pitch), while the number of pixels usually stays constant. The maximum meaningful magnification is finally defined by the beam diameter which should be considerably smaller than the image width.

The resolution is limited by lens focusing capabilities, various lens errors and the particle-matter interactions given by the sample itself. The one lens error which can usually be compensated by the

operator is the axial astigmatism and will be discussed in the section on the focused ion beam (section 3.1.2.2). For the other lens errors the reader is encouraged to use reference [6,7] for a detailed discussion.

2.1.7 Ion Beam Column

Most FIB microscopes, as well as the one used for this thesis, use Ga^+ ions, emitted from a liquid ion metal source (**LIMS**). A small reservoir filled with gallium is heated above the melting point of gallium (29.8 °C) in vacuum conditions, as displayed in Figure 7. In the liquid state it wets a hairpin made from tungsten. Through effects of the gravitational force a little droplet is formed at the end of the hairpin.

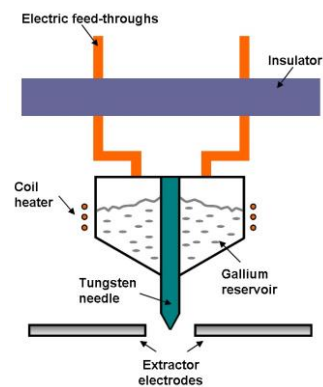


Figure 7: scheme of a liquid ion metal source (LIMS) [9].

Through the use of a special cylinder, the extractor (which has got a very high potential and field intensities of more than 10^8 V/cm), the droplet is shaped conically (Taylor cone), with a half angle of 49.3° and a final radius of only a few micrometers. Due to the high curvature at the end, the huge electric field and the ability of Ga to easily abandon valence electrons there is a highly localized emission of Ga^+ ions. The emitted ions are then guided through the beam acceptance aperture, which is situated above the condenser lens system (Figure 8). The condenser lens system adjusts the ion energies as specified by the user in a range of 5 kV to 30 kV and aligns the ion beam parallel and central with respect to the optical main axis. In the next step the ion beam current is adjusted, in a range of 1 to 20000 pA, by the beam defining aperture. The beam blanker, which is next in line, can blank the ion beam within sub-microseconds which is necessary because of the very destructive character of the ion beam. The last two lens systems again show combined functionality concerning scanning and stigmatism. Because of the higher particle masses and energies of the ions they are constructed as octopoles. The last lens is the objective lens, which focusses the ion beam on the sample.

Even though, historically seen, gallium was rather chosen as an ion source due to curiosity, but it has proven to be a good decision, for various reasons: due to its low melting point it can easily be liquefied. Its low vapour pressure enables easy ion emission, minimizes losses and therefore increases the lifetime of the source. Also it is not miscible with the tungsten tip and has is very stable in vacuum. A detailed description can be found in reference [10] or [11].

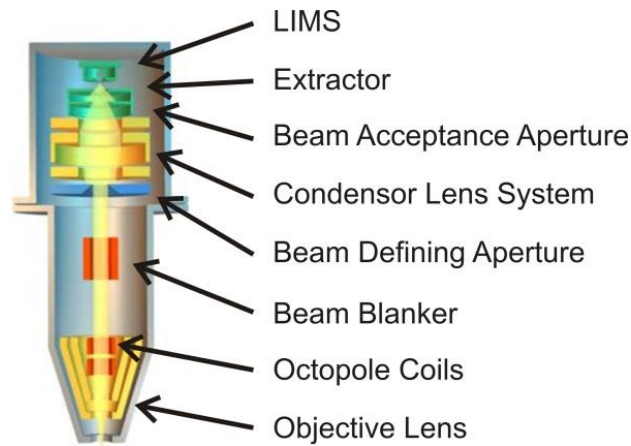


Figure 8: scheme of ion beam column for the used DBM [12].

2.1.8 Axial Astigmatism

Because the lenses never are perfect, for example there are deviations from the rotational symmetry, the electron beam is differently deflected depending on the position at the lens cross section. Resulting from that is a distortion of the beam which limits the resolution of the microscope. This is called axial astigmatism and shown in Figure 9 in principle (left), how it looks uncorrected (centre) and corrected (right).

This lens error can be compensated quite easily. The radial inhomogeneity's can be corrected with a special and dedicated lens system consisting of at least four poles. Such lens systems are built into all FIBs or SEMs.

In our case the compensation of this lens error was a very important issue since distorted beams lead to a different ion-per-nm² rate which finally has the same influence as a lower current and / or a defocused beam. Hence, prior to any structuring experiment, the beam has been carefully set up until no astigmatism could be observed.

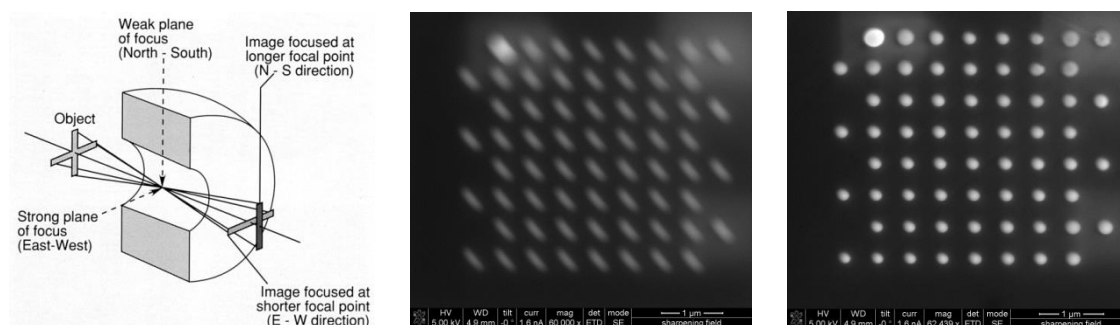


Figure 9: reason for the axial astigmatism schematically shown (left) and SEM images showing a strongly astigmatic (middle) and a corrected image (right).

2.1.9 Ion beam – Matter Interaction and Detection

While there are only little sputtering effects through electrons by means of knock on damage (material removal through the transfer of momentum), it is almost impossible to avoid damage, when the ion beam strikes the surface. This material removal through transfer of momentum is called sputtering and is the main mechanism of interaction during FIB processes. Next to the emission of atoms, ions and clusters a large number of SEs are emitted, which are used for image formation via the ETD or the TLD.

2.1.9.1 Direct Effects

Because Ga^+ ions are remarkably larger than electrons they cannot penetrate the sample as deep as electrons. Instead, collisions with atoms or molecules are inevitable. Together with the high energy of the incoming ions this leads to damage of the sample. Figure 10 displays the most important processes that occur due to the interaction with high energy Ga^+ ions. The distance the ions can move through the material undisturbed is material dependent but usually confined to a few nanometers. Afterwards atoms are removed from their positions due to inelastic collisions, which lead to a loss of energy and a change of propagation direction of the ion. As an example of the characteristic volume of interaction Figure 11 shows a simulation of 30 kV Ga^+ ions in silicon. Due to the size of the ions and the therefore high number of collisions per path length the total depth of penetration for 30 kV Ga^+ ions is less than 70 nm in Si while e.g. electrons of the same primary energy penetrate up to several μm .. After the primary ion lost all its kinetic energy, it stays in the sample and is permanently implanted. Within this interaction volume (see Figure 11) Ga implantation is intrinsically unavoidable and the sample material will be amorphous (in case of a crystalline material) and / or chemically degraded (in case of molecules) due to the inelastic interaction.

2.1.9.2 Indirect Effects

Atoms, ions or clusters, which have been displaced from their positions, can lead to different follow-up processes depending on their energy:

- Excitation of molecular vibrations (phonons), which can lead to an enormous increase of temperature. Simulations suggest that the local temperature can rise up to 2000°C. The lateral temperature distribution depends on the thermal conductivity of the samples used together with specific heat capacity and can range from about 5 nm to 500 nm. Therefore, considerable collateral damage can occur which is one of the main aspects in this thesis. An adaption of processing parameters is the only way to control and reduce enormous heating which will be shown during this master thesis.
- A large number of valence electron emission originating from neighbouring regions due to phonons and collision effects might be set free which corresponds to a large number of SE.
- Collision cascades which lead to amorphisation and chemical degradation.
- Re-emission of atoms, ions and clusters including SE emissions.

to handle with the FIB. Another problem is that their melting points are very low (typically below 300°C).

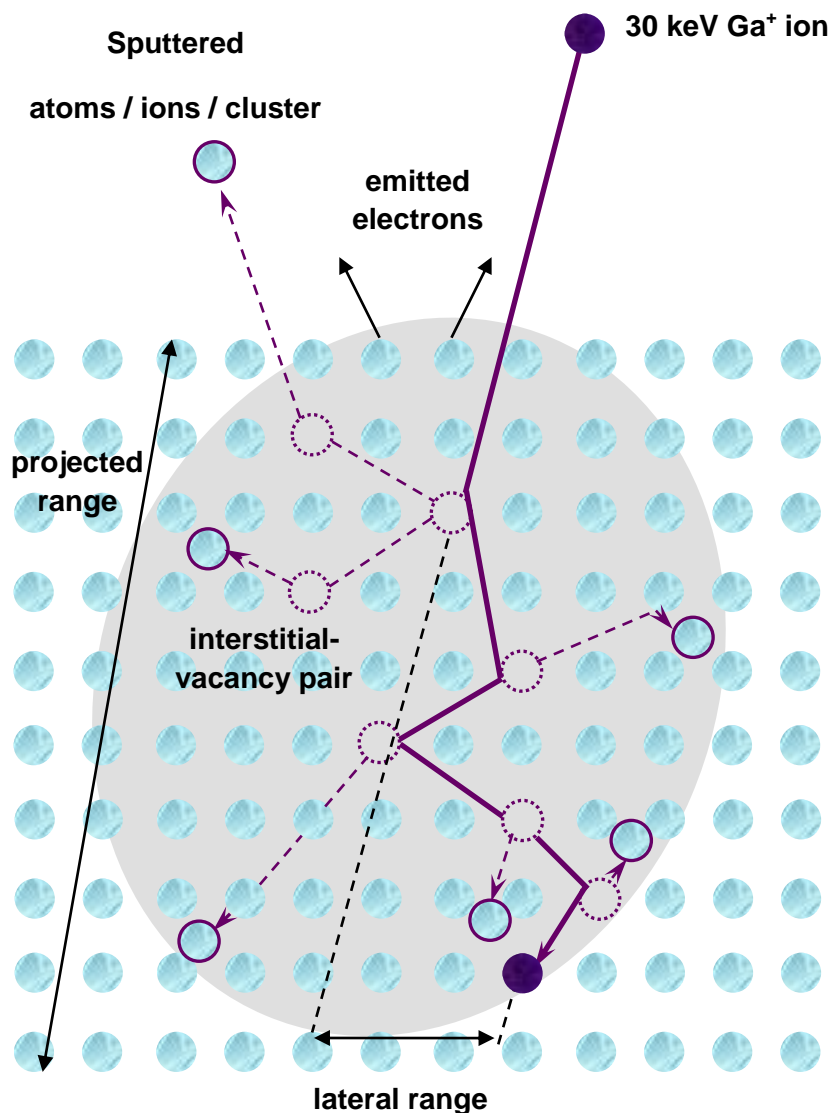


Figure 10: the effects of the ion beam interaction a follow-up processes [13].

The both last influences are mainly responsible for the material removal. They are supported through thermally induced evaporation in the vicinity of the beam due to heat accumulation in materials with low thermal conductivities. This is also the reason why polymers and biological samples are difficult to handle with the FIB. Another problem is that their melting points are very low (typically below 300°C).

The material removal is referred to as sputter rate and is strongly material dependent. It depends on the bond energies. In crystalline materials it is also dependent on the relative orientation of the crystal. Different crystalline zones show different sputter rates.

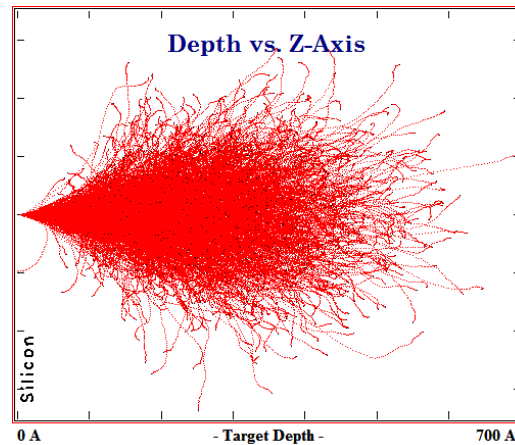


Figure 11: Monte Carlo simulation of 30 kV Ga⁺ ion trajectories in silicon [14].

Next to the already mentioned internal side effects like amorphisation or chemical degradation of the interaction volume (also at side walls), a rise in temperature and Ga⁺ implantation, there is also the external problem of redeposition. Material that has been sputtered accumulates again in the vicinity. On the one hand this can occur due to badly chosen processing parameters, as shown in Figure 12: while all structures have been exposed to the same ion dose in the same process time the two structures on the left show the desired shape, the structure on the right has no vertical side walls any more due to redeposition (single sputter process from top to bottom). Shorter dwell times or slightly larger point pitches can improve the situation dramatically [15]. On the other hand large aspect ratios (depth divided by width) are problematic, because the sputtered material cannot leave structures that are very narrow and very deep. This leads to an intrinsic limit of aspect ratios of about 5 to 10. Reduced ion beam currents and gas enhanced etching can lead to slight improvements.

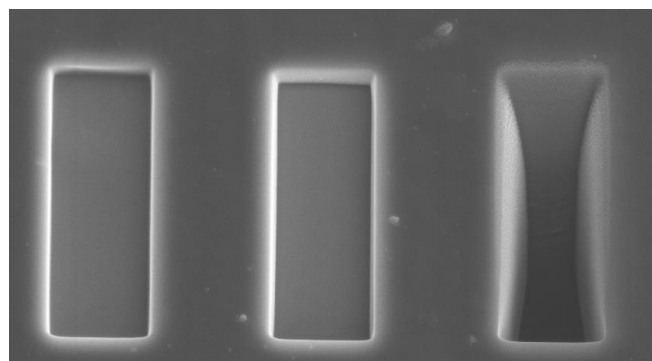


Figure 12: redeposition effects due to improper chosen processing parameters; from left to right the DT equal 10 μ s, 100 μ s and 1000 μ s while the total exposure times were constant for all patterns (pattern width was 2 μ m) [1].

The signal detected during FIB processing mainly consists of SE, but also atoms, ions and charged clusters can contribute to the signal. Special detectors allow furthermore the qualitative separation of different ion species similar to BSE detection for electrons. For this thesis, the FIB processing was always monitored via the ETD which mainly responds to surface emitted electrons.

A much more detailed description of ion-material interaction, its basic dependency on process parameters as well as detection can be found in reference [4, 10, 11].

2.1.10 Variable Temperature Stage (VTS)

The variable temperature stage (VTS) can be seen in Figure 13. When used for cooling a sensitive sample in order to keep thermal stress low liquid nitrogen is used as flow-through media with a constant overpressure of about 1 bar. The samples used need to be thin, especially for materials with low thermal conductivities, so that the cooling is sufficient in the structured areas, as low thermal conductivities imply that the heat can only be slowly transported away from the sample. The tubes providing the stage with the cold gas become stiff due to the low temperature, which can lead to mechanical problems when the stage is moved. In particular, a sample drift after positioning is often observed which reduces patterning accuracy. Therefore, to avoid such drift problems, one needs to wait for some time after moving the stage prior to patterning. Same holds for on-purpose variation of the sample temperature resulting in a tension on the tubes which can also cause the stage to move. Hence, after stage movements and / or on-purpose temperature changes, the final X / Y position should be checked together with the eucentric height. Taking into account that the installation / deinstallation of the VTS takes about 2 hours, the use of the VTS is economically very unfavourable, even though it can reduce the damage in sensitive samples. For biological materials where the water has to be kept inside, the VTS is an absolutely necessary add-on.

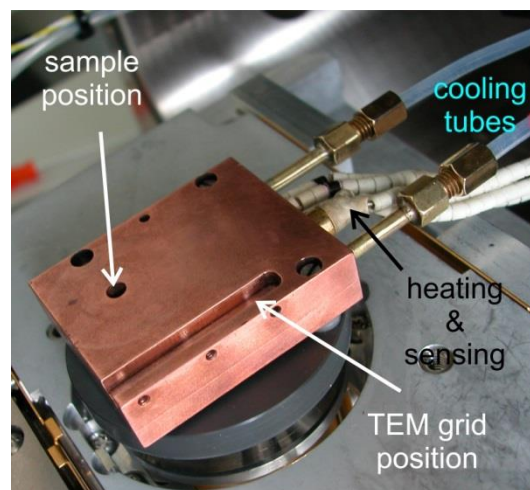


Figure 13: variable temperature stage (VTS) for the dual beam microscope which allows sample temperatures from $-150\text{ }^{\circ}\text{C}$ to $+100\text{ }^{\circ}\text{C}$ [1].

2.1.11 Patterning Parameters and Classical Strategies

In classical patterning the beam follows a consecutive sequence of discrete points. These are either arranged line by line, each line patterned from left to right (raster style), or the beam follows a serpentine pattern which is the standard patterning procedure in most DBM instruments. In this case the beam does not always follow the same direction when patterning, but moves in alternating directions, going from left to right and then from right to left again as schematically shown in Figure 14.

Patterning parameters that can easily be changed are the point pitch and the dwell time. The point pitch (**Pop**) is the distance between two (consecutive) patterning points addressed by the beam (see

Figure 14). The dwell time (**DT**) is the pulse duration for single points before moving on (see Figure 14). These parameters have a great influence on the resulting morphology and chemistry, especially for sensitive materials.

Another important and influential parameter is the refresh time (**RT**) which becomes relevant if the structure is not processed via a single but with multi passes of the same pattern. The RT is then given by the time until the beam patterns the same point again. The RT is of course dependent on the number of patterning points (via shape and size), the PoPs and the DTs used. For small pattern sizes, low dwell times, or large point pitches the RT can become very short which can be problematic in terms of sufficient local cooling before subsequent pulses. To avoid this the refresh time can artificially be increased by introducing a pause. However, such additional pause times can have unfavourable consequences such as very long process times which can also entail drift related issues. Finally the total exposure time (**TET**) is defined by the total time required for the pattern while the specific total exposure time (**STET**) is given by the total exposure time per single point which are very useful quantities for this thesis.

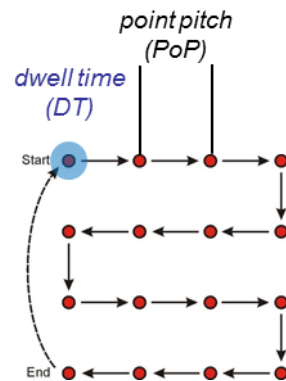


Figure 14: typically used patterning sequence represented by a serpentine patterning strategy. Such procedures are defined by their single pulse duration (dwell time - DT) and the distance in between two consecutive points (point pitch - PoP).

2.1.12 Beam Damage in Sensitive Materials

Beam damage as a general term has to be divided into two classes: **1)** particle – material related damage which is unavoidable and **2)** process related damage. The second influence in terms of its identification and reduction is the main aim of this thesis.

The particle – material related damage is based on so called primary beam parameters in terms of primary ion energy, the ion beam current, and the ion beam cross sectional profile. These parameters usually can't be changed, either because of technical limitations of the microscope or because of necessary processing conditions. Hence, the related interaction with the sample as described in chapter 2.1.9 are intrinsic limitations and therefore unavoidable.

The patterning parameters, on the contrary, are easily adjustable. The patterning strategy by means of PoP, DT and RT can be chosen by the operator in a straightforward manner. The ion beam can also be defocussed, in order to avoid too much damage due to a reduced ion density, but in this case the possibility of producing very fine structures is lost. The stage temperature can be controlled using a

VTS as described in section 2.1.10. Finally the patterning sequence can also be changed which – as will be shown during this thesis – can strongly avoid material damage by reduced local temperatures.

The goal is to explore possibilities to even work with very challenging samples concerning their thermodynamic and chemical properties like melting point, thermal conductivity, and particle / temperature induced chemical altering. Furthermore, as a critical issue we wanted to decouple the process parameters from sample geometry and patterning shape in order to find general ways for improved FIB processing of sensitive materials via ideal processing strategies.

2.1.13 Previous Work at the FELMI: An Alternative Patterning Approach

Previous work at the FELMI (done by Roland Schmied and Harald Plank) focused on first investigations of beam damage during soft matter processing and possibilities of reducing it. Experiments were carried out on PP and HDPE. These experiments showed instable conditions and high chemical and morphological damage for high dwell times and low point pitches. Simulations confirmed that these problems occur due to heat accumulation that could be avoided using an alternative patterning strategy. It was proposed that the heating effect was localized in the vicinity of the beam.

2.1.13.1 Heat Accumulation

If classical patterning is used, neighbouring points are addressed right after each other. As the heat is not strictly confined to the point where the beam is located due to heat dissipation, the neighbouring points are heated as well. If the beam then moves to the neighbouring point, the temperature has already increased and so will increase further, when hit by the beam, than it would for a single point (see Figure 15a). If the beam then proceeds along a line of closely spaced consecutive points – as typically used in classical patterning strategies – the heat accumulates more and more, resulting in final temperatures far beyond intrinsic heating (Figure 15b). This is called technically induced heating and represents one of the most limiting factors during FIB processing of soft matter.

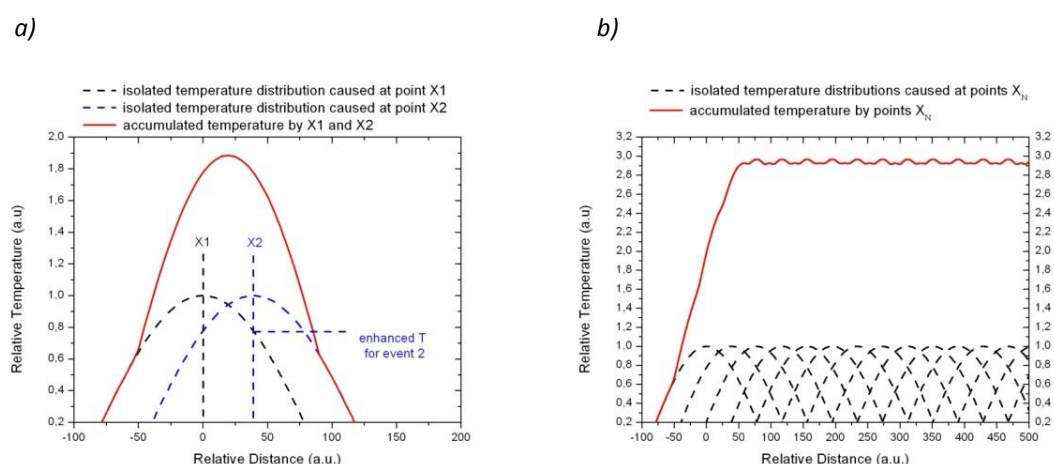


Figure 15: a) temperature increase if two neighbouring points are patterned consecutively. b) temperature increase if many neighbouring points are patterned consecutively (red: final temperature distribution, black / blue: isolated temperature distributions of single pulses).

As the DT directly corresponds to the number of particles which hit the sample, it also directly corresponds to the induced kinetic energy which is then transferred into heat. That is why long dwell times cause high temperatures in the patterned point and through dissipation also in its proximity. Hence very short dwell times can reduce but never eliminate this technically induced heating component.

As can be seen in Figure 15a, the PoP also determines the additionally accumulated heat, as smaller PoPs correspond to more patterning points in the same area and more intrinsic heat is added from neighbouring patterning points. If the PoP is very small, the beam diameter itself becomes relevant, too. The influence will be drastic if the beam diameter is larger than the point pitch, as then the overlapping areas experience a dwell time that is twice as high as specified. Ideally very large PoPs must be chosen to avoid technically induced heating effects. This, however, has the limiting drawback that the patterned areas are not flat any more.

In the following, strategies to recognize technically induced heating experimentally and first successful counter-strategies are presented, which are the basis of this master thesis.

2.1.13.2 Removal Rate (RR)

To visualize the technically induced heating component, described in the previous chapter, the removal rate (RR) is defined as the resulting structuring depth divided through the total exposure time (TET). Please note that redeposition effects (see chapter 2.1.9) make it complicated to use a removal rate by means of volume per time. In previous work at the FELMI it was found that the RR is only stable for short DTs, followed by a quite abrupt increase. The according DTs are defined as critical dwell time (CDT). This increase reflects experimentally that the temperatures are reaching the volatilizing threshold (VT, see chapter 2.4 and 3.4) in the proximity of the ion beam leading to thermally assisted material evaporation caused by technically induced heating [15]. As can be seen in on the left, the critical dwell time is in the range of 100 μs – 250 μs for polypropylene (PP) and high-density polyethylene (HDPE).

The PoP dependence of the RR (Figure 2 on the right) shows the expected opposite behaviour: for small PoPs the RR is very high (red lines) due to technically induced heating (see Figure 15) representing working conditions that can hardly be controlled. For higher PoPs the RR becomes fairly constant, as can be seen in Figure 2 on the right. For shorter DTs the RR increase is strongly reduced but can never be completely eliminated via classical patterning strategies. As a further practical measure during this thesis, the critical point pitch (CPoP) is introduced as the PoP below which the RR becomes unstable. From Figure 16 it becomes experimentally evident what has been described in the previous chapter: very short DTs and large PoPs could basically reduce the effect of technically induced heating. However, as will be shown during this thesis, both straightforward approaches are not working for a material- and pattern-independent FIB processing of sensitive materials.

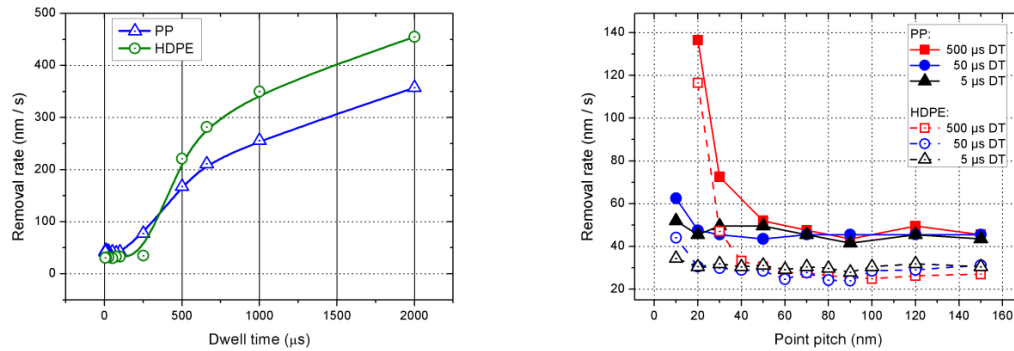


Figure 16: removal rate dependent on the dwell time for a PoP of 20 nm (left) and the point pitch (right) for PP and HDPE [1].

Please note, most pre-experiments as well as all experiments in this thesis have been carried out with primary ion energies of 30 kV and beam currents of 500 pA. This current was chosen since the effect becomes observable very clearly without rapid degradation as observed for higher currents or strongly expanded transition ranges for lower currents. The structures patterned for the RR experiments were $2 \times 2 \mu\text{m}$ squares with TETs of 20 s. Although this has an influence on the absolute value of the removal rate, it does not influence the qualitative behaviour, as the removal rate rises linearly with the number of passes (see section 55) as long as the aspect ratio does not become extremely high. Then the redeposition might start to limit the RR.

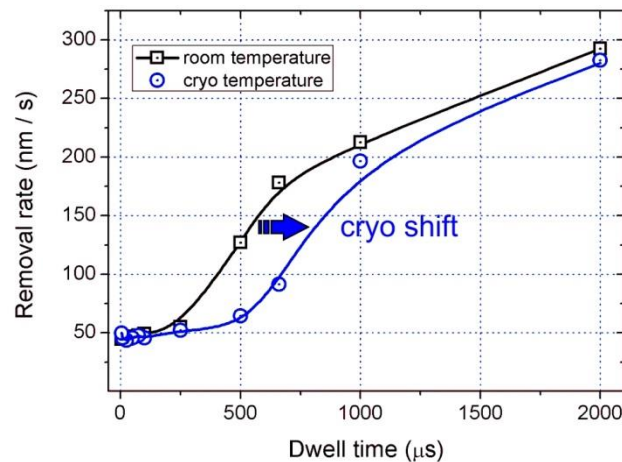


Figure 17: DT dependence of the removal rate at room temperature (black) and at -150°C (blue).

2.1.13.3 Cryogenic Sample Temperatures

As the effects described above are temperature induced it becomes obvious that cooling the sample to cryogenic temperatures could stabilize the procedure and improve the structuring capabilities of sensitive materials. This was done using the VTS described in section 3.1.4 at temperatures of -150°C . However, cooling the sample could only delay but not eliminate technically induced heating as can be seen in Figure 17: the behaviour during a DT sweep (see previous chapter) remains very similar but is just shifted to higher DTs due to the lower sample temperature. These surprising

results, however, can be well explained by the very low thermal conductivity of the polymer which is often the case for low melting materials (see chapter 3.4). In more detail, the material is unable to remove the introduced heat fast enough before a subsequent ion beam pulse. Furthermore, the chemical stability is also improved only a little as will be shown in section 3.1.7.5. Beside the fact that such cryo stages are more complicated to handle and time consuming, these experiments reveal that working at cryogenic temperatures is not sufficient to eliminate technical induced heating during classical patterning strategies.

2.1.13.4 The Interlacing (IL) Strategy

A main achievement of previous investigations at the FELMI is that an alternative patterning strategy has been introduced to overcome the problem of technical induced heating: the interlacing (IL) strategy [15]. The idea behind interlacing is to change the patterning sequence in a way that heat accumulation of closely spaced single patterning points is prevented and to enable heat dissipation before the beam moves to the neighbouring point. For a square the IL strategy consists of a two-step process: the beam does not move directly from one point to its neighbouring point, but instead leaves a well-defined distance (the interlacing distance - ILD) between two subsequently patterned points, as shown in Figure 18 by the blue squares (d_{IL}). When one frame is finished, the whole pattern is shifted by the desired final PoP (d_F) and the same pattern is repeated. This will be done until all the points have been patterned.

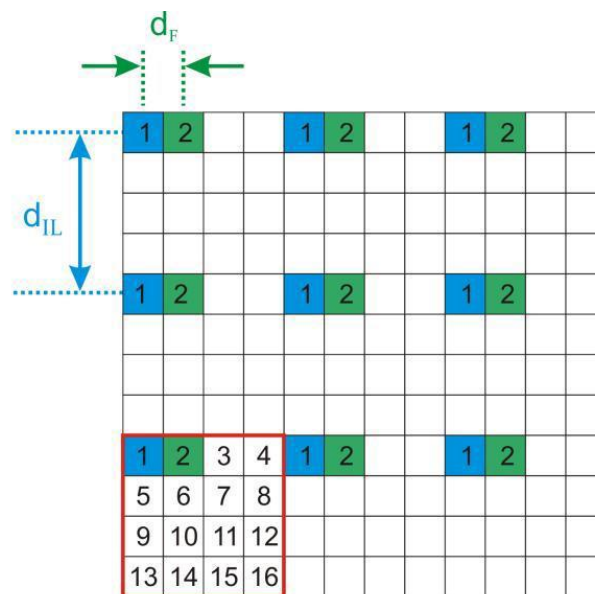


Figure 18: basic principle of the interlacing strategy (for explanation see text).

For a final PoP of 20 nm and an interlacing PoP of 80 nm the pattern would be set up as shown in Figure 18: the first point is the one in the top left corner. Then three points (all spaced by 20 nm) are left out and the beam moves to the fifth point, which is 80 nm apart from the first one. Then three points are left out again. When the first line is finished the beam skips three lines (with a 20 nm spacing) and moves to line five, which is 80 nm apart from the first line. The first frame is finished when all the points coloured in blue in Figure 18 have been patterned. Then the whole interlacing

pattern starts again top left but shifted by 20 nm in X (green block) and the whole procedure is repeated. In the displayed case 16 frames are patterned until the final pattern is the same as a regular single pass pattern with a PoP identical to the shift distance d_f of the interlaced pattern. The only difference in the regular and the interlaced pattern is the sequence in which the patterned points are addressed while the TET is kept constant!

The interesting part however, that only the variation of the patterning strategy has a tremendous influence on the morphology, can be seen in Figure 19: while regular (REG) patterning (left) reveals a strongly rugged surface, the IL strategy (right) stabilizes the morphology and provides clearly improved results. A detailed discussion of the observed effects can be found in recent literature by Schmied et.al. [15].

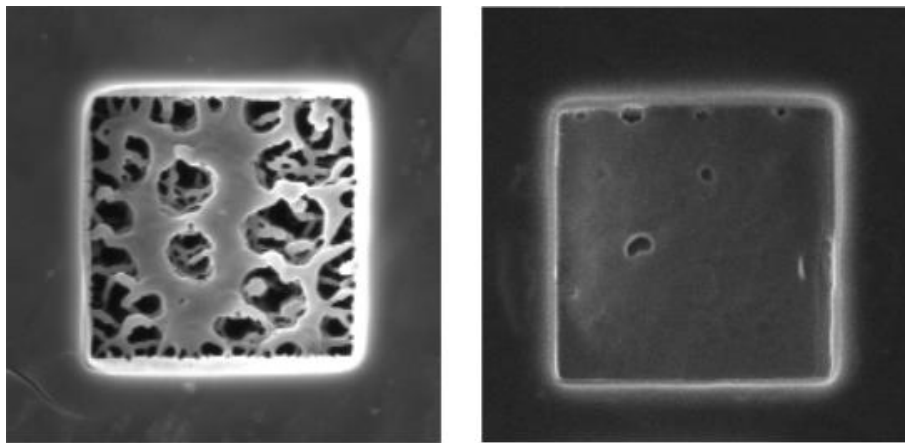


Figure 19: single pass squares with side lengths of 5 μm , patterned with 700 μs DT and 20 nm PoP as a REG pattern (left) and an IL pattern (right) with a d_{il} of 100 nm on PMMA ; patterned with an ion beam current of 500 pA and identical total exposure time.

2.1.13.5 Chemical Degradation

As shown in the previous section, the morphology during FIB processing of sensitive polymers could be stabilized by the introduction of the IL strategy. Additional Raman spectroscopy has been applied to reveal the difference in chemical damage that appears, when different patterning strategies are used. Figure 20 shows representative Raman analyses for PP, where the integrated peak signal between 2700 -3000 cm^{-1} has been acquired corresponding to the most relevant stretching vibrational bands of CH_2 and CH_3 (see also section 2.4). Lower integral values indicate higher damage and reveal that the IL strategies (green bars) are much more independent on individual DTs (single pulse dose) than structures patterned via REG strategies (red bars). Furthermore it can be seen that the values for 50 pA (blue bars) are slightly higher which might promote the use of very low beam currents. But it needs to be considered that if the beam current is reduced by a factor of ten (as has been done in the discussed experiment) the total exposure time which is necessary to reach the same dose rises by a factor of ten. Therefore this might not be an option due to throughput reasons and related drift issues. If the results of patterning performed at room temperature (left block) are compared to the results from the cryogenic patterning conditions (right block) an improvement through cooling can be seen, even though it is only small. This experimentally confirms the

statements in section 2.1.13.3, that cryogenic temperatures cannot compensate for technically induced heating effects and the entailed chemical degradation. For both temperatures it is obvious that shorter DTs lead to increased chemical stability where IL patterns are found to be much less affected while REG patterns with high DT lead to a total loss of the chemical structure. The practical aspect of these findings, however, is the fact that the very easily applicable interlacing strategy is far more effective in preventing chemical damage than cryogenic temperatures, which practically eliminates the necessity of such low temperature stages unless incorporated water is not an issue (e.g. biomaterials).

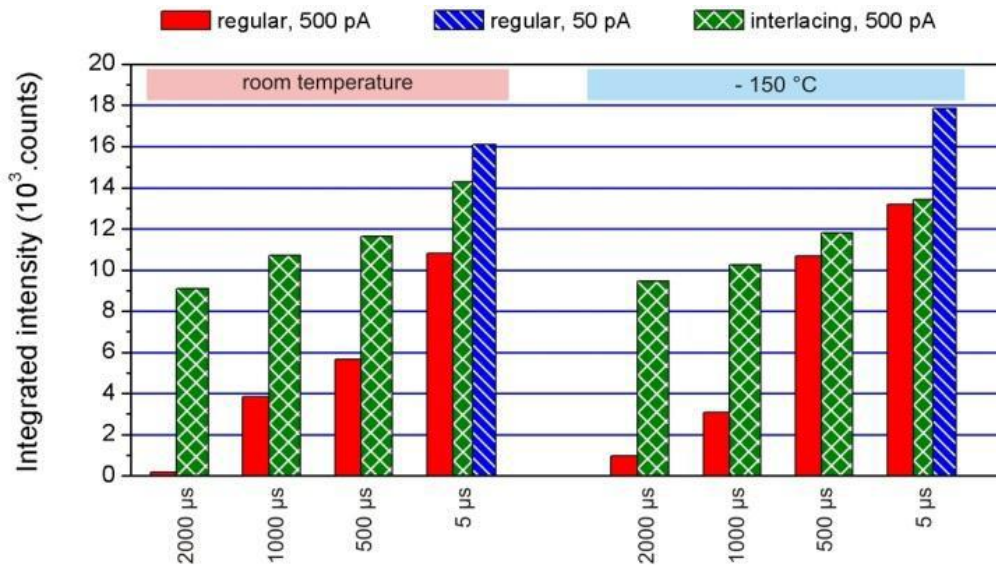


Figure 20: integrated intensity of the Raman signal of structured PP from 2700 - 3000 cm^{-1} corresponding to the CH_2 and CH_3 stretching vibrational bands [15].

2.2 Atomic Force Microscopy (AFM)

2.2.1 Technical Setup

The basic idea of the atomic force microscope (**AFM**) is to get a quantitative 3D image of a sample surface by scanning it with a very fine tip, which is fixed on a fine bar, called the cantilever. The interaction of the tip with the surface bends the cantilever. This deflection is detected by a laser based system and its optical displacement during cantilever bending. The controller electronics analyses the signals and initiates an adequate response of the piezo motions system, which also is responsible for the scanning of the probe over the surface.

2.2.2 Motion System

The requirement to realize reliable movements in the picometer range is provided by piezoelectric elements. These are often (and also in the system used for measurement during this thesis) arranged as a tube scanner. The basic concept is shown in Figure 21a. The movement in X and Y direction is enabled by the lower part of the tube, which consists of four quarter segments (Figure 21b). Two opposite electrodes are oppositely biased, so that one side of the tube is contracted, while the other expands. That way the bottom of the tube and therefore the cantilever perform a lateral movement (Figure 21c). The upper part of the tube is responsible for the movement in Z-direction.

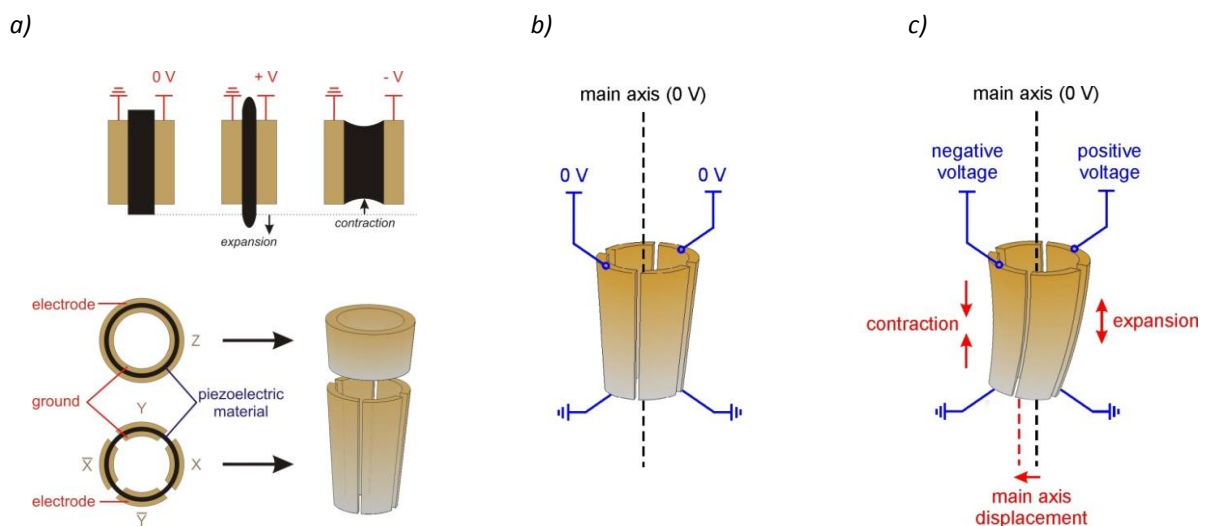


Figure 21: scheme of the piezo arrangement (a) and functionality of a tube scanner (b and c) [1].

The disadvantages of this arrangement lie in mutual mechanical influences, electrical coupling effects and the fact that the movement in X and X direction does not happen on a flat plane, but on a spherical surface. This is corrected by the software. The advantage of this concept is that the lateral sample size is not a problem and even heavy or complex sample arrangements can be investigated.

2.2.3 Detection Systems

The interaction of the AFM tip with the surface leads to cantilever displacements in the nanometer range. This can be detected with an optical system, which positions a laser spot in the foremost part of the cantilever which is reflected back to a position sensitive detector (**PSD**). A distortion of the cantilever, due to the interaction of the tip with the surface, will change the position of the reflection of the laser spot on the PSD. This is schematically shown in Figure 14.

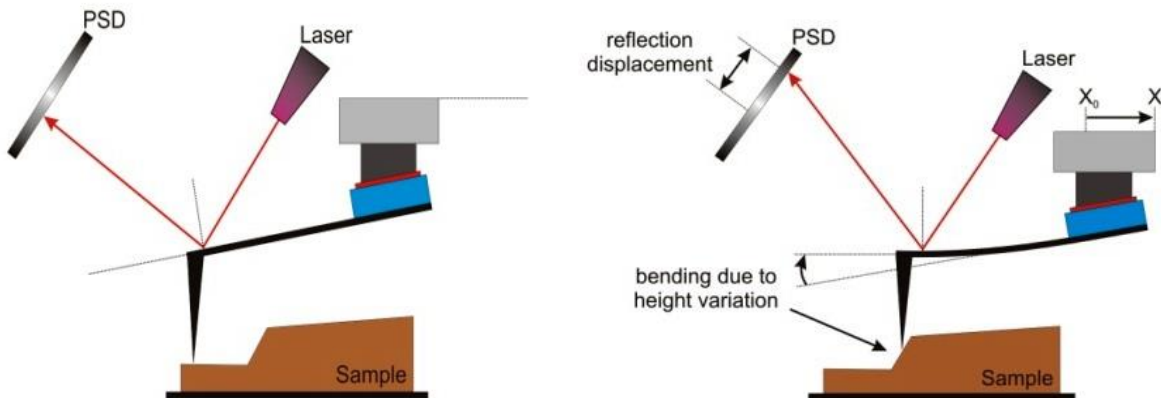


Figure 22: schematic of the detection of the cantilever movement with the optical detection system via correct (left) and bended (right) cantilever geometries due to tip sample interactions [1].

2.2.4 Cantilever and Tip

The distortion of the cantilever allows conclusions on the forces between tip and sample. As this distortion can be well described by Hook's Law ($F = c_0 \cdot x$) the spring constant c_0 is a meaningful quantity to describe the flexibility of a freely oscillating tip, and therefore different cantilevers. Typically there is a differentiation between harder, rectangular tips, with high spring constants, and softer tips, which have a triangular geometry to avoid torsion around the main axis of the cantilever.

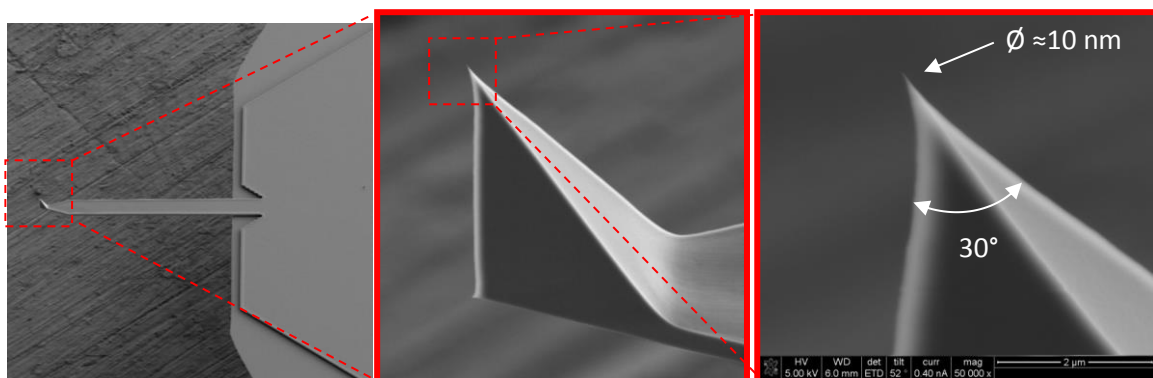


Figure 23: SEM images of a rectangular tapping mode tip also used for AFM measurements for this thesis [1].

A perfect tip with a maximum lateral resolution would be delta shaped. That of course is not possible in reality. The opening angle is about 30° and the final tip radius at about 5 to 10 nm, for commercially available tips, which also have a pyramidal or tetragonal structure. Those non-ideal geometries lead to influences of the measurement, which can mathematically be described by a convolution of the tip geometry with the surface of the sample. Figure 24 schematically shows how the tip geometry influences the lateral resolution, broadens structures and changes flanks in the measurement. From that it can be seen that flattest samples works best for AFM and it becomes also evident why e.g. vertical slopes cannot be imaged correctly [16].

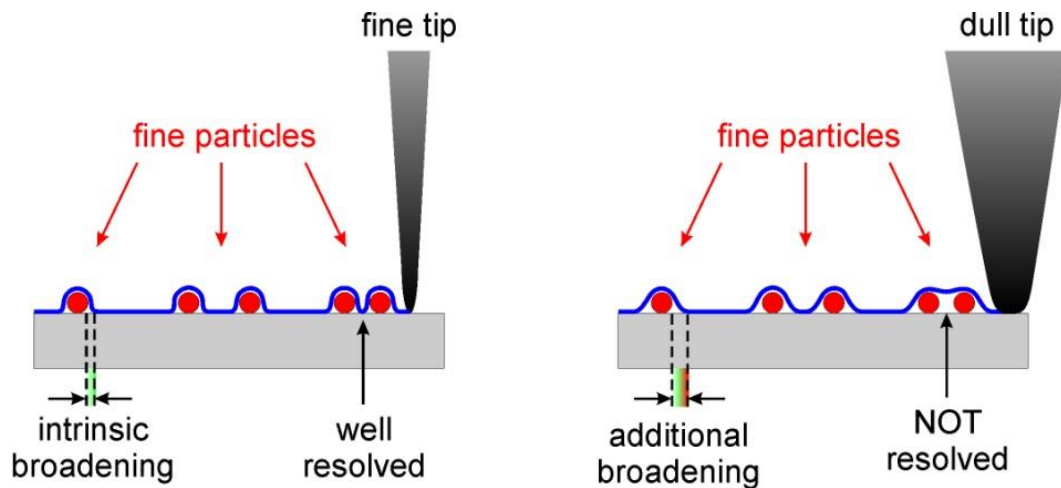


Figure 24: influence of the tip geometry on the resolution [1, 16].

2.2.5 Functionality / Basic Principle

At different distances between tip and surface, the tip experiences different forces. They are listed in the following table.

Table 1: Forces acting between the tip and the surface depending on the distance:

Distance tip-surface	Type of interaction	Potential
> 10 nm	Electrostatic (magnetic)	$\frac{c}{r^2}$
10 nm – 0.5 nm	Van der Waals (dipole – dipole) interaction	$-\frac{a}{r^2}$
< 0.2 nm	$e^- - e^-$ interaction (Pauli principle)	$\frac{b}{r^{12}}$

For morphology tracking, usual working distances are below 10 nm and electrostatic / magnetic forces can be neglected in first approximation. Therefore, the Lennard-Jones potential V_{LJ} can be used to describe the interaction of tip and surface:

$$V_{LJ} = V_{rep} + V_{vdW} = \frac{b}{r^{12}} - \frac{a}{r^6} \quad (1)$$

Where a and b are constants, and r indicates the tip sample distance. When the tip approaches the surface it will first experience an attractive force, as for larger distances the van der Waals term is dominating [16]. If the distance to the surface is further minimized it will increasingly experience a repulsive force, as a further approach of the electron orbitals of the tip and the surface is forbidden by the Pauli principle. Figure 25 shows the interplay of different potential and the different working regimes. For scanning sensitive materials it is advantageous to work in the attractive regime to avoid damage of the sample. However, due to surface contamination and the mostly present water layer, real attractive conditions can be complicated to establish. In such cases the repulsive regime with lowest forces is used, called light repulsive mode. Whenever possible such conditions have been used during AFM investigations for this master thesis.

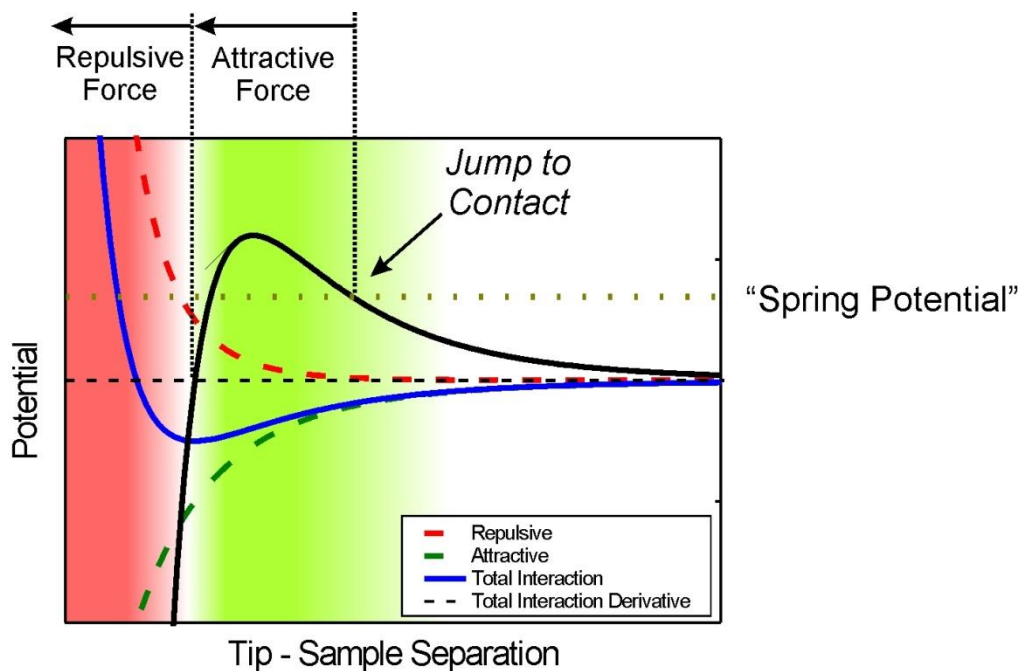


Figure 25: total potential (blue) according to equation 1 as superposition by attractive (green) and repulsive (red) forces in dependence of the tip sample separation. The black curve gives the force onto the tip and the dotted horizontal line indicates the force equivalent originating from the cantilever spring constant. If the resulting force onto the tip is exceeding this limit the cantilever is pulled down to the surface (jump to contact) [1, 16].

2.2.6 Tapping Mode

There are many different modes the AFM can be operated in. A very gentle one, as the contact of sample and tip is reduced is the tapping mode. In this imaging process another piezo crystal excites the cantilever itself in order to oscillate at its resonance frequency. The oscillating laser signal on the PSD leads to an AC voltage, from which an average amplitude (the RMS amplitude) can be calculated. As the oscillating tip approaches the surface the acting forces will dampen the amplitude (see Figure 26a), by a shift for the intrinsic tip-sample related resonance frequency (ω_{coupled}) while the driving piezo still excites the cantilever at its free resonance frequency ω_0 . This leads to an amplitude decay as shown in Figure 26b. In order to keep the RMS amplitude constant the Z-height is adjusted. The Z-values for equal forces are monitored for every coordinate and can therefore be used to form a height image. Please note the exact interaction shows also energy dissipation and by that an additional amplitude damping which contributes to the final amplitude. However, such details are beyond the scope of this thesis but can be extensively studied in reference [16].

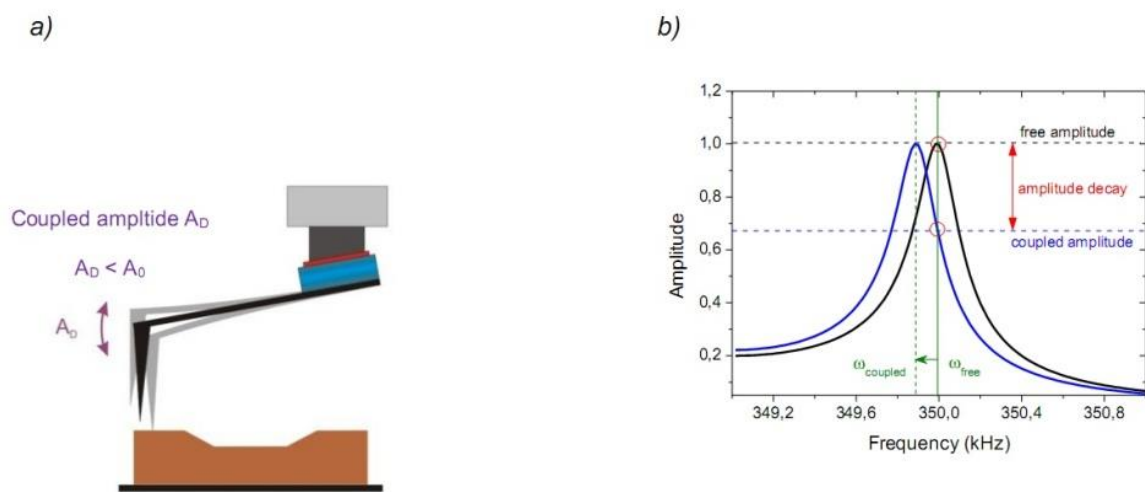


Figure 26: schematic figure of amplitude dampening due to a shift in the resonance frequency [16].

Furthermore, when the cantilever is oscillating at its resonance frequency there is a phase lag between the oscillation of the piezo, and the oscillation of the cantilever. As the approach of the cantilever to the surface leads to a shift in resonance frequency, there is also a shift in this phase lag, which can be used to **1)** determine the working regime (attractive or repulsive); **2)** to detect lateral material variations; **3)** visualize lateral property variations; and **4)** improve the detection of topographical variations on a very small scale by lateral tip-sample coupling effects. Although the phase signal is an extremely powerful expansion to tapping mode AFM, it was not extensively used during this thesis. A detailed description about possibilities and exact working principles can be found in reference [16].

2.3 Raman Spectroscopy

In Raman spectroscopy the inelastic scattering of light is used to investigate a material. The sample is illuminated with monochromatic light, usually in the visible or infrared range. While most of the light is elastically scattered, some of the light is inelastically scattered and transfers energy to the system by exciting molecular vibrations, rotations or phonons.

When a molecule is excited from its present state to a virtual state it may relax into a different state and therefore give off a photon with a different energy than the incoming photon, corresponding to the energy difference between the initial and the final state. Depending on whether the final state of the molecule is higher or lower in energy than the initial state, the energy shift of the photon is called Stokes or Anti-Stokes shift respectively.

A signal at a specific energy shift therefore means that a vibrational or rotational state of a molecule corresponding to exactly that energy has been excited. In combination with the relative intensity this energy shift can often be exactly assigned to a chemical bond. If the material that is analysed is known, an integral over the peak can allow conclusions on the state of the material. The diminishing of a peak therefore means that less of the corresponding vibrations or rotations are excited. It can be concluded, that less of the corresponding bonds exist in the material, and therefore hint at chemical degradation.

All Raman measurements in this work were conducted by Mag. Dr. Boril Chernev and DI Roland Schmied on a Horiba Jobin Yvon LabRam 800 HR spectrometer with a He-Ne laser emitting at 633 nm, a grating with 300 l/mm and a confocal Olympus BX41 microscope. The objective used was x100 (NA = 0.9). The 1024x256 CCD was Peltier-cooled. The standard integration function of the LabSpec® software was used to calculate the integrated intensities.

2.4 Differential Scanning Calorimetry (DSC) and Thermogravimetric Analyses (TGA)

Simultaneous thermal analysis (**STA**) is a method where thermogravimetric analysis (**TGA**) and differential scanning calorimetry (**DSC**) are performed simultaneously. As the measurements are performed in the same instrument on the same sample, the test conditions are identical. During the TGA the mass change of a sample is recorded as a function of temperature and time, which can be related to phase transitions, like vaporization or sublimation, or to chemical reactions. In DSC the amount of heat necessary to change the temperature of a sample and a reference is measured as a function of temperature. During phase transitions involving latent heat either more or less heat is necessary to change the temperature of the sample, compared to the reference, depending on whether the process is exothermic or endothermic. Therefore phase transitions can be detected and analysed.

DSC and TGA work was performed by Dr. Gregor Trimmel and Josefine Hobisch at the Institute for Chemical Technologies of Materials (TU Graz).

3 Materials

3.1 Damage

3.1.1 Thermally Assisted Degradation (Pyrolysis)

Thermal degradation – or **pyrolysis** - occurs when the bonds of a polymer acquire sufficient thermal energy to break or rearrange in significant rates [17]. We can differentiate between two basic types of reactions: **1**) molecular rearrangement; and **2**) reactions involving homolytic scission of bonds to produce free radicals. In both cases the primary products may be very reactive, especially at high temperatures. Therefore secondary reactions are very common.

As addition polymers (like polypropylene or polyethylene) typically have C-C bonds along their main chain axis (called backbone) and commonly also have a great number of hydrogen atoms, the dominant mechanism of degradation usually involves C-C bond breaking and the formation of free radicals, which can result from rapid decomposition at very high temperatures in the range of 300 °C to 500 °C [17]. At such temperatures the free radicals are highly reactive and can undergo a wide variety of reactions including chain transfer and recombination. This may lead to a complex mixture of final products.

If there is a parallel occurrence of different reactions, the activation energy (E_A) will determine which reaction is predominant. Processes with higher activation energies will increase more rapidly with rising temperatures, and decay more rapidly with decreasing temperatures. Therefore, reactions that are negligible at lower temperatures might become dominant at high temperatures. If the activation energy for depolymerization is larger than the activation energy for polymerization, the rate of depolymerization increases faster with rising temperature, than does the rate of polymerization at a given concentration. This may lead to very rapid depolymerization if a critical temperature, called the ceiling temperature (T_c) is exceeded. This phenomenon can for example be observed when working with poly(methyl methacrylate) (**PMMA**, see also section 3.4.1).

Depolymerization (Figure 27) occurs when the bonds along the polymer backbone are broken. This scission can take place through three different mechanisms: 1) **random degradation**, meaning a random breaking along the polymer backbone; 2) **weak-link degradation**, defined by the preferred breaking of weaker bonds; and 3) **depropagation**, meaning that monomer units are successively released from the main chain [17].

Whether scission is followed by depropagation mainly depends on the stability of the chain-end radicals and whether there are hydrogen atoms which are easily removable, which would lead to stabilization. PMMA is an example of a polymer that depropagates chemically clean, because its chain-end radicals are very stable, and the intermolecular transfer of the radical is unlikely due to the absence of easily removable hydrogen atoms. Another reason chain depropagation might be inhibited is the presence of co-monomer units. They may act as blocking agents and therefore hinder the unzip process.

Typical monomer yields during thermally assisted decomposition are strongly material dependent and may vary from nearly 100 % in PMMA [17] to 2 % for polypropylene (**PP**) [17] or even less than 1 % for polyethylene (**PE**) [17]. Please note that chemical effects during pyrolysis can be manifold for different polymers. For this thesis, however, only PP, PE, and PMMA are of high interest, which

undergo mainly the effects described above. A more detailed introduction into this subject can be found in reference [17].

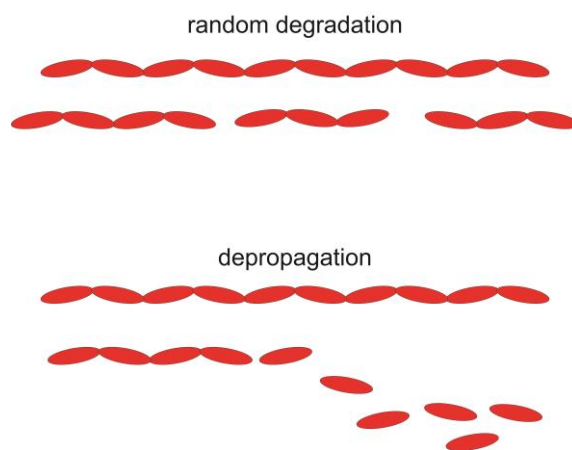


Figure 27: schematic of depolymerisation via random degradation (top) and depropagation (bottom) processes upon temperature exposure.

3.1.2 Degradation due to High Energy Radiation

High energy radiation is absorbed non-specifically. It might be absorbed by the nuclei, but usually the interaction with electron clouds is more important. Often, the energy transfer leads to the formation of ions and secondary electrons which again can cause further processes. Energetic species which are usually trapped in the material include electrons, ions and radical ions. The scission of C-C bonds leads to radicals that can recombine rather rapidly, while the scission of C-H bonds often leads to rather stable radicals and molecular hydrogen [17].

In absence of oxygen there are two main reactions often triggered by carbon centred radicals: **1)** they may take part in **chain-scission** (left hand shift in Figure 28); or **2)** lead to **cross-linking** through a recombination process (right hand shift in Figure 28). Both processes can also occur simultaneously. Therefore, polymers can be divided into these two main groups concerning their reaction to radiation in inert conditions [17]. This tendency can be expressed by G-values. G_x stands for the number of bonds formed for each 100 eV of absorbed energy (cross-linking), while G_s stands for the number of bonds broken per 100 eV of absorbed energy (scission). Cross-linking increases the molecular weight due to the formation of a macroscopic network called a **gel**. The ability of single polymer chains to move past each other is inhibited more and more during cross-linking, and the material will start behaving like a solid. On the other hand chain scission breaks the polymer down into smaller and smaller fragments, which can move past each other more and more easily. The process of chain scission will give the material a behaviour that corresponds more and more to a viscous liquid also called **sol**. The gelling G-value criterion, which was found through statistical treatment of cross-linking and scission processes, states that a gel will not develop, unless $4G_s \ll G_x$ [18]. Typically, polymers that rather cross-link, are considered to have at least one hydrogen atom bound to each carbon atom in their structural backbone, while polymers that tend to scission usually have quaternary carbon atoms with rather large pendant groups [18].

In our experiments a focused ion beam was used for surface structuring. In this case a small part of the sample is irradiated in a laterally inhomogenous manner due to the ion beam profile (see

chapter 4.2.2). As directly irradiated beam areas and effects in the beam proximity cross-link or scission the material, the polymer lengths and by that the distribution of the molecular weight varies. This can be described by polydispersity index which equals 1 for identical molecular weights and increase for a broader distribution. Hence, for both, cross linking and chain scission, the polydispersity index rises upon ion beam exposure. Therefore, the material in the proximity of the beam will not be well defined any longer but reveal a broad distribution of differently modified polymers as schematically shown in Figure 28.

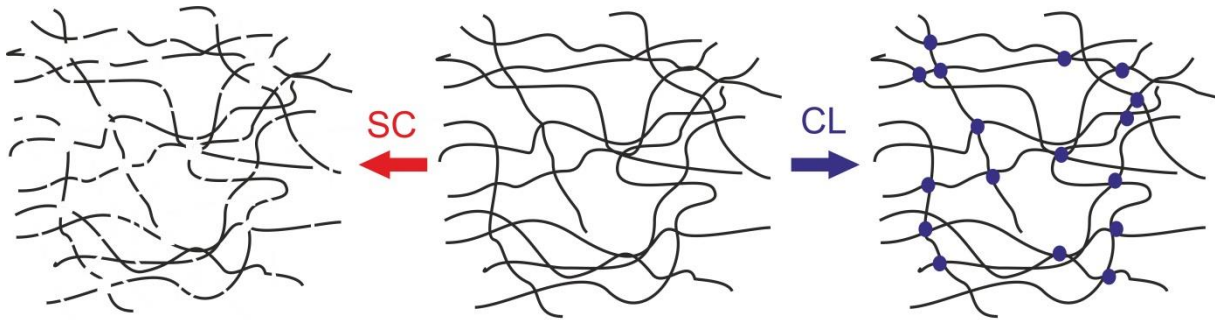


Figure 28: scission effects (towards left) and cross-linking processes (towards right).

Even though the materials can generally be divided in those two groups, whether they scission or cross-link depend on the irradiation conditions as well. Even though PMMA usually scissions, it may also cross-link if it is exposed to very high fluences and very high values of linear energy transfer [18]. Another example is polytetrafluorethylene (PTFE), which also typically scissions when exposed to radiation. But when irradiated in inert atmosphere in a narrow temperature range just above the melting point it can also be cross-linked [19]. However, the ion beam conditions used for this study are basically well below the threshold for this tendency reversal and therefore this effect is only mentioned because of completeness.

3.2 GEL - SOL

We consider a material which consists of many subunits (individual polymer chains in first approximation). These subunits have the ability to bond with each other. If so many links are formed, that a macroscopic network evolves, the material will have mechanical properties reminding of a solid, like a non-zero shear modulus. The material is then called a **gel** and highly disordered [20]. Even though the mechanical characteristics can often be compared to those of a solid, the **gel** may contain a high volume fraction of liquid components.

A gel may show very different properties depending on the fragment types it is made up of. If the gel consists of long chain segments, which are flexible and might be considered random walks joined together by cross-link points, their mechanical properties can be described by the theory of rubber elasticity. Gels containing a large amount of short rigid fragments will rather show glassy behaviour [20].

What also has a big influence on the behaviour of a gel, are the kind of bonds between subunits. We can differentiate between **physical** and **chemical gels** depending on the nature of their bonds. Chemical gels have their networks formed through chemical bonds, like for example covalent bonds between molecules [20]. An epoxy resin is an example of a chemical gel. In physical gels the cross-

links come from an interaction of physical nature, like for example crystalline parts that form, including more than one long polymer chain [20]. These physical gels are often known to be thermoreversible. A prominent example of a physical gel is jelly. Another example is PE [21], which was also used in experiments for this thesis.



Figure 29: the gelation transition defined by an increasing network.

As defined, a necessary condition to call a material a gel, is that the number of links between subunits is high enough so that a macroscopic network is formed, as shown in Figure 29. If that is not the case, the material will have different rather liquid-like properties which is then called a **sol**. The transition of a material from a sol to a gel is called gelation transition or **sol-gel transition**, and happens through a process of increasing the number of links between subunits, until a macroscopic network is formed [20].

Starting from a basic polymer the different effects upon high radiation exposure and / or thermal effects can decide about a gel or sol formation: cross-linking leads to a gel while chain scission results in a sol phase, as shown in Figure 28. This will play an essential role in this thesis when working with PMMA as a scissioning material (sol transition) and with PE as representative of a classical cross-link material (gel formation).

3.3 Soft Matter

As soft matter we define materials which are neither simple liquids nor crystalline solids with typically low melting points such as polymers or biological materials which typically show low thermal conductivities and higher specific heat capacities [20]. The thermal conductivities of polymers are about three orders of magnitude lower than those of classical metals. These characteristics make them hard to process with a focused ion beam microscope, as the particle beam has a lot of energy which to a large extent remains in the material as heat. The higher specific heat capacity on the other hand allows the storage of energy for a longer time period which makes cooling even more complicated. Those two qualities in combination often lead to very problematic results, as the low thermal conductivities and specific heat capacities prevent the heat from dissipating away fast enough from irradiated areas and the resulting high temperatures often easily exceed the low melting points and promotes pyrolysis which leads to material modification described in the previous chapters.

For polymers the thermodynamic quantities cannot strictly be given, as they strongly vary depending on the polymer used and its definition by means of the polydispersity index. This can be influenced by the average chain length and the chain length distribution, as well as how branched the chains are, and whether the polymer has been exposed to any environmental effects.

3.4 Materials Used

3.4.1 Poly(Methyl MethAcrylate) (PMMA)

One of the most challenging, and therefore also one of the most interesting materials we used during our investigations was poly(methyl methacrylate) (**PMMA**), which is commonly known as acrylic glass. It is well known as photoresist material used as standard resist in semiconductor industry. PMMA is generally known as a non-gelling polymer, in fact it undergoes an extremely clean scission process, often leading to monomer yields of almost 100 % [17]. Therefore, if it is exposed to radiation and / or temperature treatment, it usually scissions, leading to a sol phase for increased temperatures. It has a G_S value of 1.8 and a G_X value of 0. [17].

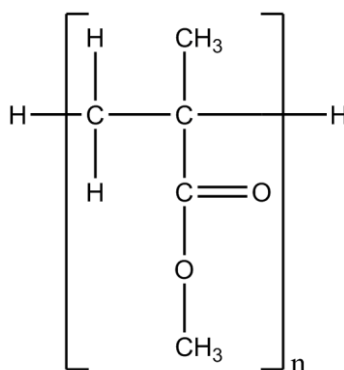


Figure 30: chemical structure of PMMA.

Figure 30 shows the chemical structure of PMMA which is basically amorphous and has strictly seen no clear melting point but just a glass transition temperature.

Its thermal conductivity at 20 °C is given around $0.21 \text{ W}\cdot\text{m}^{-1}\cdot\text{K}^{-1}$ [17, 22], while its specific heat capacity at 20 °C is around $1400 \text{ J}\cdot\text{kg}^{-1}\cdot\text{K}^{-1}$ [17].

The PMMA sample we used for our experiments had a weight average molecular mass of M_w of $67480 \text{ g}\cdot\text{mol}^{-1}$ and a number average molecular mass of M_n of $37470 \text{ g}\cdot\text{mol}^{-1}$ resulting in a very good polydispersity index of 1.8. From the mass average molecular mass we can conclude that the average chain length is around 675 monomer units which equals a total length of about 200 nm in fully extended conformation.

The volatilizing threshold of the PMMA we used was experimentally determined via simultaneous thermal analysis (**STA**, see section 4.1.4) and defined by a 2 % criterion in the thermogravimetric analyses (**TGA**, see section 4.1.4) to $V_T = 310 \text{ °C}$ (see Figure 31 by the black curve). Furthermore, a small peak in the differential scanning calorimetry (**DSC**, see section 4.1.4) can be seen around 120 °C which indicates the glass transition temperature of PMMA which can be seen as phase change point.

For our investigations a small PMMA block was embedded in epoxy, cut and mechanically polished. It was also coated with a very thin layer of carbon ($\sim 10 \text{ nm}$) and the conductive carbon tape at one edge, with which it was fixed to the sample holder plate, was used to contact the surface to allow charge to flow and therefore minimize charging effects when working with the dual beam

microscope. An image of the PMMA sample is shown in Figure 32. All the other samples were prepared in the same way, except for PEG and PP. We also used a PMMA sample, which was spin cast and used in its provided shape, respectively. The samples for the low temperature experiments at $-150\text{ }^{\circ}\text{C}$ were also not embedded, because they had to be very thin for the cooling to work, and also that they could be mounted on the variable temperature stage (see section 2.1.10).

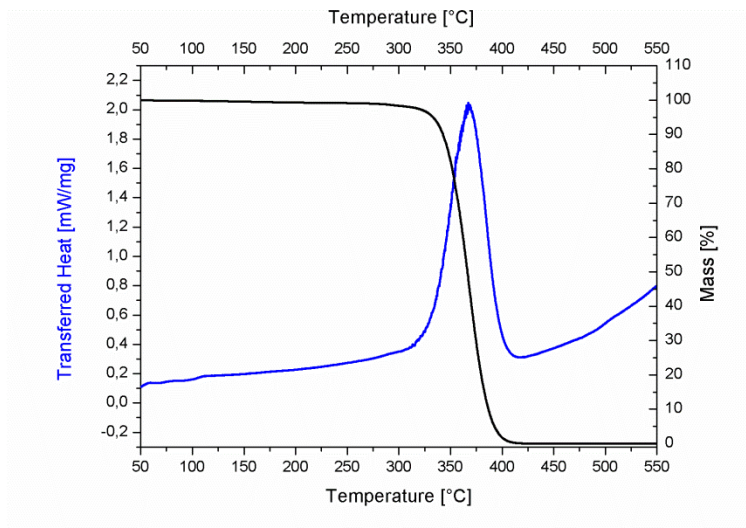


Figure 31: DSC (blue curve, left Y axis) and simultaneous TGA (black curve, right Y axis) for PMMA.

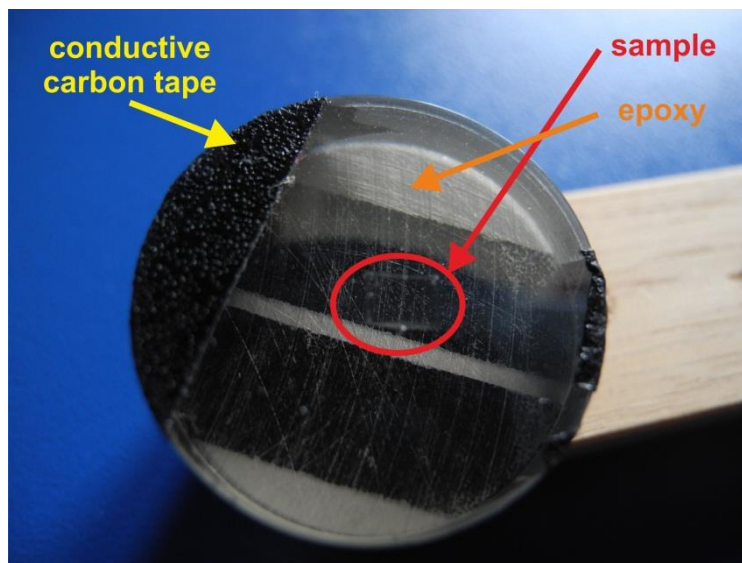


Figure 32: PMMA sample embedded in epoxy.

3.4.2 High Density PolyEthylene (HDPE)

Polyethylenes (**PE**) are well known commodity plastics and make up more than 70 % of the total plastics market [21]. There is a wide variety of applications including many household products. PE is thermoreversible and can therefore be reprocessed several times [21]. The difference between high

density polyethylene (**HDPE**) and low density polyethylene (LDPE) is that HDPE has got less side chains and is therefore more densely packed, revealing semi-crystalline characteristics.

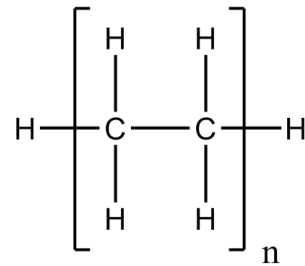


Figure 33: chemical structure of HDPE.

The chemical structure of HDPE is shown in Figure 33 and this polymer rather tends to cross-link than to undergo chain scission. Its G_x value is approximately 2.1 while its G_s value is given as 1.3 [20].

Its thermal conductivity at 20 °C is given around $0.52 \text{ W}\cdot\text{m}^{-1}\cdot\text{K}^{-1}$ [17, 22] while its specific heat capacity at 20 °C is found around $2075 \text{ J}\cdot\text{kg}^{-1}\cdot\text{K}^{-1}$ [17].

The HDPE we used for our sample was ordered as a rod from “Alfa Aesar” [23]. Also determined by STA experiments (Figure 33), we found the melting point of the HDPE we used at 130 °C and the volatilizing threshold at 400 °C.

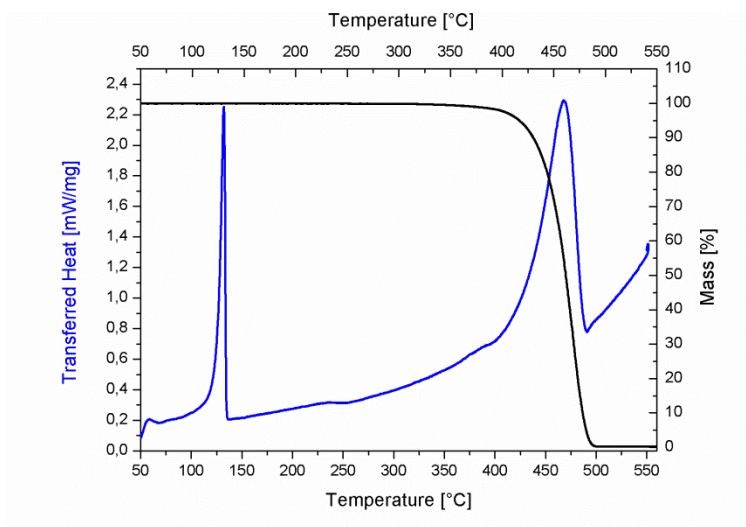


Figure 34: DSC (blue curve, left Y axis) and simultaneous TGA (black curve, right Y axis) for PEG.

3.4.3 PolyPropylene (PP)

Polypropylene (**PP**) is a semi crystalline material and after PE one of the most important industrial plastics. If exposed to radiation it mainly cross-links with a G_x value of 0.9. It also scissions, as it has a G_s value of 0.6 [17]. Figure 35 gives its chemical structure.

Its thermal conductivity is low even for polymers with $0.12 \text{ W}\cdot\text{m}^{-1}\cdot\text{K}^{-1}$ at 20 °C [17, 22]. While its specific heat capacity at 20 °C equals $2350 \text{ J}\cdot\text{kg}^{-1}\cdot\text{K}^{-1}$ and therefore is rather high [17].

The melting point of the PP used in our experiments is found at 168 °C, while the volatilizing threshold is at 365 °C determined via STA measurements shown in Figure 36. Our PP samples used for this study were not embedded, but directly polished due to sufficiently large dimensions of the purchased source material.

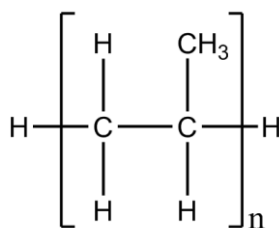


Figure 35: chemical structure of PP.

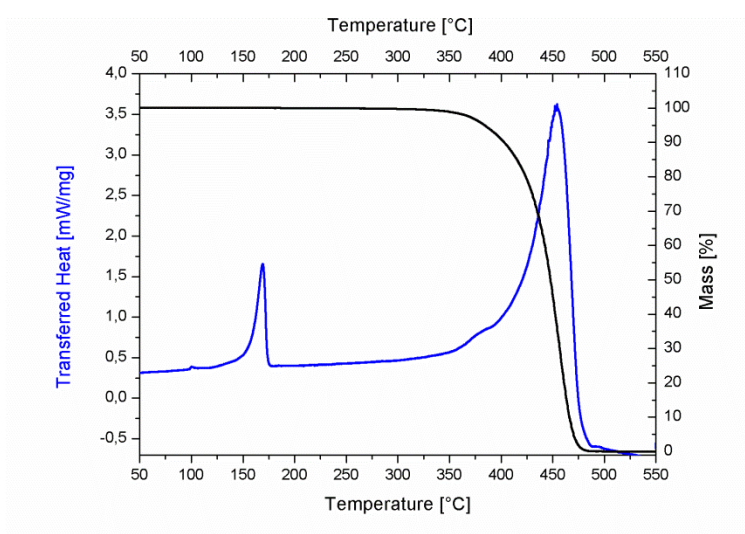


Figure 36: DSC (blue curve, left Y axis) and simultaneous TGA (black curve, right Y axis) of PP.

3.4.4 PolyEthylene Glycol (PEG)

As polyethylene glycol (**PEG**) is water soluble and non-toxic it is often used in biological and especially in medical contexts [24]. It is also known as polyethylene oxide (PEO) or polyoxyethylene (POE). PEG crystallizes to a high extent as spherulites (spherical arrangement of lamellars starting from a central nucleus). X-ray diffraction experiments indicate that when PEG crystallizes packed antiparallel helical structures of opposite handedness are present with the oxygen in the core of the helix surrounded by the hydrophobic methyl groups [24].

PEG is very reactive when exposed to radiation and / or high temperatures. If the two G values are compared it can be concluded, that the slightly predominant reaction is chain scission, as its G_s value equals 2.1 and its G_x value equals 1.8 [17].

While thermal conductivity values are barely reported in literature, the specific heat capacity equals $0.3 \text{ W}\cdot\text{m}^{-1}\cdot\text{K}^{-1}$ at 20 °C [25]. Its chemical structure can be seen in Figure 37.

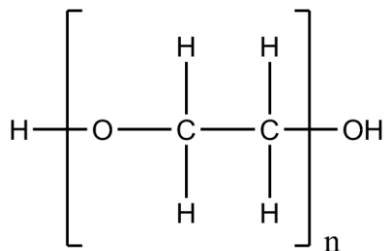


Figure 37: chemical structure of PEG.

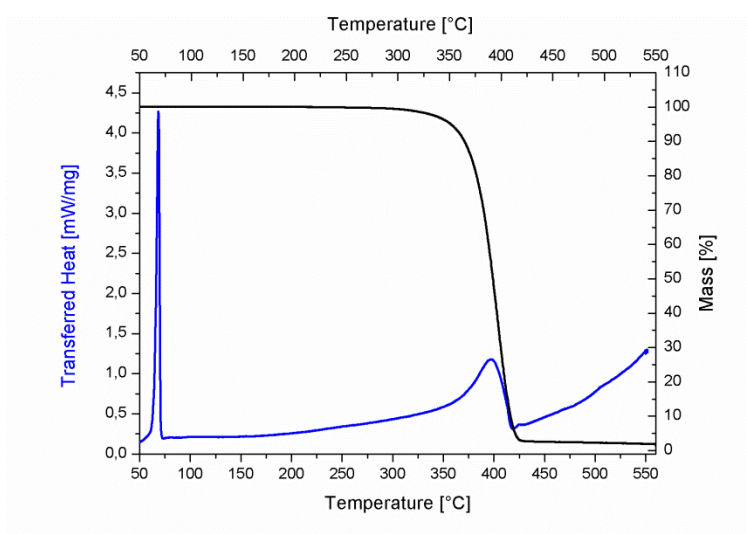


Figure 38: DSC (blue curve, left Y axis) and simultaneous TGA (black curve, right Y axis) for PEG.

In our experiments we used PEG with mass average molecular mass (m_w) of $35.000 \text{ g}\cdot\text{mol}^{-1}$. Its melting and volatilizing threshold are found to $68 \text{ }^\circ\text{C}$ and $330 \text{ }^\circ\text{C}$, respectively. Both were determined through an STA measurement shown in Figure 38.

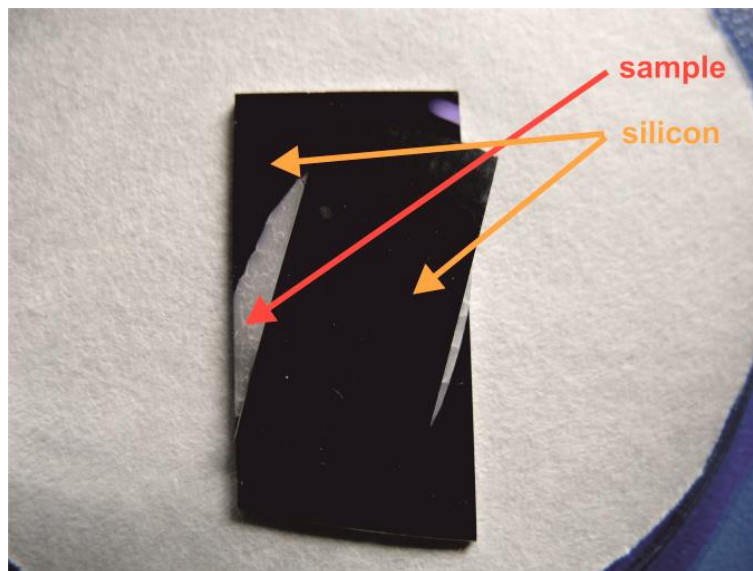


Figure 39: PEG that has been molten and shock-cooled between two pieces of silicon.

To prepare a PEG sample for our measurements, we melted it on a hot plate (110 °C) on a silicon substrate, to ensure, that the sample is as flat as possible. We put another piece of the silicon wafer on top and then shock-cooled the silicon-PEG-silicon “sandwich” in liquid nitrogen to prevent phase transitions as often observed via slow cooling. The sample at this stage is shown in Figure 39. When the top silicon wafer piece was taken off, we obtained a sufficiently flat surface of PEG, although crystallization had taken place. A lot of spherulites could be seen as will be shown in section 4.1.6.

3.4.5 Ethylene Vinyl Acetate (EVA)

Ethylene vinyl acetate (**EVA**) is a copolymer consisting of ethylene and vinyl acetate as shown by its chemical structure in Figure 40. By varying the percentage of vinyl acetate the properties (like for example the melting point) of the polymer can be changed. We used two versions of EVA with VA percentages of 9.3 % and 25 %. Their melting points were at 100 °C and 78 °C, respectively, determined via STA measurements shown in Figure 41. The samples were ordered at “Dupont” [26], the names of the products were “Elvax 360” (9.3 %) and “Elvax 760Q” (25 %).

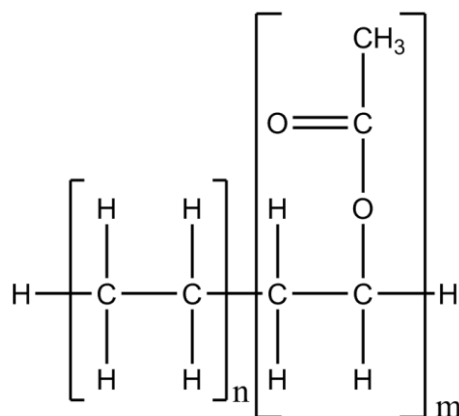


Figure 40: chemical structure of EVA, where the left block corresponds to ethylene and the right represents vinyl acetate.

EVA with a low VA content has properties that are very similar to those of LDPE. With a rising VA concentration the degree of crystallinity sinks and its behaviour becomes more similar to that of thermoplastic rubbers [27].

EVA decomposes in two stages. When EVA is heated the first product of thermal degradation is acetic acid which is produced during a cross-linking mechanism. The reaction is based on ester pyrolysis and starts at about 300 °C and has its maximum reaction rate at about 330 °C. Every VA sequence needs its own initiation step. The loss in mass during this decomposition stage is proportional to the amount of VA initially present in the copolymer. In the second step of decomposition the chains scission [27].

One can easily see the mass loss during the reaction producing acetic acid as the first drop in the mass curve in the STA data. It is clearly visible, that the material with more VA has the greater loss in mass. The reaction is also visible in the heat transfer peak, which is also clearly larger for the polymer with the greater VA content.

The thermal conductivity of $0.23 \text{ W}\cdot\text{mK}^{-1}$ was reported for EVA with a VA content of 28 % [28].

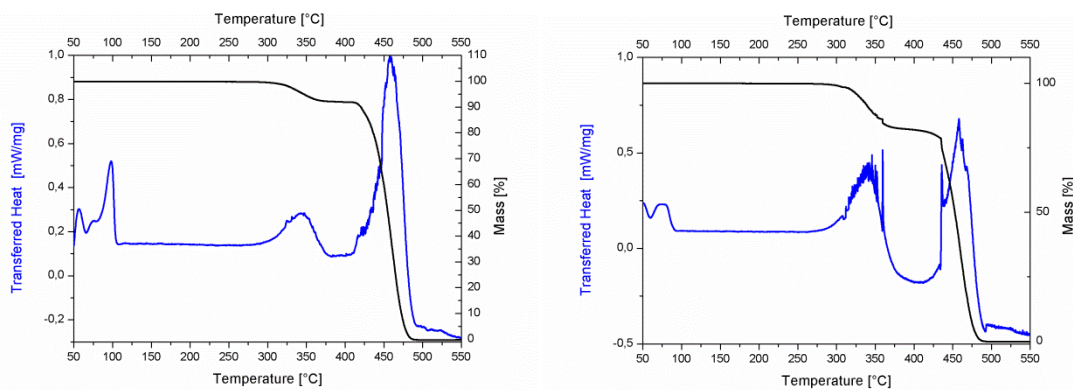


Figure 41: STA data for EVA with 9.3 % of VA (left) and 25 % of VA (right). DSC signals are shown in blue (left Y axis) and TGA data are given in black (right Y axis).

As for all other materials STA (Figure 41) was used to determine the melting point, and the volatilizing threshold. For the EVA sample with 9.3 % of VA the volatilizing threshold for the remaining material after the formation of acetic acid is at 421 °C. For the sample with 25 % of VA it is at 429 °C.

4 Experiments and Results

As described before this master thesis is an integrative part of a bigger project at the FELMI, which aims at separating intrinsic unavoidable processing influences from avoidable processing influences (as shown in Figure 42), and therefore improving results when patterning critical materials. Previous work included the demonstration of the existence of a technically induced heating component and its compensation via an alternative patterning approach. The motivation of this thesis was the clarification of thermally induced degradation effects in the proximity of the ion beam. The primary idea was to clarify whether there exists a relation between FIB patterning parameters and the thermodynamic material properties which are summarized in section 4.1 (Correlation 1). During these investigations it turned out that there exists another, even more important component based on the chemical effects during FIB processing which are discussed in section 4.2 (Correlation 2). Based on both correlation results, a special counter-strategy was derived and successfully implemented which is explained in section 4.3 (Smart Interlacing).

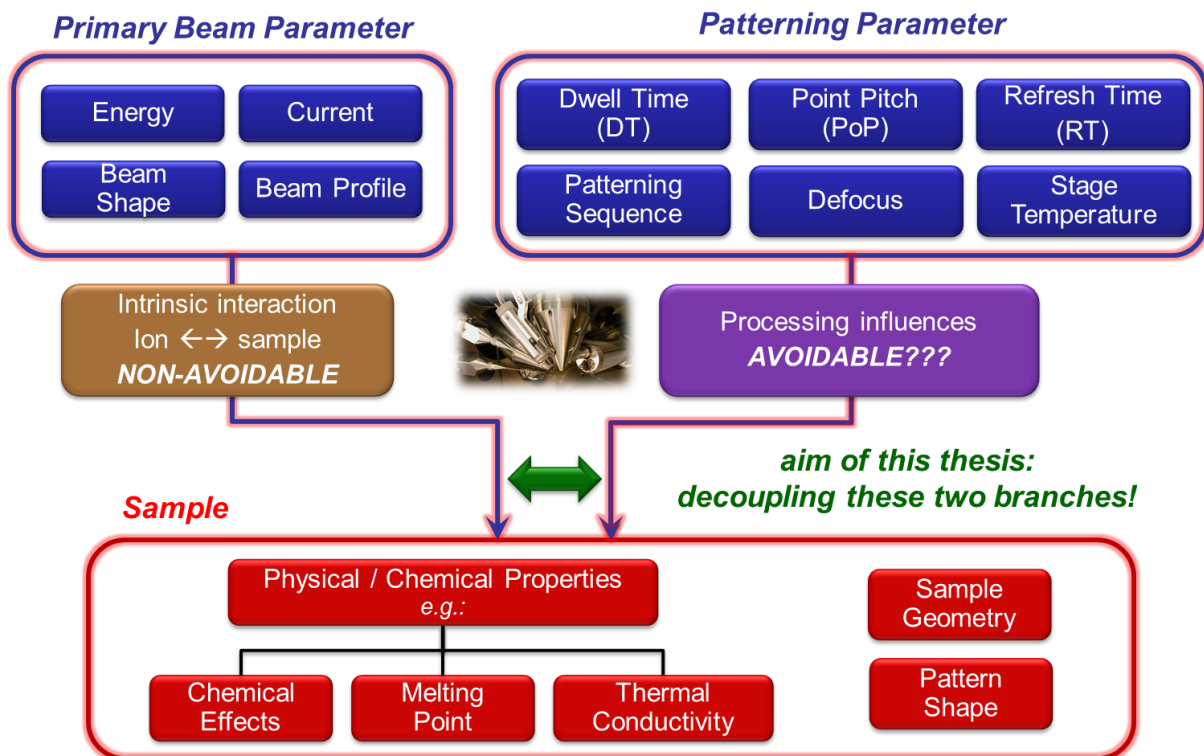


Figure 42: representation of the aim of this thesis, which corresponds to separate intrinsic unavoidable effects from avoidable processing influences, and therefore improving results when patterning critical materials.

4.1 Correlation 1 - Thermodynamic Properties as Key Element

4.1.1 Introduction

As described in sections 2.1.13 the primary aim was to correlate morphological / chemical degradation due to technical induced heating with thermodynamic quantities of different polymers such as melting points, thermal conductivity and specific heat capacity. In particular, the use of different dwell times, point pitches, refresh times as well as interlacing point pitches should reveal the relation between local heating effects and material related properties. Finally, room- and cryo temperatures should be compared to extract the particular role of the thermal conductivity. While previous work was only focused on polypropylene (PP) and high-density polyethylene (HDPE), which both show a comparably high melting point of 168 °C and 365 °C, respectively, this thesis was aimed at expanding the range of used polymers so that very low melting points down to 65 °C can be accessed.

Please note, unless otherwise stated all FIB experiments have been performed using primary ion energies of 30 kV and ion beam currents of 0.5 nA.

4.1.2 Removal Rate (RR) Experiments

4.1.2.1 Dual Beam Microscope (DBM) vs. AFM

During first investigations the cross section characterization tool of the DBM was used to measure the depth of the obtained structures, which would then be used to calculate the RR. While a 52° tilt angle was used as standard configuration for most of the cross sectional measurements, very deep structures required a stage tilt to lower angles in order to access the bottom areas with the electron beam. During the acquisition of these values it soon became obvious that the measured depths varied for different stage tilts α . The reason for this lies in the necessary assumption of fully vertical structure slopes and well defined bottom edges for the reliable use of the DBM cross sectional tool. Both of these conditions are not always fulfilled mainly because of redeposition (see section 2.1.9), but also because of temperature effects, which particularly blurred the bottom edges. As can be seen in Figure 43 by top view SEM images the lower edge (which finally has been used for primary depth measurements) is widened ($\Delta X \neq 0$) for some parameters (left square) which indicates a non-vertical slope. For comparison an ideally patterned structure is shown on the right with negligible widening ($\Delta X \approx 0$).

Together with the blurred bottom edges it is very difficult to estimate where to place the measuring tool which leads to insecurity ΔZ that can be estimated from the geometric conditions using: $\Delta Z = \Delta X \cdot \tan(\alpha)$, where ΔX represents the horizontal distance between upper and lower edge as a convolution of slope and edge blurring. As shown in Figure 44 ΔZ can be significant for low inspection angles

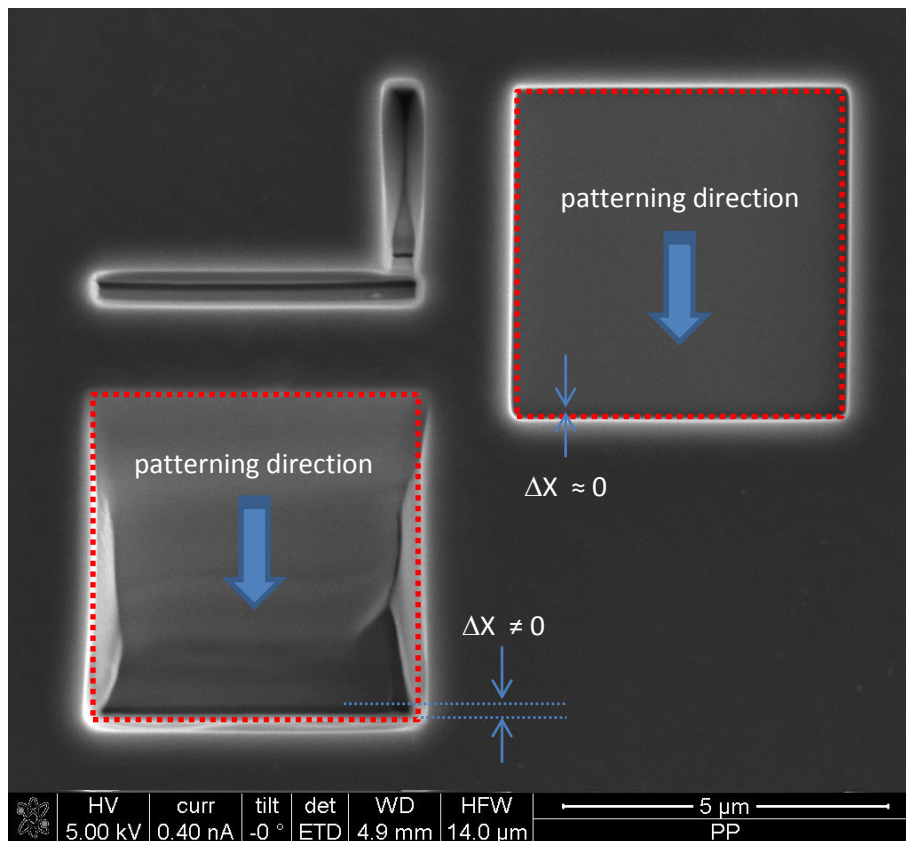


Figure 43: slope broadening and bottom edge blurring (left square) compared to ideal situation (right square) performed on PP. The dotted red lines indicate the intended pattern shape.

As the resulting variations introduced an unreliability, it was decided to perform all further depth measurements via AFM. The main limitations resulting from this decision were that the maximum depth accessible is approximately 6 μm due to the maximum Z-range of the AFM limited by the piezo-system and that high aspect ratios can be problematic due to tip geometry related issues (as explained in section 2.2.4). Furthermore it must be noted that the real side slopes are not accessible via AFM, which however was not of interest during the aimed AFM depth characterization.

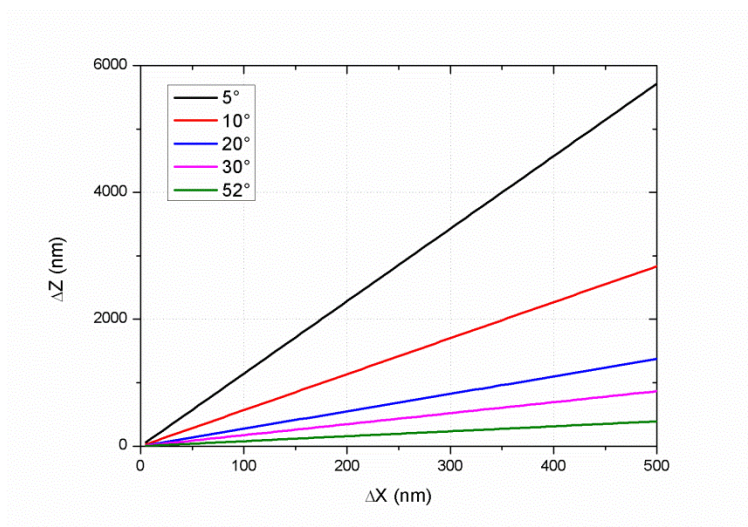


Figure 44: systematic measurement error when using the cross section tools on non-vertical slopes.

4.1.2.2 Patterning Size Influence

First experiments were performed using $2 \times 2 \mu\text{m}$ structures, which led to reliable results working with PP and HDPE. However, for low melting materials such as PEG and PMMA morphological instabilities made measurements on such small pattern sizes complicated (see Figure 45). One reason for this is redeposition effects which are known to be more pronounced for materials with a high sputter rate respectively lower melting points. The effect becomes furthermore dominating for higher depths (higher aspect ratios) where it gets more and more complicated to remove the sputtered material from such high aspect ratio trenches. Hence, the use of larger patterns for more reliable analyses was necessary.

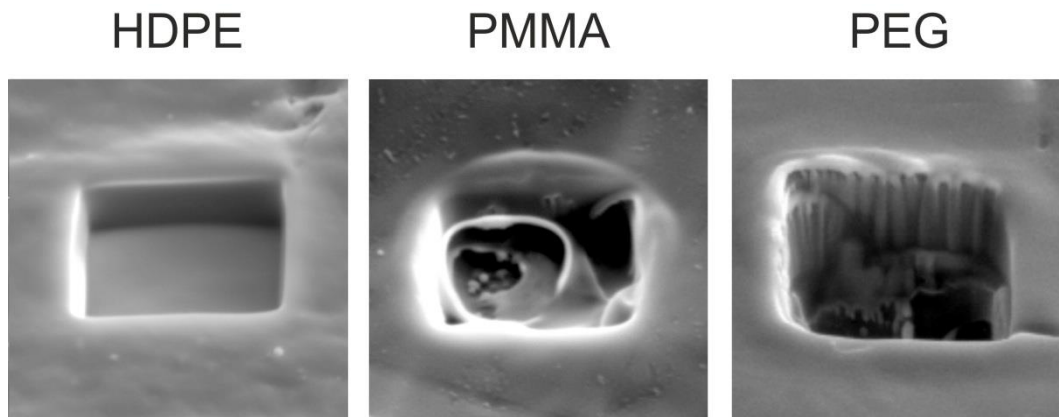


Figure 45: $2 \times 2 \mu\text{m}$ squares in HDPE (left) with clean cut edges and PMMA (middle) and PEG (right) where intended square structure is not represented anymore.

During the change from $2 \times 2 \mu\text{m}$ to $5 \times 5 \mu\text{m}$ the striking effect of redeposition becomes evident as representatively shown for HDPE in larger patterns show clearly deeper structures for identical total exposure times per μm^2 , further denoted as specific total exposure time (STET). From that, it is clearly visible that a simple comparison of patterns with different sizes is not possible and limiting effects need to be considered. As outcome of these pre-investigations, a pattern size of $5 \times 5 \mu\text{m}$ was chosen for all further experiments which turned out to be sufficiently large for all polymers and parameters used.

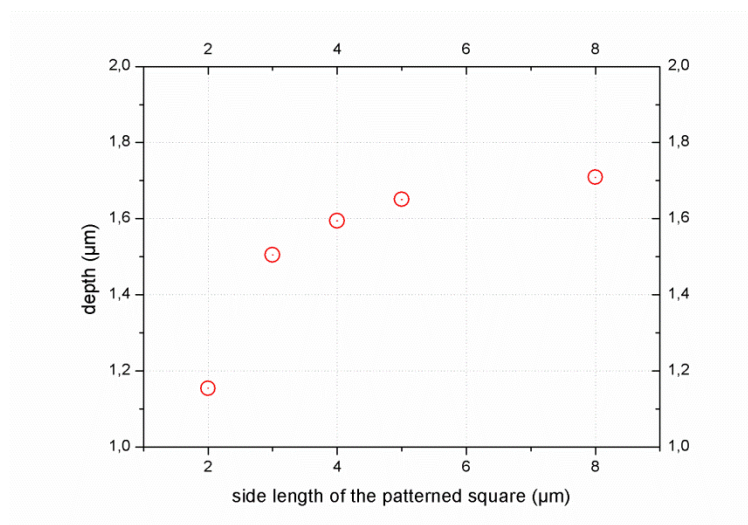


Figure 46: depth dependent on the side length of the fabricated square.

4.1.2.3 Point Pitch (PoP) and Dwell Time (DT) Influence

As expected due to studies performed by Roland Schmied et.al., all polymers investigated showed the same qualitative behaviour as PP. For a constant point pitch (PoP) of 20 nm the specific removal rate (SRR) is widely constant for small dwell times (DT) and then rises rapidly, as can be seen in Figure 47. This increase indicates that temperatures in the ion beam proximity reach and exceed the volatilizing threshold (VT) of the material and thermally assisted proximity evaporation starts to contribute to the RR. The specific removal rate (SRR) is introduced to decouple the RR from the patterning size and is given via the depth divided by the total exposure time (TET) and the pattern size in μm^2 . The critical dwell times (CDT) are in the region of 250 μs for all polymers. Only for PEG the RR rises earlier together with clearly higher absolute SRR values which is caused by the extremely low melting point of about 65 °C.

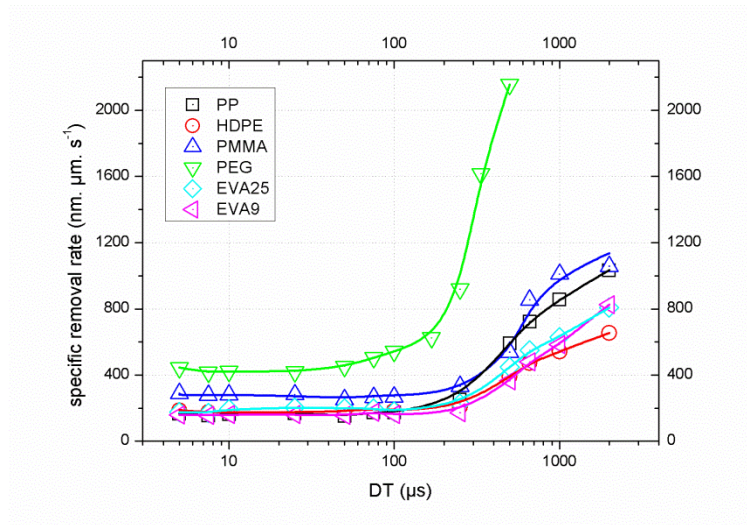


Figure 47: direct comparison of DT sweeps for PEG, PMMA, PP, HDPE, EVA 25 and EVA 9. Experiments have been performed with a PoP of 20 nm.

Because of that all further RR experiments on PEG were carried out with only half the number of passes (half the TET) than all the other removal rate experiments. Otherwise the limitation of the AFM would have made measurements impossible. But even with only half the TET not all structures could be measured. In the DT sweep the structures performed with DTs of 1000 μs and 2000 μs were too deep to be measured with the AFM. Therefore those two points are missing in Figure 47. PMMA also seems to have a slightly higher removal rate than the other polymers in the constant regime.

Concerning PoP variation the situation is again as expected and therefore opposite. If patterning is performed at rather high DTs (e.g. at 500 μs as shown in Figure 48) the following could be observed: for small PoPs the RR is large and unstable whereas it stabilizes for larger PoPs. This is because for small PoPs the volatilizing regime is reached due to heat accumulation for closely spaced single points (see section 2.1.13). For very low DTs of 5 μs the effect vanishes and removal rates stay fairly constant, as can be seen in Figure 49. For intermediate DTs of 50 μs (Figure 50) most polymers show a weak RR increase towards small PoPs, while for the low melting PEG it was still clearly visible. This is also consistent with the principle of technically induced heating discussed in section 2.1.13.1, because heat accumulation of neighbouring points strongly depends on individual heating and by that on the single pulse duration.

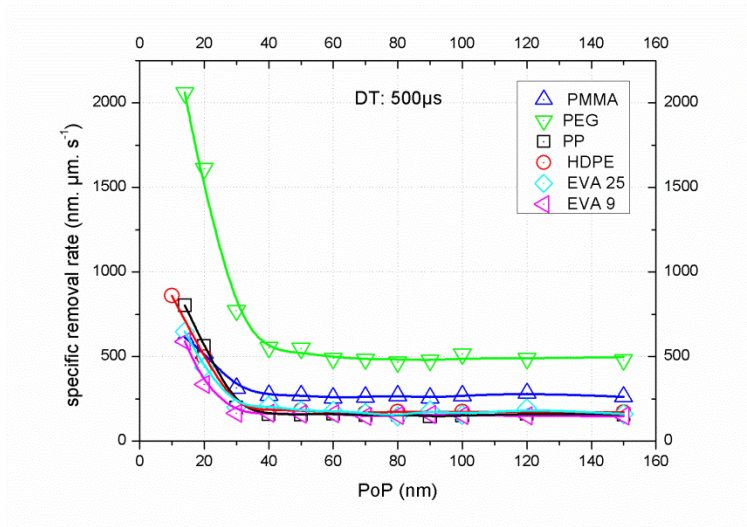


Figure 48: direct comparison of PoP sweeps with 500 μs DT for PEG, PMMA, PP, HDPE, EVA 25 and EVA 9.

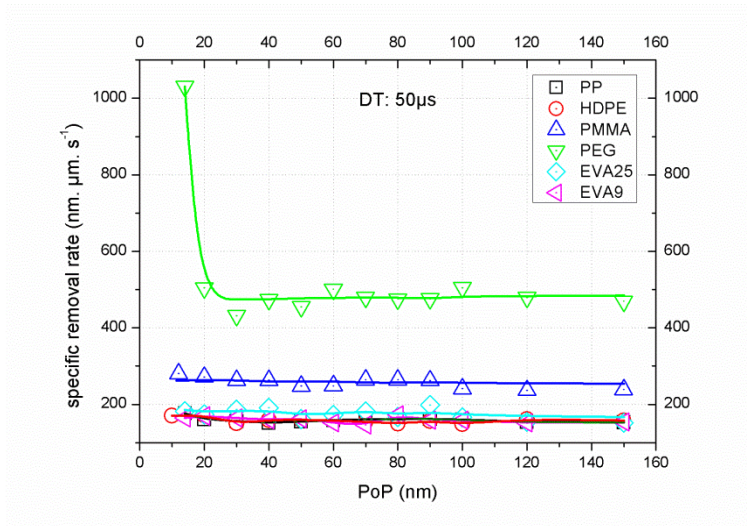


Figure 49: direct comparison of PoP sweeps with 50 μs DT for PEG, PMMA, PP, HDPE, EVA 25 and EVA 9.

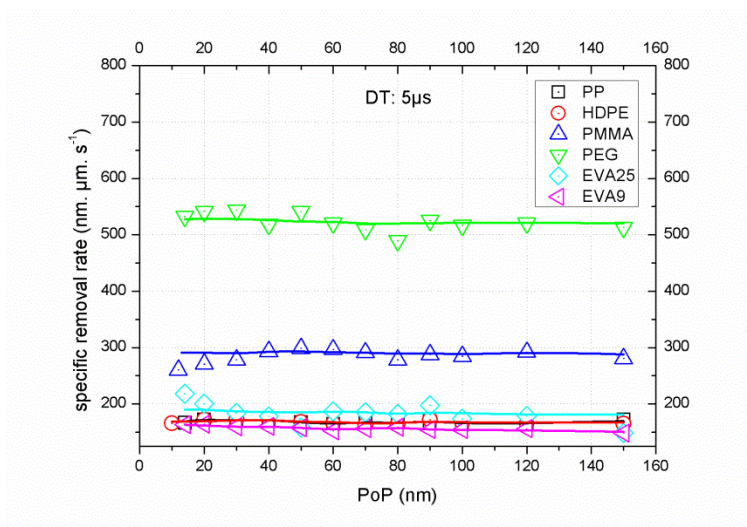


Figure 50: direct comparison of PoP sweeps with 5 μs DT for PEG, PMMA, PP, HDPE, EVA 25 and EVA 9.

The absolute values of the SRR under stable conditions are always highest for PEG followed by PMMA and similar, as well as low, for the other materials used. Before any conclusion toward a correlation between SRR tendencies and material related thermodynamic properties can be drawn, additional experiments have to be discussed. Finally, chapter 4.1.2.6 will discuss the mentioned correlation between processing and material properties.

Please note, when the results are compared to previous work at the FELMI [15], it needs to be considered that in the cited study the RR was calculated from the depth, while here the SRR is used. As they worked with $2 \times 2 \mu\text{m}$ squares, their results need to be multiplied by four to get the specific removal rate.

4.1.2.4 Influence of the Interlacing (IL) Strategy

As discussed in section 2.1.13.4, the interlacing (IL) strategy can strongly reduce technically induced heating by the alternative patterning sequence. To investigate whether the strategy also works for the additional polymers PMMA, EVA, PEG, and HDPE, a DT sweep for REG and IL strategies have been performed. Figure 51 shows the SSR summary for both strategies and all three materials. As can be seen, even for very high DTs of 2 ms no SRR increase is observed. This clearly proves the IL strategy to be capable of eliminating technical induced heating during FIB processing.

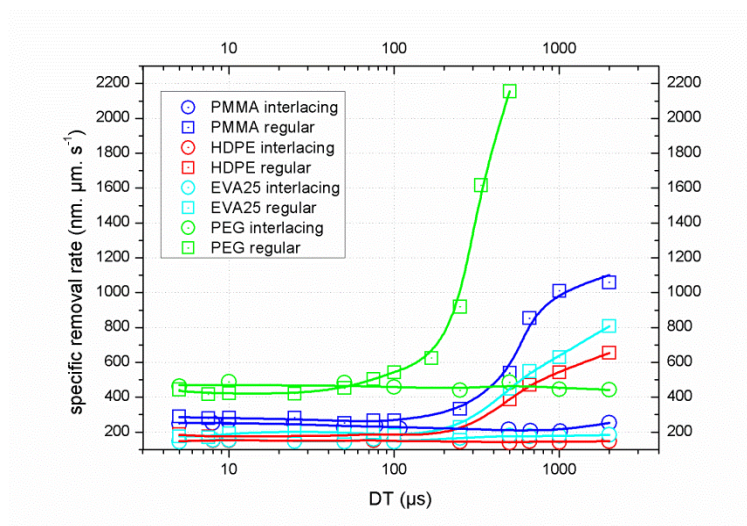


Figure 51: direct comparison of DT sweeps for PEG, PMMA, HDPE and EVA 25. Experiments have been performed with a PoP of 20 nm.

4.1.2.5 Influence of the Interlacing Distance (ILD)

As shown in the previous section, the IL strategy works very well for eliminating technically induced heating effects due to heat accumulation in the proximity of individual patterning points. To find out more about the effect of interlacing, structures with constant DTs and PoPs were made, while the interlacing distance (ILD) was varied. By that, we can estimate the lateral heat distribution after single point exposure by determining the critical ILD. First a variation was performed on a single pass pattern with $500 \mu\text{s}$ DT, 20 nm final PoP and an ILD variation from 200 nm down to 20 nm which is identical to a REG patterning strategy. Figure 52 shows the overall results revealing very constant

SSRs down to about 70 nm for PEG and to about 50 nm for all other polymers. This suggests a lateral heat expansion of at least such values after a 500 μs ion beam pulse at 30 kV and 500 pA. From these experiments one might be tempted to always use highest ILD. However, one has to keep in mind that increasing ILDs mean a lower number of patterning points within a single IL frame. This means also that the refresh times (RT) are shorter and the material cannot cool down entirely. Figure 53 shows the RR dependency on the ILD: starting from the constant minimum an increase can be seen for shorter ILDs which indicate the rise of technical induced heating. For increasing ILDs there is also an increase observable which results from the decreasing RTs as described above. Hence, the pattern size itself plays a role which will be a major issue in this thesis later.

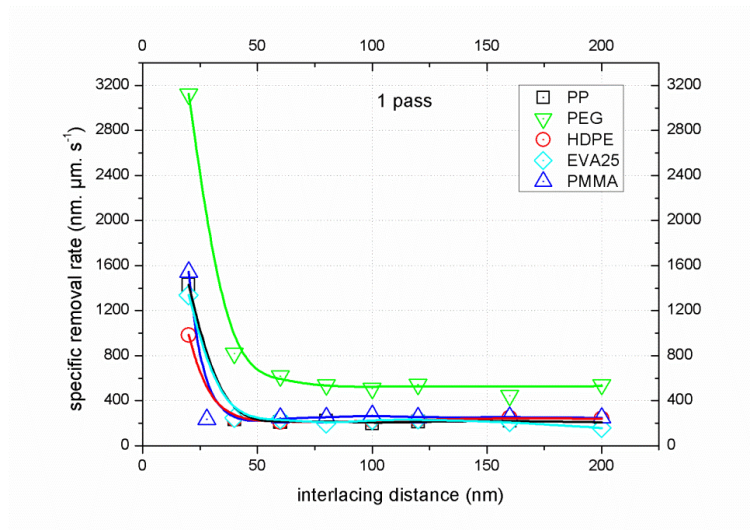


Figure 52: direct comparison of d_{IL} sweeps for PEG, PMMA, PP, HDPE and EVA25. Experiments have been performed with a single pass and a DT of 500 μs and a PoP of 20nm.

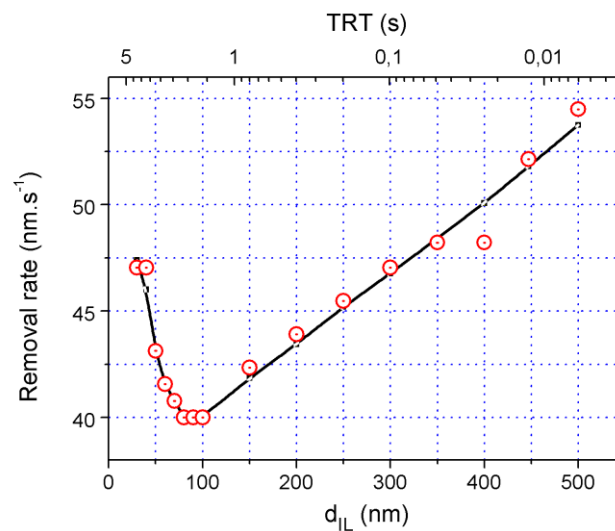


Figure 53: RR variation in dependency on the interlacing distance d_{IL} (bottom X axis). The top X axis gives the according total refresh time (TRT) which decreases for increasing interlacing distances [15].

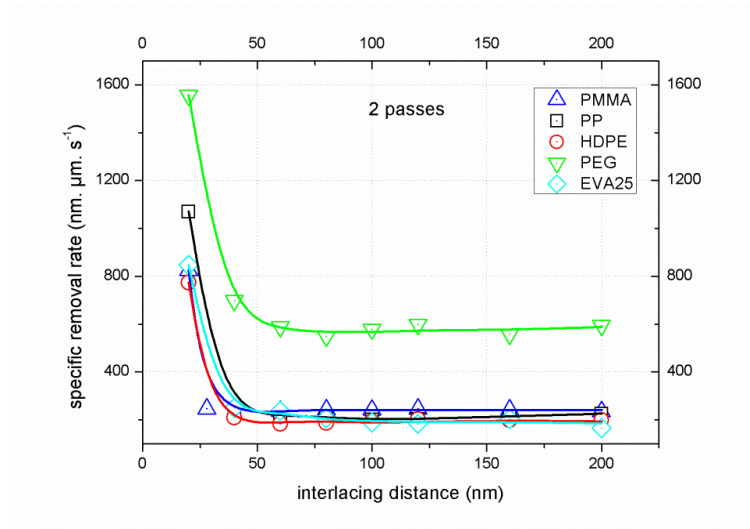


Figure 54: direct comparison of d_{IL} sweeps for PEG, PMMA, PP, HDPE and EVA25. Experiments have been performed with 2 passes and a DT of $500 \mu\text{s}$ and a PoP of 20nm.

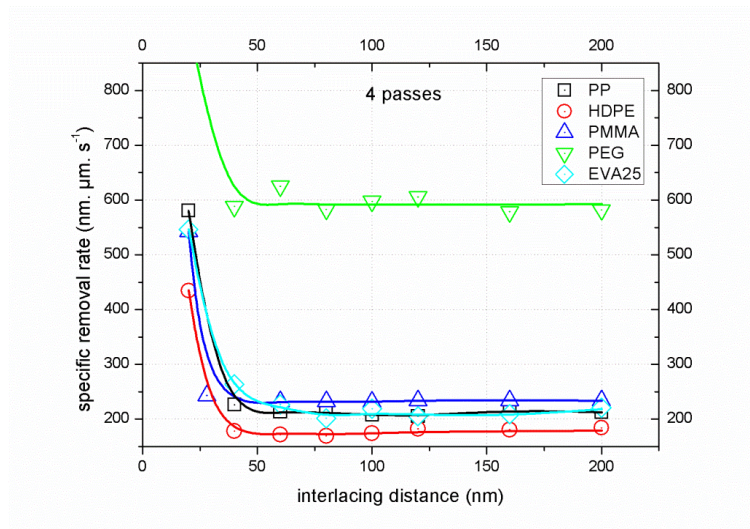


Figure 55: direct comparison of d_{IL} sweeps for PEG, PMMA, PP, HDPE and EVA25. Experiments have been performed with 4 passes and a DT of $500 \mu\text{s}$ and a PoP of 20nm.

The next step was the investigation of the IL behaviour for increasing depths via multi-pass processing. For all investigated numbers of passes (1, 2, 4) the obvious result is that while ILDs above the critical ILD stabilize the SRR, it is unstable for more regular patterning like conditions (short ILDs). For one, two and four passes the stable regime (see Figure 52, Figure 54 and Figure 55) reveals constant SRRs of approximately $600 \text{ nm}\cdot\mu\text{m}^2\cdot\text{s}^{-1}$ for PEG and around $200 \text{ nm}\cdot\mu\text{m}^2\cdot\text{s}^{-1}$ for the other investigated polymers. In contrast, towards REG patterning conditions the SRR is extremely unstable and decreases non-linearly for increasing passes. E.g. for PEG the values for one and two passes are ~ 3100 and $\sim 1500 \text{ nm}\cdot\mu\text{m}^2\cdot\text{s}^{-1}$, meaning a SRR decay of 50%. The same tendencies can be seen for all other polymers as well! Patterning in this regime is very unreliable and unpredictable and can therefore not be used for any applications where defined depth is of importance. The interlacing strategy also gives far better morphologies especially if structures that are made with a small number of passes are considered. Due to redeposition there is often a clearly visible slope if a regular

patterning strategy is used, because of serpentine or raster movement of the beam. This is not given, when interlacing is used because the beam jumps. Figure 56 shows a direct comparison for PP.

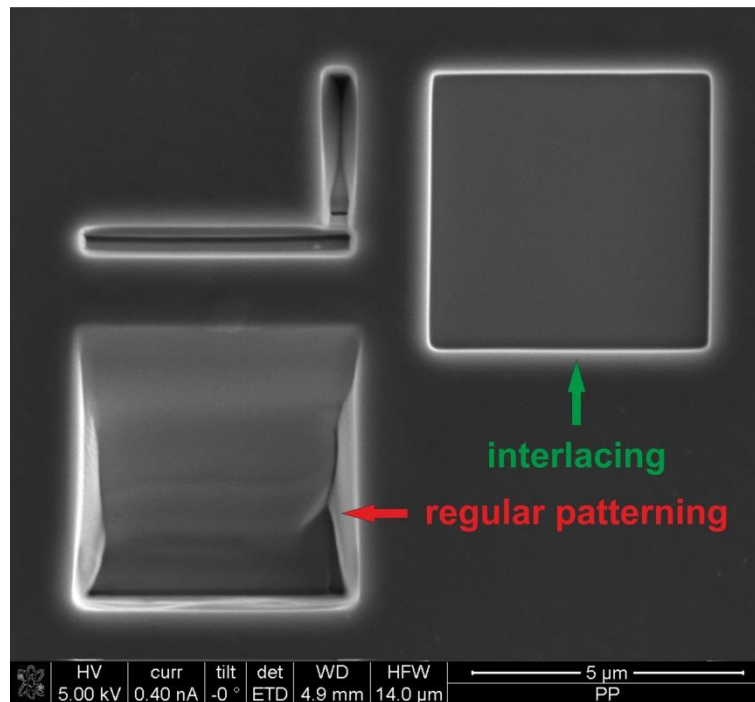


Figure 56: direct comparison of the morphology of a regular and an interlaced pattern on PP (box sizes 5x5 μm , DT = 500 μs , d_{IL} = 40 nm, single pass pattern).

Finally some problems occurred for special patterning conditions which are based on technical hardware limitations. Figure 57 shows an AFM amplitude image and a SEM image of PP samples after FIB processing: for ideal hardware settings there is no difference between REG (left) and IL (centre) patterns recognizable. For improper conditions, however, a superstructure can be observed as shown on the right in Figure 57. This stems actually from the patterning engine used during this thesis, which can only address 4096 x 4096 pixels. If a PoP smaller than the native resolution is addressed, rounding errors occur, which results in partial multi patterning of single points. Hence, the native hardware resolution has to be kept in mind when very small PoP are used together with large areas or many patterns.

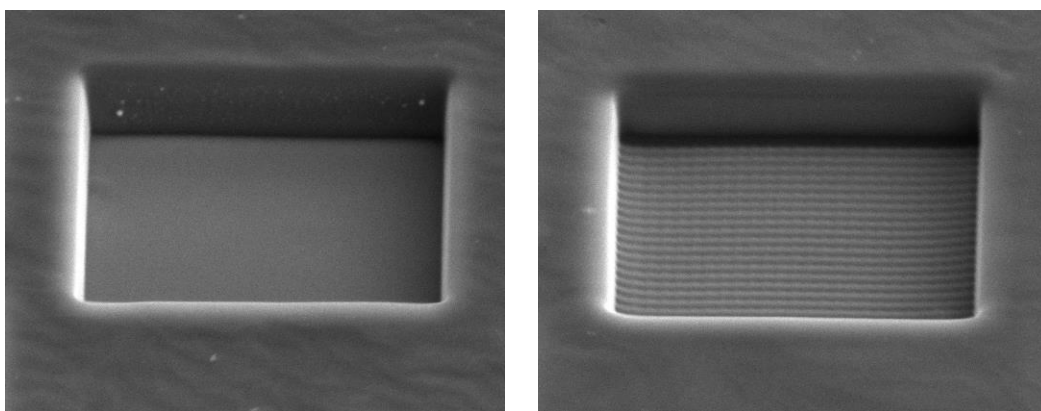


Figure 57: patterning engine influences of ideally (left) and non-ideally set boundary conditions shown by SEM images of interlaced structures in PP (5x5 μm , DT = 500 μs , PoP = 20 nm, ILD = 200 nm, 4 full frame passes).

Fortunately a new patterning engine has recently been installed at the FELMI which expands the addressable point to 65536 x 65536 pixels. This reduces the risk of unwanted superstructure effects and allows large area patterning with high resolution.

4.1.2.6 Straightforward Parameter Adaption as Alternative to Interlacing

From the section 4.1.2.3 one might deduce that it is enough to simply choose very small DTs or high PoPs to prevent technical heating for reliable FIB soft matter processing. However, that argument does not hold! A particular problem lies in the morphology of the resulting structures which is discussed in this chapter.

The first straightforward parameter adaption would be an increasing PoP to prevent proximity heating as discussed in section 2.1.13.1. However, due to the large PoP distance a superstructure appears at the bottom of the structure, as shown by AFM height images in Figure 58. The reason for this appearance is the fact that sufficiently large PoPs (to prevent proximity heating) are achieved when the individual beam profiles of neighbouring patterning points are barely overlapping. This, however, entails a non-uniform lateral sputtering which results in superstructures. Hence, the reduction of unwanted overheating is accompanied by the loss of structuring capabilities and thereby not applicable at all.

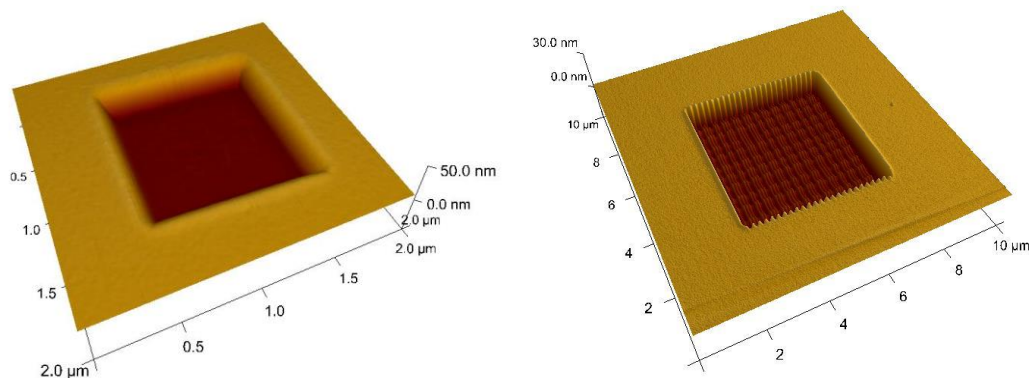


Figure 58: morphological effect due to large PoPs: while small PoPs results in flat bottom areas (left) sufficiently increased PoP values lead to superstructures at the bottom of the structures (right).

The second and actually more promising possibility to reduce unwanted proximity heating is to keep the individual pulses short. Short DTs work indeed very well for the fabrication of shallow structures as can be seen in Figure 59 at the left. However, when deeper structures are of interest, which are realized by multi-passes, a morphological instability appears as shown top right in Figure 59. The origin of this effect is assumed to be slow heating of the entire pattern due to the multi-passes. At a certain point the entire pad is hot enough that the additional patterning lead to temperatures beyond the VT which entails laterally inhomogeneous material evaporation. The bottom line message, however, is that even very short DTs are not sufficient to compensate for technical heating as IL patterning can do (see bottom right in Figure 59). Please note, the special morphology observed for multi-pass REG patterning will play a major role in the second part of this thesis!

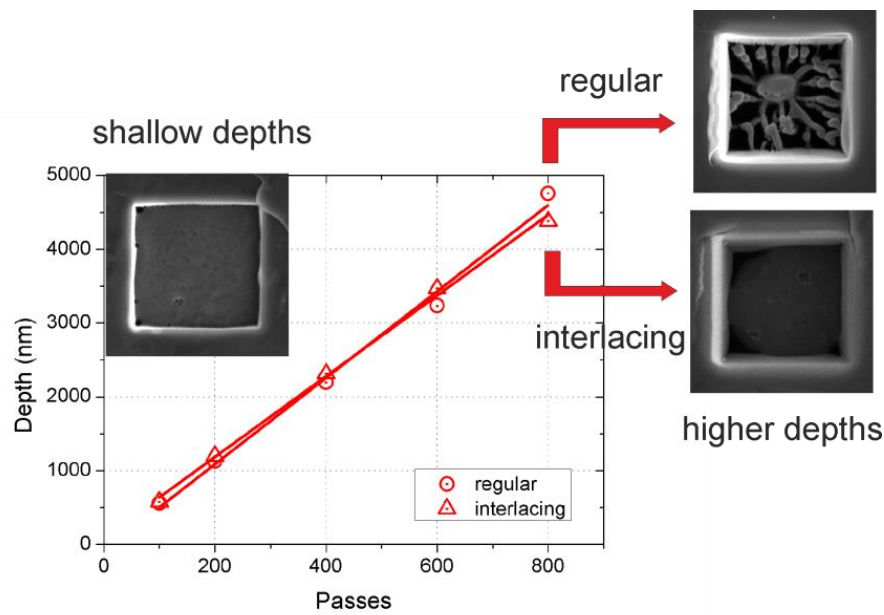


Figure 59: morphological behaviour as the number of passes is increased for both, REG and IL strategies.

4.1.3 Chemical Damage

To evaluate the chemical damage for different polymers during FIB processing via varying parameters, patterning strategies and temperature conditions, Raman spectroscopy has been used. The most critical criteria for such evaluations was the presence of usable Raman peaks. PP, HDPE, PMMA and EVA reveal easily trackable peaks between 2700 and 3000 cm^{-1} corresponding to the stretching vibrational bands of CH_2 and CH_3 . For analyses, the integrated intensity values of the specified bands have been used. Smaller integral values indicate less corresponding bonds in the material and hence indicate greater chemical damage.

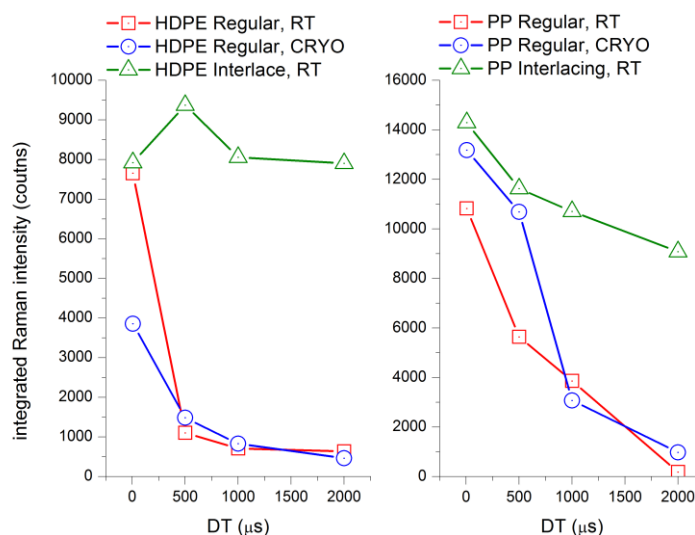


Figure 60: Raman integrals for HPDE (left) and PP (right) in dependency on the DT for regular and interlace strategies at room temperature (RT) and cryo conditions ($-150\text{ }^{\circ}\text{C}$).

Figure 60 shows a direct Raman comparison of HPDE (left) and PP (right) upon DT variation for REG and IL patterning strategies at room- and cryogenic-temperatures. As can be seen cryogenic temperatures (blue) do not prevent chemical degradation as well as interlacing does (green). The interlacing strategy gives a high chemical stability even for the highest investigated DT of 2000 μ s. In this case even cooling the sample to -150°C can't prevent chemical degradation but results in total loss of chemical signature (integral value close to zero)! This happens because of the very low thermal conductivities of soft matter which prevent a sufficient heat removal in between two consecutive pulses in close proximity.

Figure 61 shows the same investigations for EVA25 (left) and PMMA (right) on a logarithmic scale which reveals that for PMMA the degradation already starts for very short DT during regular patterning while IL strategies can maintain the chemical functionality over the full DT range up to the ms range. These results also suggested PMMA as the most sensitive polymer under investigation which was one reason why the second part of this thesis is strongly focused on this polymer as a very challenging material for FIB processing.

In summary, the Raman measurements allow the conclusion that the simple IL strategy is clearly superior to REG processes and can even compensate entirely for cryogenic sample conditions.

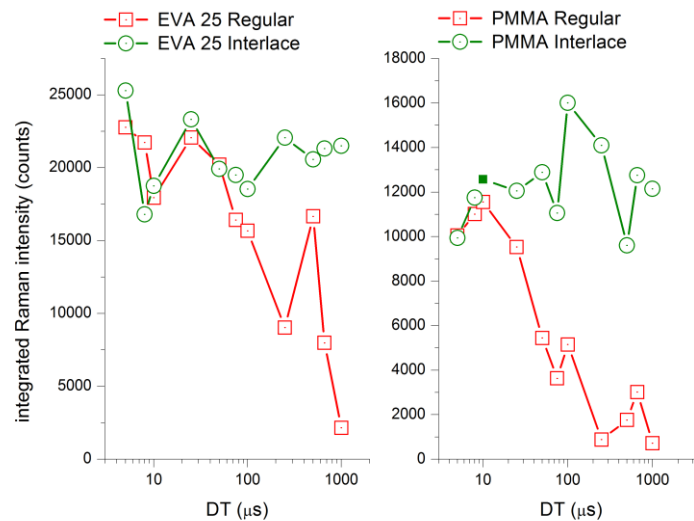


Figure 61: Raman integrals for EVA 25 (left) and PMMA (right) in dependency on the DT for regular and interlace strategies at room temperature on a logarithmic DT scale.

4.1.4 Simultaneous Thermal Analysis (STA)

As initially stated, our primary aim was the expansion of the IL concept to different and challenging polymers on the one hand and the attempt to correlated the process parameters with thermodynamic properties of the polymers used, on the other hand. In particular our primary idea was that the melting points and volatilizing thresholds could be held responsible for the differently appearing effects.

This cannot be done using values from literature, because the thermodynamic quantities vary too much depending on the exact configuration of the polymer. For instance, the variation of values of the thermal conductivity found in literature for the same polymers makes it impossible to make any

reasonable comparison of the polymers' behaviour dependent on that value, because the ranges of values for different polymers tend to overlap over wide ranges. Therefore we could only make comparisons based on measured values from the exact polymers we used. For that we used the STA data (see section 2.4) to obtain the melting point, the volatilizing threshold, and the temperature difference between them. Figure 62 representatively shows STA data from HDPE where the melting point is around 130 °C (yellow block) followed by the range where thermal pyrolysis starts and increases (blue block). Once the thermally induced decomposition produces polymer fragments around 20 carbon atoms and less (volatizing threshold), direct evaporation starts (red block) which is reflected in the mass loss of the material (blue curve).

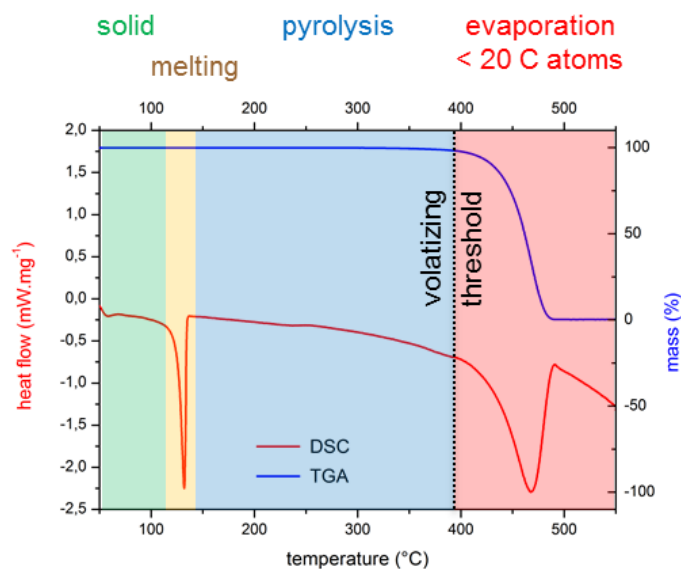


Figure 62: DSC (red line) and simultaneous TGA (blue line) of HDPE. The different states from solid towards thermally induced decomposition and evaporation are also indicated.

By using such investigations for all polymers, three important thermodynamic quantities could be derived: the melting point (**MP**), the volatilizing threshold (**VT**) and the temperature interval in between (ΔT) which are summarized in Table 2 and shown in detail in section 3.4. MPs are defined by the maximum endothermic peak in the DSC signal, while the VT was defined by 2 % mass loss. For EVA the 2 % mass loss criterion was applied to the second decline of the TGA curve, as the first decline corresponds to the formation of acetic acid, which is a cross-linking process (as described in section 3.4.5).

Table 2: melting point, volatilizing threshold and temperature difference between melting point and volatilizing threshold for the polymers used.

	melting point	volatizing threshold	ΔT
	(°C)	(°C)	(°C)
PP	168	365	197
HDPE	130	400	270
PMMA	-	310	310
EVA25	95	429	230
EVA9	78	421	343
PEG	68	330	262

All three quantities represent the last piece for the correlation between process parameters, thermal effects and material properties, discussed in the following chapter.

4.1.5 Process Parameter to Material Property Relationships

As described above, part of the first part was to correlate the process parameters with the qualitative behaviour of different polymers and thermodynamic polymer properties. Concerning the specific removal rate (SRR), which indicates massive heating by a strong increase, the same qualitative dependence on PoP and DT could be seen for all polymers (representatively shown in Figure 63). The slight improvement of morphological stability at cryogenic sample temperatures for REG patterns could also be confirmed, but the enhanced chemical stability was not so obvious for HDPE. Most outstanding is probably the obvious improvement in morphological and chemical stability for all investigated polymers when the interlacing strategy is used. Following these investigations the interlacing strategy seems to be a universally applicable approach for gentle processing of sensitive materials. Hence, the first main achievements of this thesis are:

1. Interlacing strategies can reduce massive local heating by an alternative patterning sequence
2. Interlacing strategies strongly improve chemical stabilities for all polymers investigated
3. Interlacing strategies also reveal superior improvements compared to regular patterning at cryogenic temperatures.
4. Hence, interlacing minimizes technical induced heating effects and thereby morphological instabilities and chemical degradation without the need for cryogenic sample temperatures.

In a second step, the critical PoPs (CPoP) and critical DTs (CDT) are used for the attempt to correlate the process parameters with thermodynamic properties of the used polymers. This is valid because e.g. for increasing DTs the increasing SRR should be reached earlier for materials with lower VTs. Same holds for decreasing PoPs with respect to MPs. Finally, the temperature interval in between (ΔT) is considered as well because it gives information how long thermal pyrolysis needs before the VT is reached. Therefore the CPoPs and CDTs are reasonable quantities for a correlation between process parameters and thermodynamic properties.

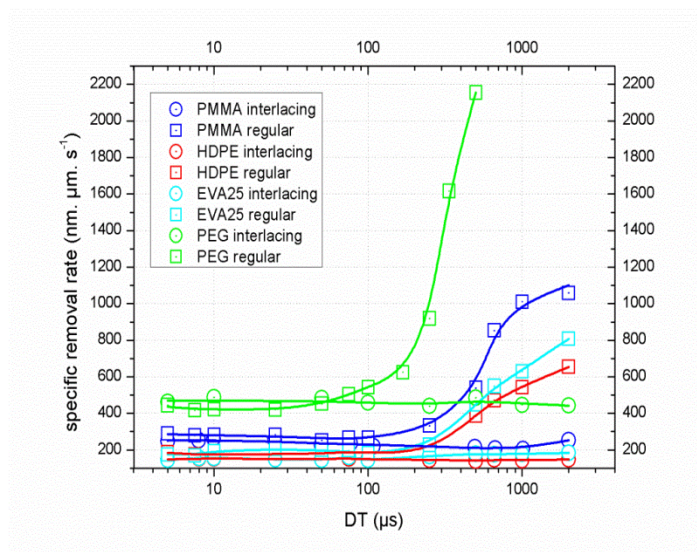


Figure 63: representative DT sweep of HDPE, PMMA, EVA25, and PEG for REG and IL patterning.

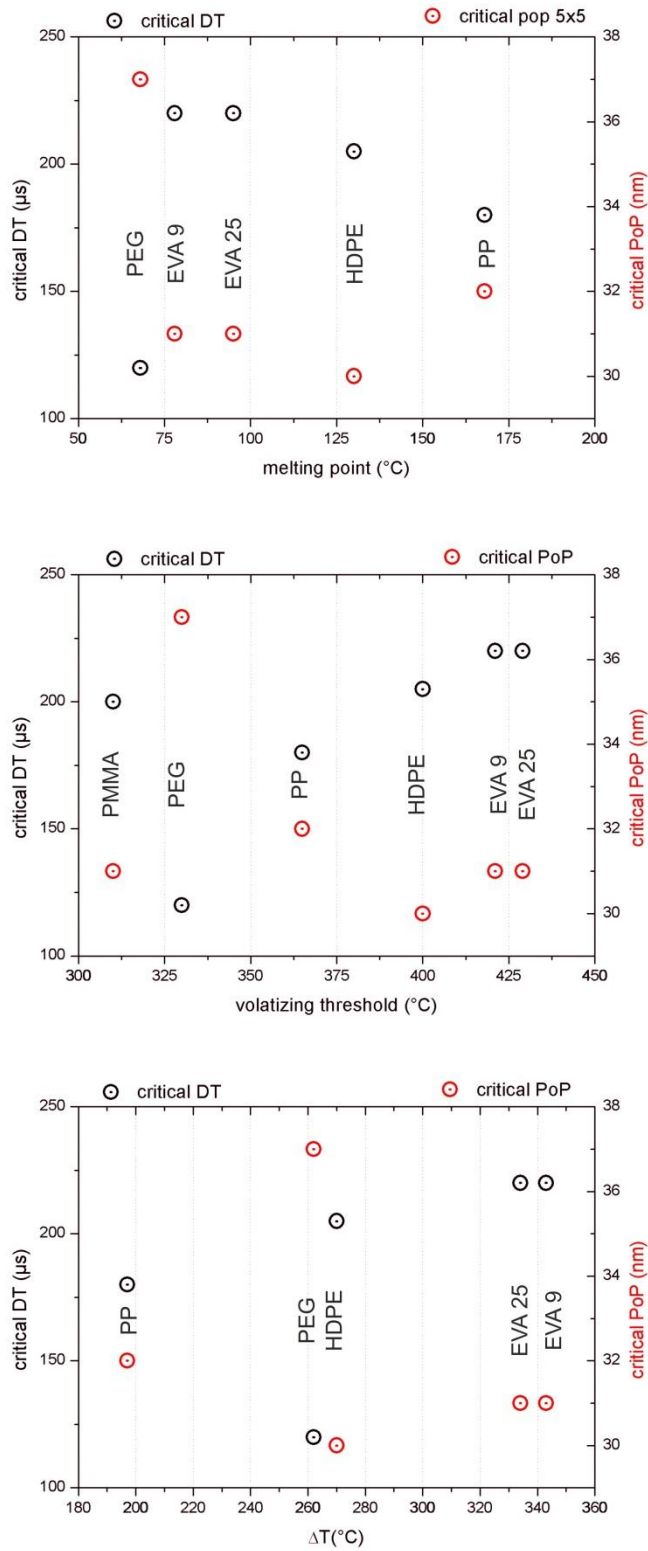


Figure 64: : correlation between critical DT (black and left Y axes) and critical PoP (red and right Y axes) with melting points (top), volatilizing thresholds (centre) and ΔT (bottom).

Figure 64 shows such a correlation with respect to the MP (top), the VT (centre) and the temperature interval ΔT in between (bottom). However, a simple relation between a thermodynamic quantity and CDTs or CPOPs dependence of the SRR could not be found. The first clear detail is that PEG is always behaving very differently. This might be due to the highly crystalline character which will be considered in a following section (chapter 4.1.6). As can be seen in the VT correlation (Figure 64, centre) the argument that lower VTs should result in lower CDTs does not hold: the material with the lowest VT (PMMA) has a rather high CDT of 200 μs and also the CPOp cannot be correlated to the volatilizing threshold, as HDPE has the lowest CPOp and at the same time a very high VT (400 $^{\circ}\text{C}$). Same holds for the MP correlation (top graph in Figure 64) where e.g. the most stable polymer (PP) reveals the second lowest CDT of about 180 μs , and also other high melting materials have low CDTs. Also the temperature interval ΔT in between (bottom graph in Figure 64) as a measure of required pyrolysis heat amount towards the VT does not give clear (monotone variation) correlations.

These surprising results therefore suggest that the observed effects are not exclusively driven by the thermodynamic properties of the material used.

Hence, another component must be strongly involved. At this point, it is necessary to not only focus on the SRRs but also on the detailed morphology obtained for different materials via different FIB process parameters as discussed first in chapter 4.1.2. For this purpose a first detailed look will be taken at the most deviating material: PEG.

4.1.6 Special Details

As discussed in the previous section, PEG deviated strongly from all other polymers. So far only SRRs have been considered in detail together with chemical behaviour described by Raman measurements. But at the same time very interesting observations concerning the morphology were made, mostly when regarding SEM images. A special candidate for special structures is PEG, which is known to be crystalline for the molecular weight we have used in our study (see section 3.4). Figure 65 shows a PEG film imaged with light microscopy where the birefringence causes the varying colours in the image. As can be seen a high number of spherulites can be observed, different in size with a closely packed character.

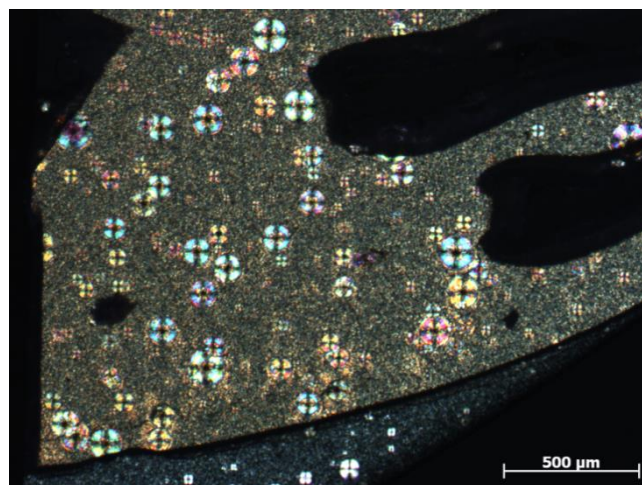


Figure 65: PEG film on SiO_2 substrate imaged via light microscope revealing the birefringent spherulites via multiple colours.

When first DT and PoP sweeps were performed on such PEG films there were two immediate discoveries. First we realized that the removal rate is far higher than it was for the other materials, which is most likely caused by the crystalline order and the easy removal of the atoms (mainly oxygen) or short molecules fragments which tend to order themselves regularly.

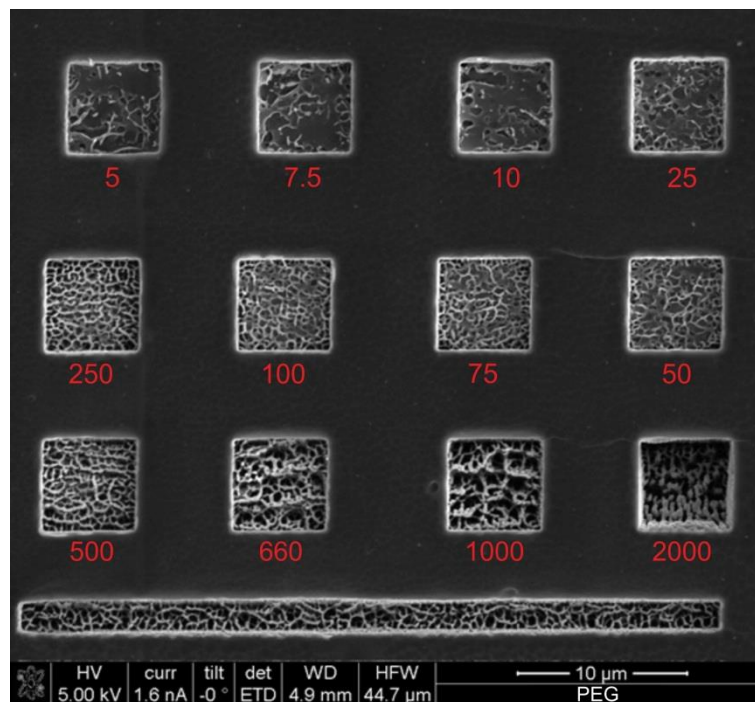


Figure 66: different morphological structures appearing for a DT-sweep on PEG at a PoP of 50 nm. The DTs are indicated in red below the corresponding structures.

The second immediate observation was the very pronounced morphologies that appeared at the bottom of the structures. Figure 66 shows the usual DT-sweep performed with a PoP of 50 nm. Here different structure types can be observed along increasing DTs: networks, rods and walls. Figure 67 shows part of a DT-sweep performed with a PoP of 60 nm. In this image the rod-like structures can clearly be seen. The circular arrangement of the rods reminds of the spherulites and suggests a connection, as the spherulites can also be seen on the surface of the sample in Figure 67.

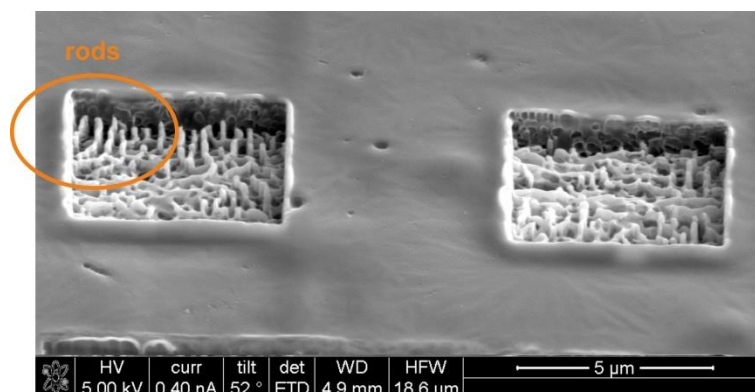


Figure 67: rods appearing in 5 x 5 μm square structures on PEG with a TET of 64 s. The PoP used was 60 nm. The DTs equalled 250, 100, 450, 750 μs (from left top to right bottom).

Dedicated DT experiments at the border of a spherulite did not show any difference in their overall SRR which was slightly unexpected (see Figure 68). AFM investigation of same areas clarified the situation afterwards. Figure 69 shows the AFM height image of a spherulite and of the apparently amorphous region next to it. What seemed to be amorphous in the light microscope and the SEM, proved not to be. Instead there were many small spherulites. Therefore it made sense that there was no difference in the DT-sweeps performed in those two regions, because the entire surface consists of densely packed spherulites of different sizes

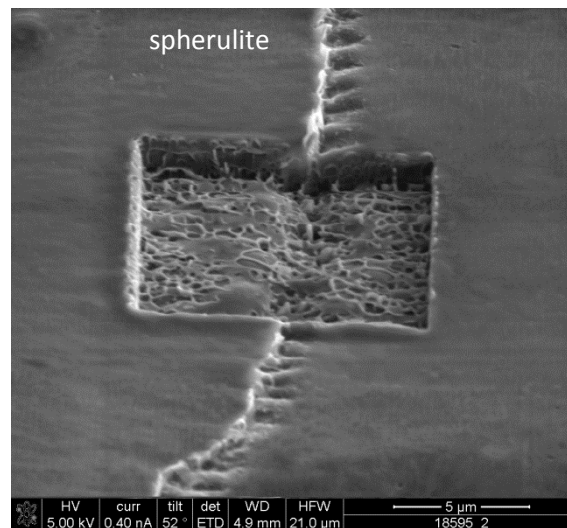


Figure 68: SEM image of a structuring experiment across the border (vertical bended line) of a spherulite. No clear difference beside the morphological border reflection could be found.

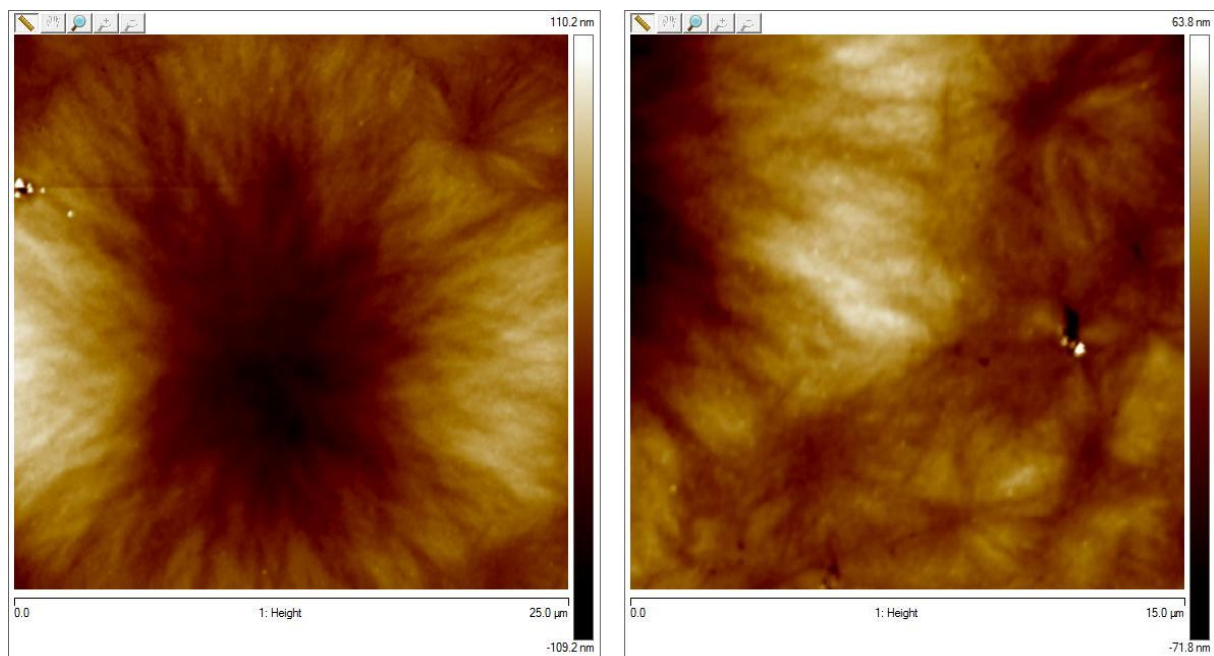


Figure 69: AFM height images of a spherulite (left) and of the apparently amorphous region next to it.

Hence, we assume that the free standing rod-like features after FIB processing (see left side in Figure 67) are caused by poly-crystalline areas as it is well known for FIB processing of inorganic materials such as gold or copper [REF].

Nevertheless, the inhomogeneous structures and the relation to its inner structure motivated to take a closer look at other materials, in particular PMMA, where similar structures have been observed under certain conditions. As shown in Figure 70 by a direct SEM comparison of CL - HDPE (upper row) and SC - PMMA (lower row), the resulting morphologies after identical REG preparation parameters are very different. After more detailed experiments we could basically divide the polymer behaviour into three different stages:

1. (widely) flat → further denoted as phase 1
2. rugged → further denoted as phase 2
3. volatized → further denoted as phase 3

In the given example HDPE reveals only phase 1, followed by phase 3 for very high dwell times (>500 μs). In contrast, PMMA reveals phase 1 only for short DTs followed by phase 2 which changes from a hole like appearance towards a rod like morphology for intermediated DTs. For very long single pulses, the morphology changes into phase 3, where volatizing takes over completely. Hence, a difference in the internal (chemical) structure during processing is assumed which could play a major role for all effects observed in this chapter.

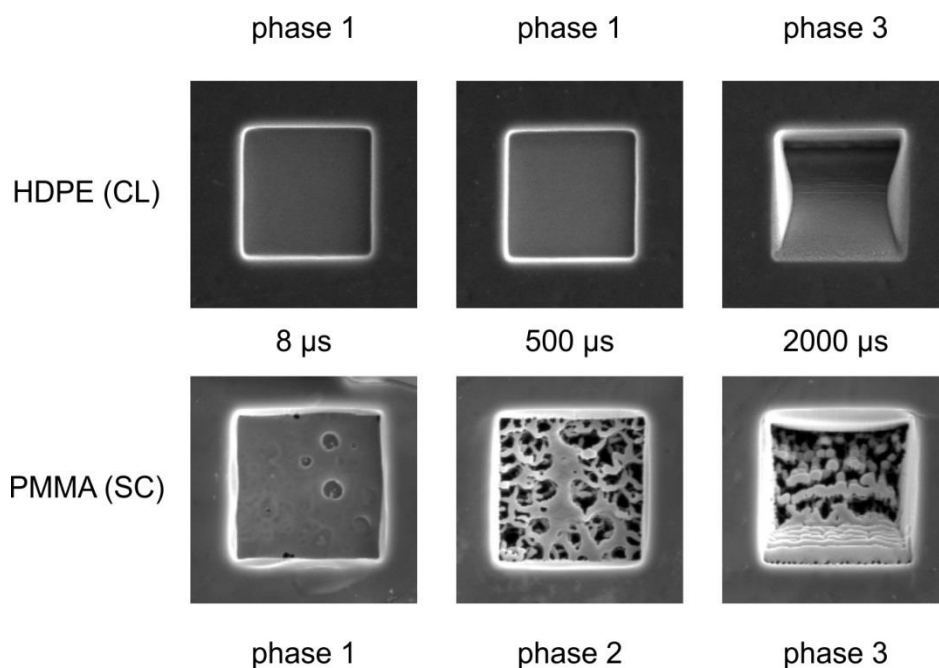


Figure 70: direct SEM comparison of HDPE (upper row) and PMMA (lower row), structured via REG strategies with identical TETs and and PoPs while the DT increases (indicated). The images reveal the individual phase changes (from left to right) and the big different between CL and SC materials.

4.1.6.1 Material Creeping

A closer look at the special phase 2 for PMMA gives the impression that the material undergoes liquefaction in a first step, followed by selective material creeping and subsequent cooling as representatively shown in Figure 71. Such a phase transition in a liquid-like state requires two effects: **1)** the polymers have to be short enough and **2)** the local temperatures have to be high enough to enable a material creeping. Both effects are conceivable by thermal pyrolysis (shortening of the polymer chains) and local heating (movability). These basic ideas lead to the formulation of a new hypothesis, which will be subject of the second part of this investigation.

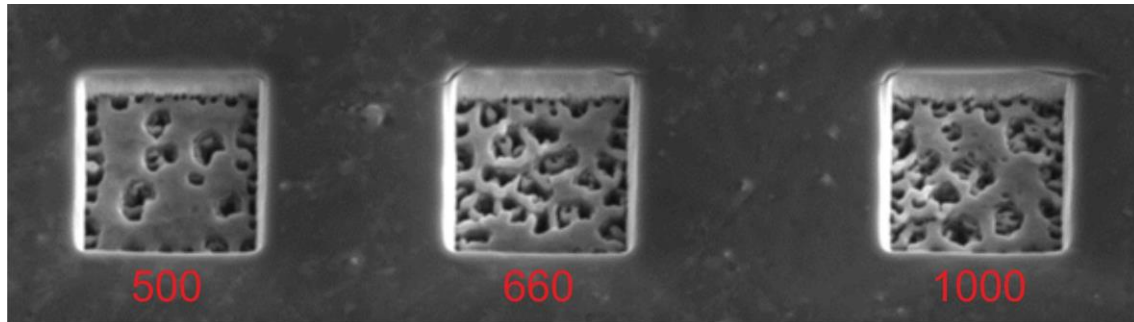


Figure 71: 5x5 μm structures in PMMA with 500 μs (left), 660 μs (centre) and 1000 μs (right) and a PoP of 40 nm revealing the morphology which reminds of quasi liquid materials.

4.2 Correlation 2 – Chemical Processes as Major Influence

4.2.1 Introduction

In the first section, only the rise in temperature due to heat accumulation and its direct effects on the original material, like volatilizing, were considered. Therefore a crucial mechanism was neglected – the modification of material in the proximity of the beam due to heat accumulation. It needs to be considered, that the volume exposed to the beam is mostly not pristine, but modified, due to the high temperatures it has been exposed to, when the beam was nearby.

A follow-up effect is that the material in the proximity of the beam is not homogenous. Depending on the scanning strategy, the material close to the beam may show different degrees of modification and partly be pristine. This may lead to different effects depending on the material that is being structured.

Basically, we can divide into two basic polymer types when evaluating their behaviour when FIB processing with respect to high temperatures and the presence of electrons / ions:

1. Polymers that rather **cross-link** giving the **morphological structure more stability** \rightarrow further denoted as CL materials
2. Polymers that rather **scission** which leads to very instable morphologies due to **short and mobile fragments** \rightarrow further denoted as SC materials

This difference – as will be shown in the following - can clearly be seen at medium DTs, where the volatilizing regime is not yet reached.

We will also show that the interlacing strategy can reduce negative effects caused by the material modification mainly because heat accumulation is avoided, but also because negative effects of the asymmetry of the material in the proximity of the beam are avoided.

4.2.2 Formulation of the Hypothesis

To better understand the following hypothesis, the DT sweep experiments on PMMA were repeated for different PoPs. As shortly mentioned before, three **morphological** regimes of material modification due to heat accumulation and particle interaction can be defined. Let's first regard a DT-sweep at a PoP of 20 nm shown by the central column in Figure 72:

1. *Phase 1*: at low DTs the morphology stays stable → flat morphology
2. *Phase 2*: at medium DTs a very active regime is reached → rugged morphology. The material seems to become liquid. Holes appear first followed by the formation of a rod like morphology. Forces of cohesion seem to govern the material by local dewetting effects.
3. *Phase 3*: at very high DTs the volatilizing regime is reached → volatilized. As the removal rate rises drastically, the resulting deep structure is not at all flat.

It should be mentioned that as soon as a higher temperature regime is reached, all the lower temperature regimes will be present too. The lower temperature regimes will definitely be present at greater depths, but may also be present at the surface. This simultaneous presence of differently modified material can lead to very weird morphologies, like for example the structures in Figure 67 or Figure 71.

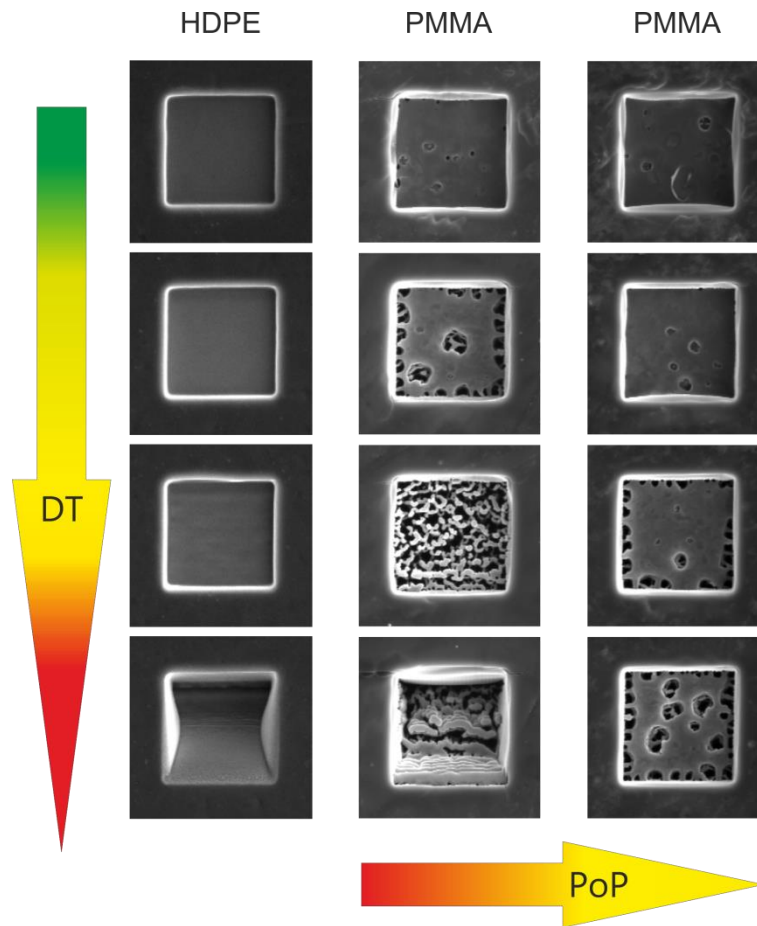


Figure 72: SEM images of structures where different patterning regimes have been reached.

If the PoP is increased, the same regimes appear but they are shifted towards higher DTs. The last column in Figure 72 shows a DT-sweep at increased PoPs of 60 nm. In this case the volatilizing regime is not reached and the active *phase 2* regime appears at higher DTs.

In this context it is very important to note that PMMA (centre and right column in Figure 72) is known for its SC properties which mean chain scission between the melting point and the volatilizing threshold.

In contrast, HDPE is shown in the left column of Figure 72 and reveals only two morphological regimes: *phase 1* (flat) and *phase 3* (volatized). As HDPE is a cross-linking polymer and cross-linking stabilizes the morphology, the active *phase 2* regime cannot be distinguished from the stable regime. The results are still flat surfaces as long as the volatilizing threshold is not reached which explains the difference for PMMA and HDPE during increasing DT as shown in Figure 72. The volatilizing regime, which appears at high DTs, is clearly visible due to the inhomogeneous structures.

All in all we now have to combine the morphological regimes (*phase 1, 2, 3*) with the two classes of polymers (cross-linking and scissioning) and postulate a hypothesis by means of **patterning regimes**, which needs to be tested in this second part of the thesis.

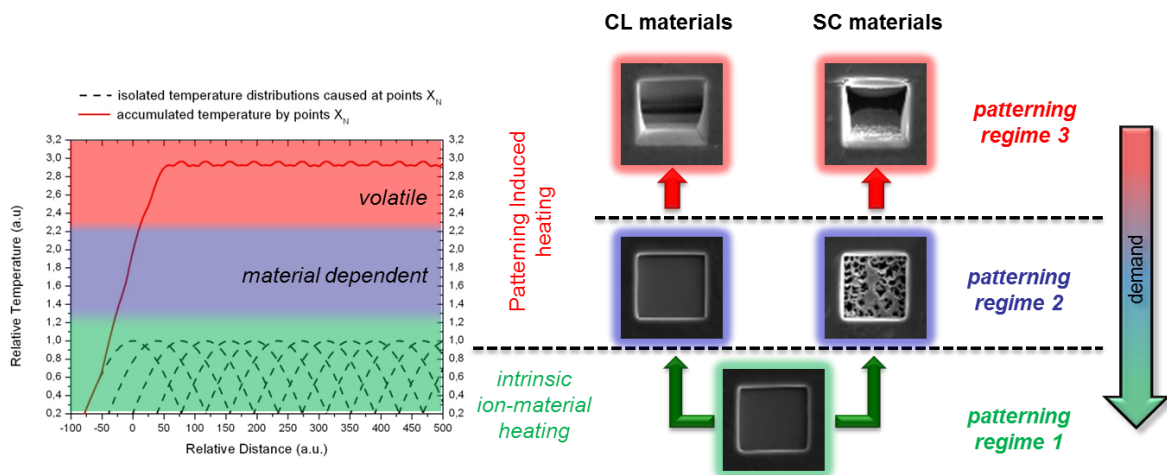


Figure 73: the three patterning regimes; for a more detailed description please read the main text.

Figure 73 shows the total summary of effects and assumptions leading to **three different patterning regimes** for different polymer types. The main source of technical heating is shown on the left by the proximity heating and the entailed heat accumulation. This increases the temperature from the intrinsic ion-material heating for single pulses (green block) to a range where the material is chemically / structurally modified (blue block) and finally beyond the volatilizing threshold where the material is evaporated independently of the chemical / structural modification (red block). Depending on the material type the three patterning regimes can be defined which are indicated on the right hand side in Figure 73:

1. Patterning Regime 1 (**PR 1**): If the temperatures are kept low, the material is modified according to the intrinsic ion-material interaction during a single pulse, and the resulting structure shows a stable morphology (Figure 73; SEM-image bottom). The related RR is rather low.
2. Patterning Regime 2 (**PR 2**): If the patterning conditions are such that the resulting temperature is well above the temperature reached by intrinsic events, the removal rate stays also low, but the material is strongly modified (Figure 73, marked in blue). This modification depends on the type of material:
 - a. Cross-linking (see section 3): This type of modification forms a macroscopic network, the modified material is a **gel** and its morphology is stable and even improved compared to the pristine materials (Figure 73; SEM-image middle-left).
 - b. Scissioning (see section 3): Here no network is formed. On the contrary, the material is cut down in smaller and smaller fragments and forms a **sol**. The movability (creeping) increases for shorter chains and higher local temperatures and it shows liquid-like behaviour (Figure 73; SEM-image middle-right).
3. Patterning Regime 3 (**PR 3**): If the temperature exceeds the volatilizing threshold of the material, temperature assisted evaporation takes place in the proximity of the beam (Figure 73 marked in red). In this regime the RR rises dramatically and the material shows unwanted morphologies (see Figure 73 top SEM-images). Deep trenches appear which at the bottom don't represent the intended structure at all.

Regardless of the material type, the demand for ideal processing is clear and shown by the arrow on the right hand side in Figure 73: The local temperatures during processing have to be kept as close as

possible to the intrinsic temperatures for single pulses (**PR 1**) in order to prevent volatilizing (**PR 3**) and reduce material modification (**PR 2**). However, before that can be done, an improved understanding of **PR 2** has to be developed to verify the hypothesis which will be discussed in the following sub-chapters.

Emphasis is put on PMMA due to the assumption of arising creeping effects in the **PR 2** as a consequence of thermal pyrolysis and the entailed short chain fragments.

4.2.3 FIB Parameter Variation

4.2.3.1 Dwell Time Influence

Figure 74 shows a DT-sweep on PMMA with a constant PoP of 20 nm. For DTs up to about 10 μs the structures are flat, the morphologies seem stable and we are working in the **PR 1**. A closer look reveals small holes that appear at the edges of the structure. With rising DTs, more and larger holes appear at the edges indicating the transition **PR 1** \rightarrow **PR 2**. At a DT of 50 μs first holes appear in the middle of the pattern and the material becomes more and more porous with further increasing DTs indicating the **PR 2**. At 250 μs the structure is dominated by small rods and one might see slight indication of a predominant horizontal direction which will play a major role in the following chapters. With a further increasing DT the VT is reached and the pattern works in the **PR 3**.

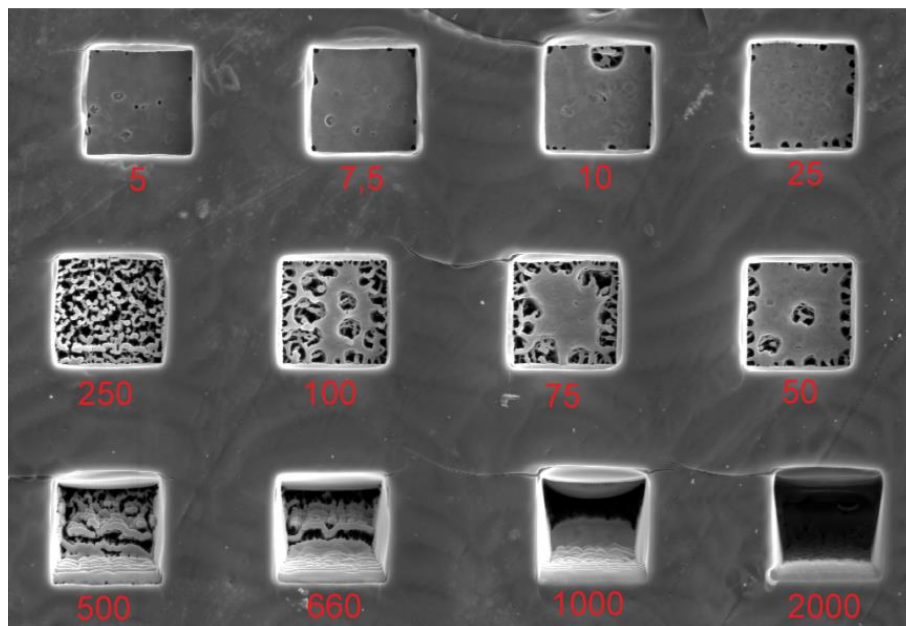


Figure 74: DT-sweep on PMMA with a square size of 5 x 5 μm and a 20 nm PoP. The red numbers indicate the DT in μs .

Trying to understand what is happening to the material in detail, is the next step. One major question is, whether the structures appear because of intrinsic beam or patterning parameters, or whether they are a result of molecular forces within the material. Another question is, whether what can be seen at the bottom of the squares really is quasi-liquid during patterning and if so, whether this is because patterning doesn't only cause high temperatures in the proximity of the beam, but globally

raises the temperature above the MP. Here it is important to note that due to the distribution of polymer lengths upon thermal pyrolysis there is not only one MP any longer but a whole MP range towards lower temperatures with the maximum at the intrinsic MP of PMMA.

4.2.3.2 Refresh Time (RT) Influence

To separate a global heating effect from local heating in the beam proximity as origin for the observed structures a special experiment is needed. A simple experiment includes multi-pass patterns of 8 passes each with different refresh times (RT) in between. If global warming is an issue, a clear difference between zero RT (no intermediate cooling) and a long RT (cooling between individual passes) must be seen since the heat is allowed to dissipate.

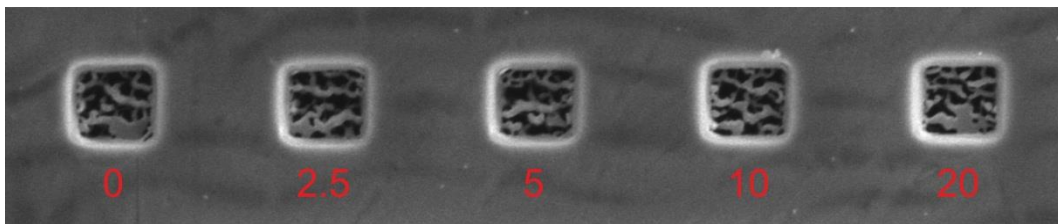


Figure 75: refresh time experiment on PMMA; indicated in red are the refresh times (in seconds) that have been left as a pause between consecutive passes; $2 \times 2 \mu\text{m}$ squares were patterned with DTs of $250 \mu\text{s}$, 8 passes, and PoPs of 20 nm.

Figure 75 shows the described experiment at a PoP of 20 nm consisting of 8 passes in total, each. The red numbers indicate the RTs in between the individual frames. As can be seen, no difference in morphology can be found for increasing RTs which is equal to reduced global temperatures. Same experiments have been performed with increasing PoPs which should improve the heat dissipation even further.

These experiments suggest that the morphology cannot simply be explained by a global increase in temperature. Therefore, a more localized effect must be involved.

4.2.3.3 Scan Direction Influences

Due to the outcome of the previous section that local effects are involved, different experiments have been designed to investigate the influence of the beam and its movement. In more detail we have to differ between molecular forces (e.g. cohesion) and intrinsic beam / patterning parameters. The first approach to distinguish between those two mechanisms was to do the same experiment on a larger length scale. The idea was to increase the size of the patterning fields, but at the same time increase the PoP and adjust the beam current and diameter (via defocus), so that the local ion dose stays constant. The new experiments were supposed to be the same DT-sweep as before, just magnified to a square size of $15 \times 15 \mu\text{m}$.

The hypothesis was that if the effects come from the beam, the resulting morphological structures should grow with the adjusted parameters and the resulting image should basically look the same. If, in contrary, the structures result from molecular forces within the material, they should not grow

with the pattern size, and therefore should appear to be smaller, if the enlarged pattern is regarded at an adjusted magnification.

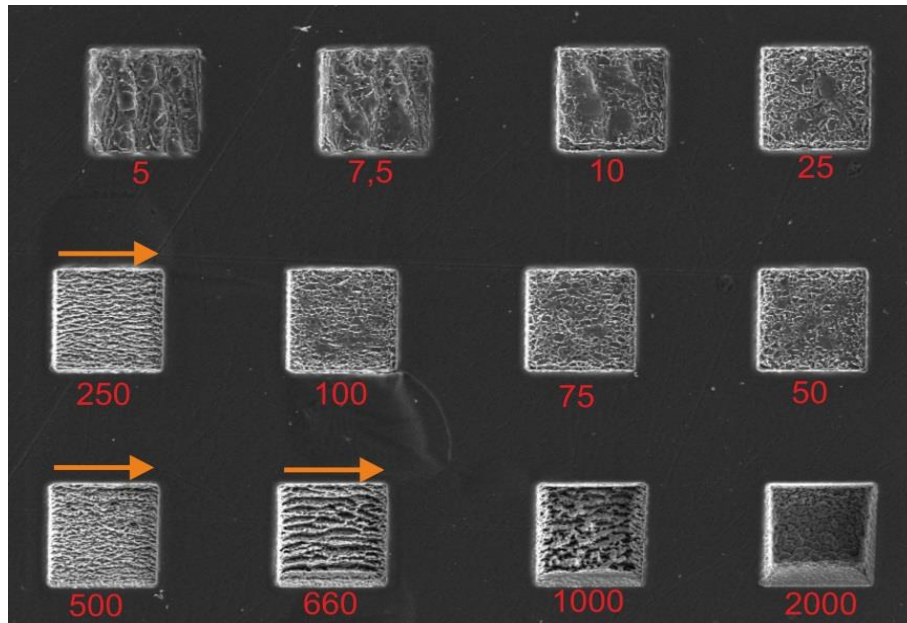


Figure 76: DT sweep on PMMA at a larger length scale (square size: $15 \times 15 \mu\text{m}$); the red numbers indicate the DTs in μs ; the orange arrows indicate the fast scanning axis.

Figure 76 shows a representative result of such experiments. At first glance one might immediately conclude that the effect is not caused by the beam. The morphological structures do not grow with the adjusted beam parameters, so they are a result of molecular forces. At second glance however, one will again see a predominant horizontal direction in the structures at some DTs – which corresponds to the fast patterning scan axis. It is very clearly visible at a DT of $660 \mu\text{s}$, in Figure 76. This suggests that the effect cannot only be reduced to material properties, but that there are at least influences of the beam and its movement.

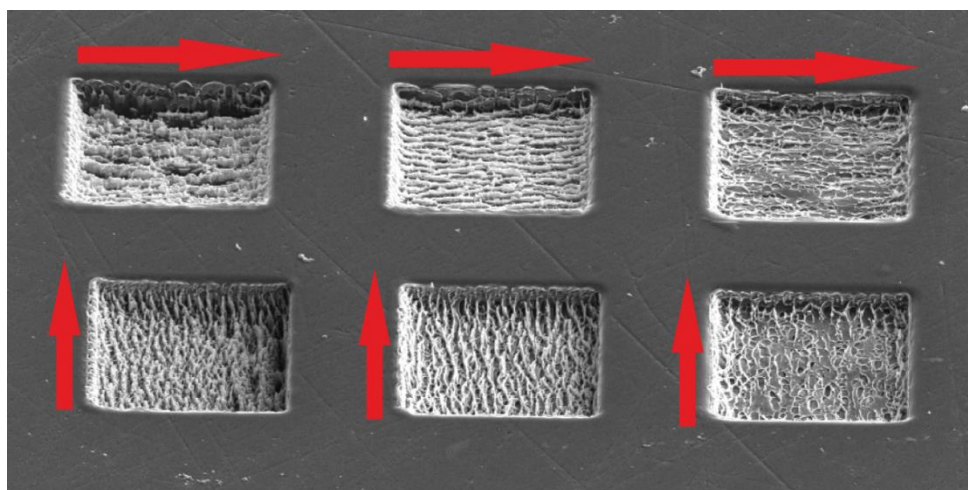


Figure 77: $15 \times 15 \mu\text{m}$ squares on PMMA at DTs of 500 , 250 and $100 \mu\text{s}$; the fast scan axis is indicated by the red arrows. A predominant direction of the morphological structures corresponding the fast scan axis of the beam is clearly visible.

To clearly link this predominant direction to the fast scanning axis of the beam, patterns were made, at corresponding DTs where the fast scanning axis was rotated by 90°. Figure 77 shows the representative outcome of such an experiment which fortifies the influence of the beam movement. As can be seen in Figure 77, the fast patterning axis – indicated by red arrows – plays a major role during patterning, independently on the used DTs.

Such experiments suggest that **1)** the beam movement itself has an influence and consequently **2)** the material somehow follows the ion beam during patterning.

4.2.4 Material Creeping

As mentioned in section 2.1.13 and 4.1 it must be considered that the heat accumulation in the proximity of the beam has follow-up effects by means of a material dependent modification. The structures in Figure 76 and in Figure 77 were fabricated using a classical serpentine patterning strategy as shown in Figure 78a. We are now trying to relate the patterning strategy - with typically used PoPs – with the beam diameters and the entailed effects as the beam moves from one line to the next. We focus on a cross section according to Figure 78a, which is then shown from left to right in b-f together with segmented material blocks for an easier understanding. White blocks mean pristine material, while modification is indicated from green over yellow to red for strong modification. In which way the material is modified depends on the type of polymer, and will be discussed later. In this first approximation we ignore sputtering and thermally assisted material evaporation and focus only on general polymer modification due to single, double and triple exposure of the scanning ion beam. Figure 78b shows the main axis of line 1 (L1) together with the ion beam profile with a box segment width of about 20 nm. The beam profile is on purpose underestimated to keep things easier [29]. As can be seen, three blocks are modified after the first run along L1. After patterning L2 (Figure 78c) some material parts are modified for the first time (right green segment) while two segments are modified for the second time, indicated by the yellow blocks. We now consider what happens during the third line L3. Once again only the neighbouring lines are influenced by the beam, so L1 and L5 remain unchanged. The lines affected again are L2, L3 and L4. While line four is only slightly modified (as it was pristine in the previous time step), line three changes from slightly modified to modified (yellow), and L2 changes from modified to strongly modified (indicated in red). When we now proceed to scanned lines L4 and L5 we end up in the situation as shown in Figure 78f where we can see two effects:

1. Due to the typically used PoP of about 50 % to 80 % of the beam diameter the material is not only irradiated once. This leads to a multiple material modification as the beam patterns the sample. This leads to point 2:
2. An asymmetric material modification is the result with respect to the ion beam moving direction as shown in Figure 78f: the left hand side is strongly modified while the right hand side is only slightly and not modified at all, respectively.

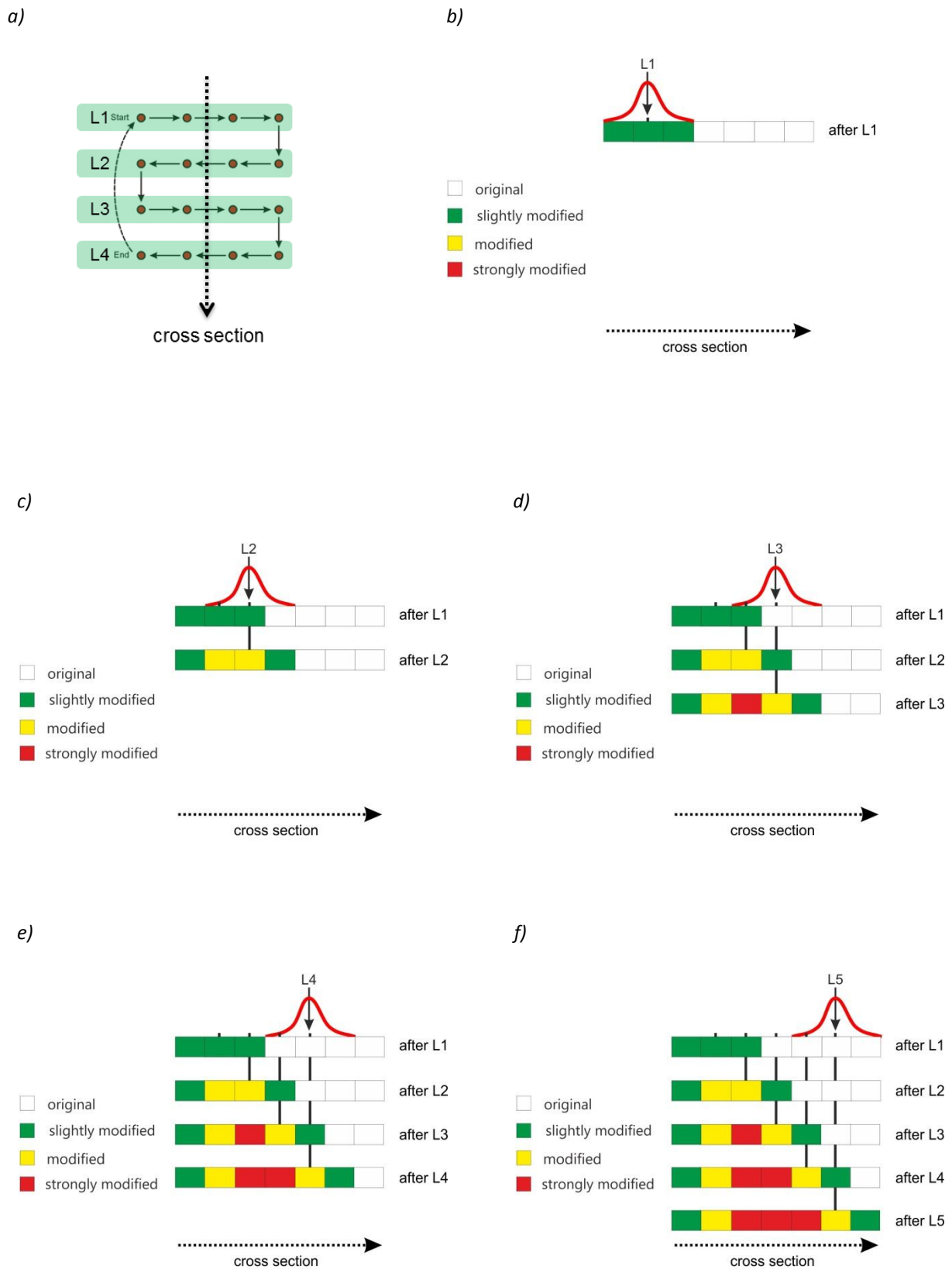


Figure 78: modification of material during patterning. For more details please read the main text.

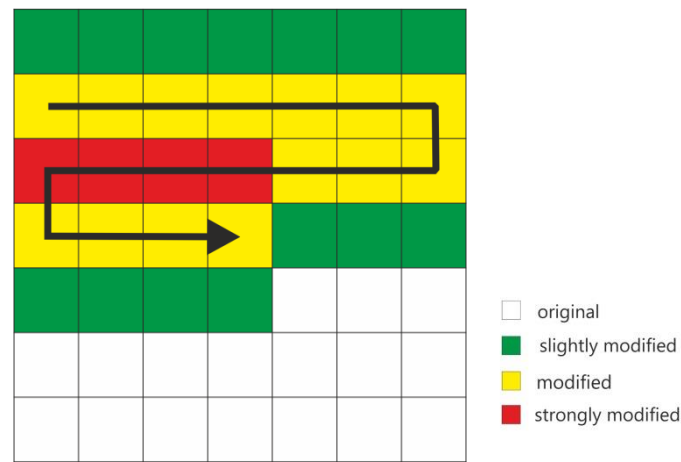


Figure 79: degrees of modification around the beam during patterning of line 4; the black arrow marks the beam movement and position.

This asymmetry becomes even more obvious considering the situation from top with the same colour coding as shown in Figure 78. Here one can see the bottom right area is not modified at all while varying degrees of material modification due to multiple exposures can be found in the upper region. In the proximity of the beam there is also an asymmetry in the direction of the fast scanning axis. If the line the beam is moving in and the adjacent lines are regarded, the material on the left is modified to a greater extent than the material on the right.

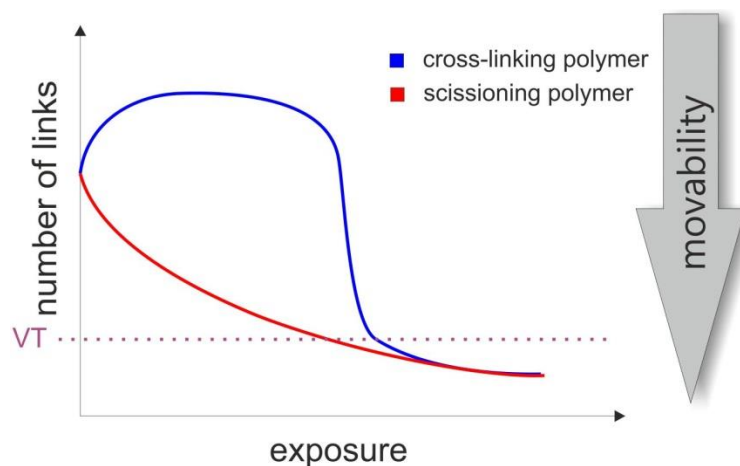


Figure 80: qualitative behaviour of the number of links in the polymer depending on the type of polymer

Before we can draw any conclusion and link these ideas with the experimental results in section 4.1, the material modification itself has to be considered since it depends strongly on the type of polymer used. As described in section 3.4 and 4.1.5, we can basically divide polymers into two main classes when talking about the following temperature and particle induced effects: **1) cross-linking of (CL)** materials which increases the number of links and thereby stabilizes the material morphologically; and **2) scissioning (SC)** of polymers, where bonds are broken continuously, therefore generating shorter and shorter polymers with decreasing melting points, leading to increased movabilities. For very high temperatures close to the volatilizing threshold (VT), cross-linking effects for CL materials are counteracted by increasing scissioning resulting in thermally assisted evaporation above the VT. Therefore, temperatures above the VT lead to a total loss of bonds and results in evaporation.

Figure 80 qualitatively shows how the number of links depends on the exposure for both material classes. The higher the number of links, the more the structure corresponds to a **gel**. The bonds connect the polymer chains to form a network on a macroscopic level. Its behaviour is solid-like. If the number of links is small, the material corresponds to a **sol**. Its behaviour is liquid-like (see also section 3.2). CL materials (blue curve in Figure 80) show first an increase of bonds for increasing exposure (=modification and temperature) followed by a fast loss of bonds when chain scission takes over completely. Once, the VT is exceeded (horizontal line) the material volatilizes. In contrast, SC materials show a continuous decrease of bonds as shown by the red curve in Figure 80.

With these details we finally can interpret the experimental results for different materials together with the asymmetric material modification for different material classes.

But that is not the only thing that happens. If we regard the beam proximity while the beam is somewhere in the middle of the pattern we realize that two effects govern the material. On the one hand, there is an asymmetric distribution of differently modified material around the beam. Figure 78 and Figure 79 show the degree of modification in the beam proximity. On the other hand, the beam elevates the temperature in its proximity.

For CL materials the modification means that a network forms across the structure which stabilizes it. Figure 81a shows the asymmetric degree of material modification (w.r.t. the beam direction) after a higher number of lines. The more modified the CL material, the more stable it gets. This means, that the material around the beam is solid- to gel-like to different degrees. The rise in temperature will further cross-link the material as long as the VT is not approached, which mostly leads to very flat morphologies (bottom SEM image in Figure 81a) due to strengthened material networks.

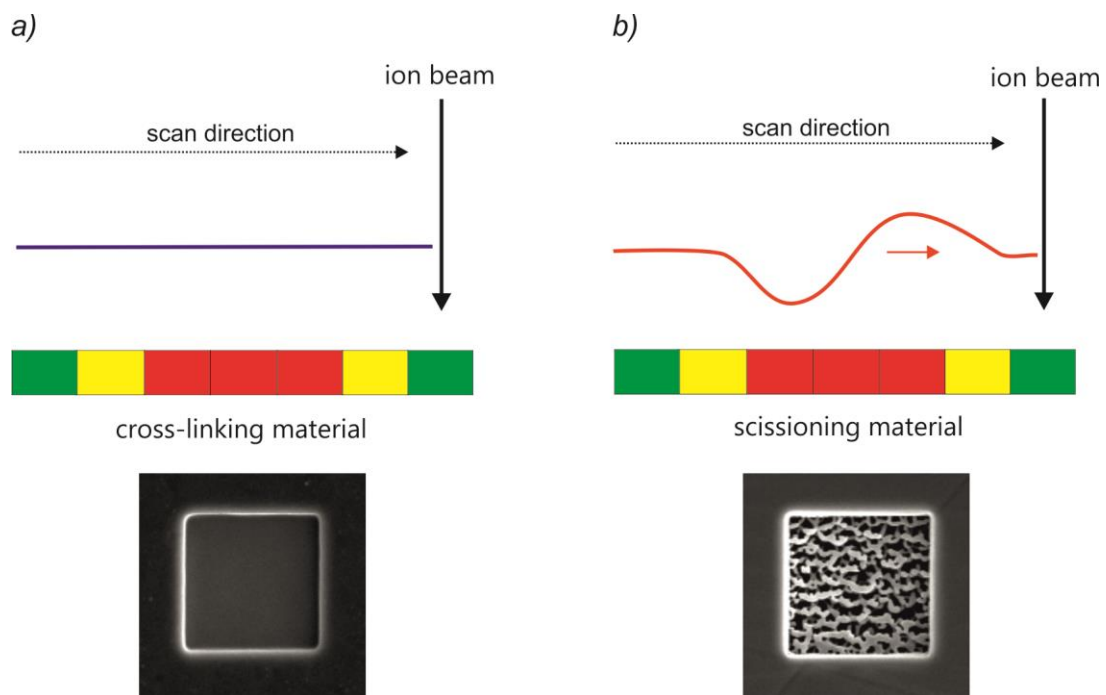


Figure 81: formation of morphological structures due to material modification for cross-linking polymers (left) and scissioning polymers (right).

The situation is total different for SC materials as schematically shown in Figure 81b. Here, multiple exposures lead to an increasing breaking of chemical bonds. The polymer is cut down into shorter and shorter fragments. The behaviour of the material becomes more and more liquid-like (sol phase) with the degree of modification. The mobility rises, and due to cohesive forces, which pull the quasi-liquid sol parts of the material together, to minimize the surface energy, the surface gets more and more unstable. The degree of modification, and therefore of how liquid-like the material is, is furthermore not symmetric around the beam. Its (simplified) distribution is displayed in Figure 79b by the red line.

At the same time the temperature is elevated in the proximity of the beam. This increase of temperature also has the effect of increasing the mobility of the molecules even further. This region of high mobility moves with the beam since within this region cohesive forces make the material creep together in order to minimize the surface energy. Due to the beam movement these forces add up to a force that drags the liquid material behind the beam up to a certain point where the structures become too large and stop following. This effect will be referred to as the **creeping effect**, in the following discussion.

The creeping effect can lead to very different structures, depending on the patterning conditions such as DTs (=exposure) and PoPs (range of proximity modification) due to varying spatial distribution of material modification.

For classical patterning strategies like serpentine strategies, the beam movement is clearly reflected due to the creeping effects described above, as evident from Figure 77 and Figure 79b at the bottom. But also the temperature reached due to heat accumulation, which of course also depends on the patterning strategy as well as on other factors, like for example the point pitch and the dwell time, influences the resulting structure. A variety of different structures due to these factors can be seen in the dwell time sweep in Figure 74. The appearance of these structures is reproducible. Low dwell times always lead to quite flat structures. Rising DTs lead to more and bigger holes and the central still connected areas can be explained by cohesion driven forces of similarly modified materials while the contact to the structure edges is less attractive based on the chemical difference. In the region of the VT the beam movement is clearly visible. The fragments are very short, so the mobility is very high, and at the same time volatilizing starts. The interplay of these processes leaves very unusual structures which are often observed and shown in literature but barely explained or even investigated in more detail before. At higher DTs volatilizing becomes the dominant effect. Larger point pitches shift the appearance of these regimes to higher DTs, as shown in Figure 72 by the central and right column. This is also in agreement with the processes described above since increased PoPs mean less modification in the beam proximity and thereby a reduced mobility compared to smaller PoPs at same DTs.

Expanding these basic ideas to an IL patterning strategy used, the situation is different in 3 ways: **1)** heat accumulation is strongly reduced as extensively discussed in the first part of the thesis (chapter 4.1). Therefore local temperatures are lower, and the material is not modified to such an extent. **2)** the beam does not move along neighbouring positions consecutively, but hops from one point to another one which is further away, so the material cannot follow the beam via the creeping effect. **3)** when a neighbouring point X2 is patterned, the point X1 is cooled down to a great extent (which is one of the key elements of IL) which reduces the mobility in X1 therefore reducing creeping

effects towards the beam. However, the effects and even further improvements of the IL strategy based on the ideas in this chapter are discussed later in detail (chapter 4.3).

The next step is the verification of the creeping effect by means of special scanning strategies and according simulations which is topic of the following sections.

4.2.5 Further Experiments at the Dual Beam Microscope

- 1) To test the previously described hypothesis of the creeping effect some further experiments were set up: a serpentine patterning with an increasing Y increment (REG strategies)
- 2) a Zig Zag pattern (REG strategies)
- 3) a spiral in pattern (REG strategies)

4.2.5.1 The Variable Y (VY) Increment

The idea behind the variable-Y (**VY**) experiment was to create a structure that would allow us to see the influence of consecutive line spacing during patterning. As it is well known from literature (see section 3.4), HDPE represents an almost exclusively cross-linking material while PMMA is a classical scissioning material. Hence, this experiment was performed on HDPE (CL) and on PMMA (SC). The pattern was built up as follows: the PoP in X-direction was kept constant at 20 nm, while the line distance in the Y-direction was increased by 20 nm after each line beginning with 20 nm between line one and two. The pattern had a size of 5x5 μm . These experiments were carried out at different DTs and numbers of passes for a general overview. Figure 82 shows a representative single-pass comparison of PMMA and HDPE with a DT of 4000 μs . At the top of the structure, greater depths were reached in both cases, which is because the increased beam overlap (small line spacing in Y) leads to:

- A higher sputter rate due to an increased number of ions per area
- The resulting heat accumulation

Once the Y spacing becomes larger the total depth is reduced and for HDPE, as the CL material (left image in Figure 82), the first separated lines are found around 200 nm line-to-line distance. Afterwards the structures are defined due to the morphological stabilization through temperature / particle induced cross linking. In contrast, PMMA, as the SC material (right image in Figure 82) shows a much less defined overall appearance and its critical distance is found to be about 220 nm line-to-line distance. In general, a clear difference between the CL and the SC material becomes obvious. While for the CL polymer the edges are clearly cut at any line distance, the SC polymer shows changing behaviour: while the edges are quite clearly cut for big line-to-line distances, at short line distances the proposed liquid-like appearance occurs. This can easily be explained by the theory described above: while for big line distances both materials are only slightly modified, at short line distances they are both strongly modified. But the effect of this strong modification is a different one for the two classes of materials. HDPE shows improved morphological details because the material cross-links as long as the VT is not exceeded.

In summary, we can extract from these experiments the critical line-to-line distance needed to prevent mutual effects from one line to the next. This is of essential importance for the following and essential zigzag patterns.

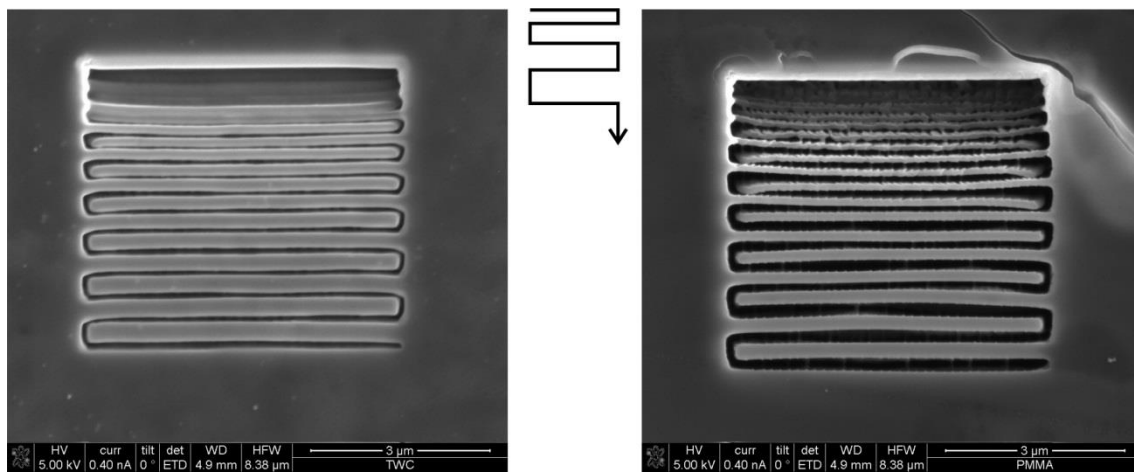


Figure 82: variable-Y (VY) serpentine pattern on HDPE (left) and PMMA (right) at a PoP of 20nm and a DT of 4000μs. The central inset represents the basic idea behind the VY strategy.

4.2.5.2 The Zigzag (ZZ) Pattern

The idea behind the Zig Zag pattern (**ZZ**) is to artificially create clearly traceable regions of different degrees of modification of the material, which is displayed in Figure 83 (same colour coding as for Figure 78 and Figure 79). If the hypothesis of the creeping effect holds, the ZZ pattern must show major differences between CL and SC polymers.

We shall now consider what happens, if the beam moves along such patterns starting from the corner top left. During the first line (L1) the material is only slightly modified along the entire path (green). But as the beam returns the material at the edges is further exposed to the ion beam. In the region very close to the edge the tracks of the beam overlap entirely. Therefore the material which already has been modified will be modified further. It's an interplay of two effects, which makes the modification at the edges the strongest. The reason for both is the actual overlap or closeness of the beam tracks. One effect is that the bigger the overlap (or the closer the beam tracks), the more modified the material already is, when it is exposed to the beam again (from green over yellow to red depending on the local track distance). The other is that the closer it is to the edge, the smaller the refresh time (RT), which equals zero exactly at outmost positions. The RT is relevant to avoid heat accumulation – which again leads to material modification. So while the beam moves from the edge back to the centre along L2 the areas modified in L1 depend on the distance and the RT and lead to the situation that temperatures at the outmost edge areas are very high while both effects, proximity modification and heat accumulation, decrease strongly towards the central line areas if the according line-to-line distance is sufficiently large (experimental design).

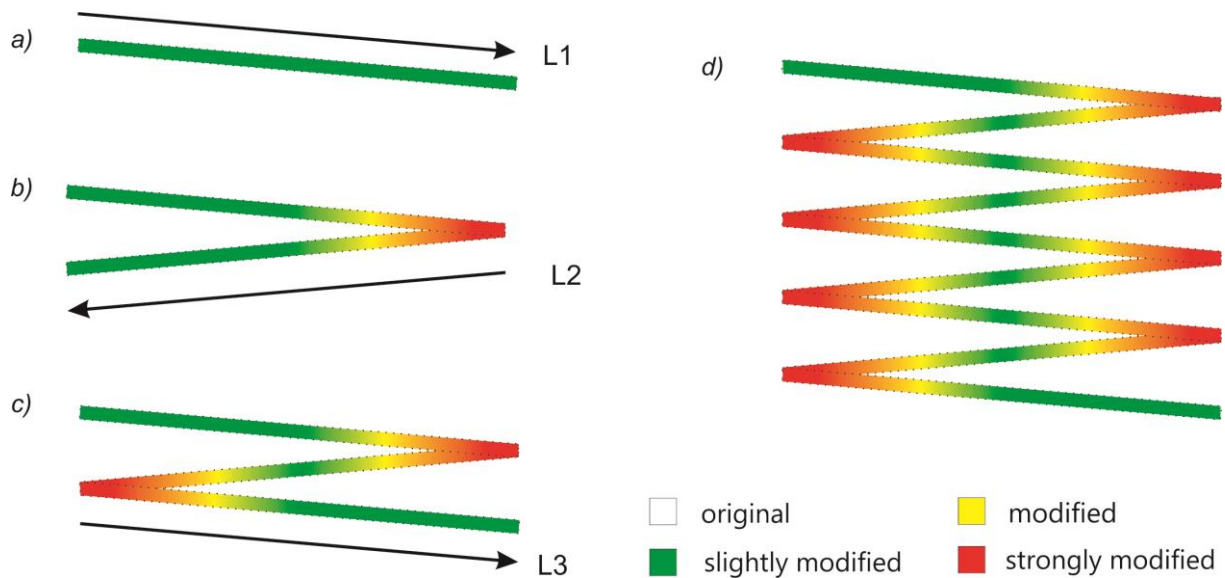


Figure 83: gradual proximity material modification in a zigzag pattern via REG strategies (consecutive sequence); development of laterally varying modification after the first three lines (a-c) and the resulting modification map (d) with vertical stripes of different material modification.

If the theory of the creeping effect holds, we should see a difference between CL and SC material for such patterns. What we expect to see for the CL material is a clear-cut zigzag structure which might have deeper cut edges because of the beam overlap and the entailed temperature increase, but it should not show any signs of material movement. For SC material we expect to see deep structures at the edges too, due to same effects as for CL materials. However, at the transition areas towards the centre we expect to observe signs of material creeping toward the middle of the structure.

The materials used for the experiments were again HDPE (CL) and PMMA (SC). Figure 84 shows two resulting structures for a single pass ZZ pattern via REG strategies with 20 nm PoP and 2000 μ s DT. The structure width is 5 μ m and the vertical edge to edge spacing was set to 400 nm as a result of pre-experiments concerning the critical interaction distance.

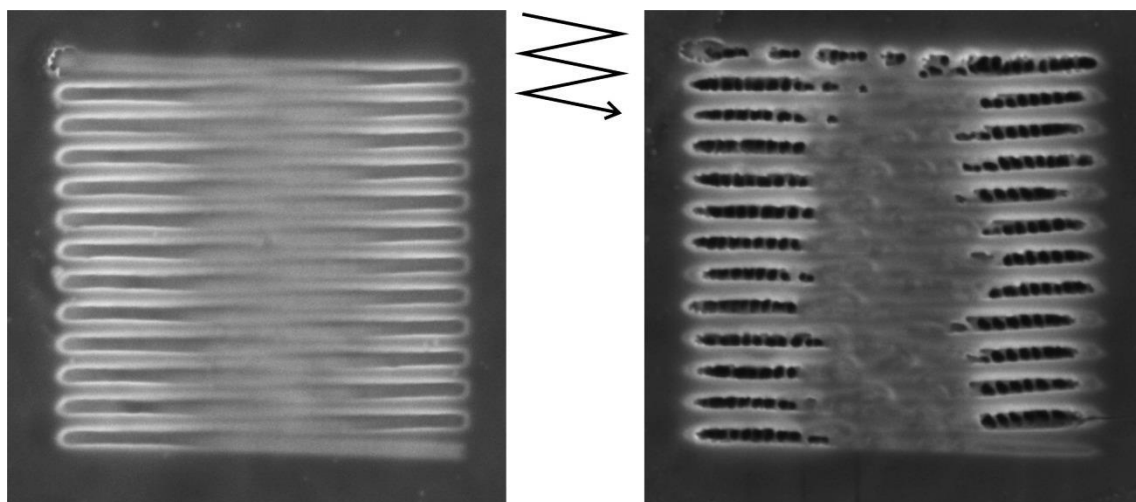


Figure 84: zigzag (ZZ) structure (5 x 5 μ m) on HDPE (right) and PMMA (left), with an edge to edge spacing of 400 nm, 20 nm PoP and 2000 μ s DT. The central inset represents the basic idea behind the ZZ strategy.

As can be seen in Figure 84 at the left, HDPE shows a clearly sputtered zigzag pattern. The lines are deeper at the edges compared to the central parts, which can be explained by the overlap of the beam of neighbouring lines, leading to double exposure as described above. A very close look at the ends of the first and last line, which are not double exposed reveal that the resulting depth is very similar to the central parts of the structure, which confirms the assumptions mentioned above. On PMMA (shown on the right in Figure 84) the structure of a zigzag pattern is basically visible but not as homogeneous as on HDPE. At the edges the structures appear to be very deep, as expected result of an exceeded VT. When following the lines towards the centres, it is evident that there is a big lake of material without any noticeable line structure. This is the result of the decreasing temperatures towards the centres where the material becomes scissioned, mobile and follows the patterning beam on the one hand and stays together because of cohesion forces on the other hand. The lake-like appearance furthermore suggest that although the beam is moving, the temperature remaining at the centre is always high enough to allow creeping and cohesively driven material agglomeration. Please note that the homogeneous appearance of the central part along the Y axis suggest strongly that redeposition may contribute but is definitely not the main source of this structure.

To support this assumption of this central creeping phase according temperature simulations have been conducted which are discussed in following section.

4.2.5.3 ZigZag (ZZ) Pattern Simulations

DI Roland Schmied (FELMI) performed finite element (FE) simulations which provided a spatially resolved temperature distribution during single ion events. The obtained results were numerically fitted and combined with Monte Carlo simulations of the ion beam trajectories [14] enabling temperature distributions upon single pulses. These results could then further be used to simulate entire patterns and the entailed temperature distribution and evolution on the surface, again neglecting sputtering effects in first approximation. The results of a ZZ pattern simulation are shown for specific points in Figure 85 (upper row) together with the experimental results (bottom SEM image). The simulation paths are indicated by fine lines and the last scanning line is indicated by a black arrow.

When the ion beam starts the last line on the right side (top right), one can see the hot spot around the beam which follows the line towards the centre (top centre) and finally to the end of the line (top left). The interesting part, however, is that the simulations always show an asymmetric temperature distribution towards the central part of the structure. This indicates a permanent heat residue in the middle as a result of previous line scanning. This essential finding is in agreement with the explanation of the creeping effect resulting from a rise in mobility due to an interplay of short polymer fragments and elevated temperatures, and cohesive forces. In the SEM image (bottom) one can see that different temperature regimes are reached simultaneously. In the edges, where there is a maximum beam overlap, the volatilizing regime is reached. Closer to the middle, the material is very mobile as described above. The elevated temperature suggested by simulation is then the explanation why the material is somehow covering the central part due to thermally assisted creeping behaviour. Together with the background idea (section 4.2.2), the experimental results (section 4.1), and the simulations described here, the presence of this creeping phase is very likely and in agreement with all experiments conducted during this master thesis. However, a final pattern

has been designed and will be discussed in the following which should support the presence of a creeping phase even further: the spiral in pattern.

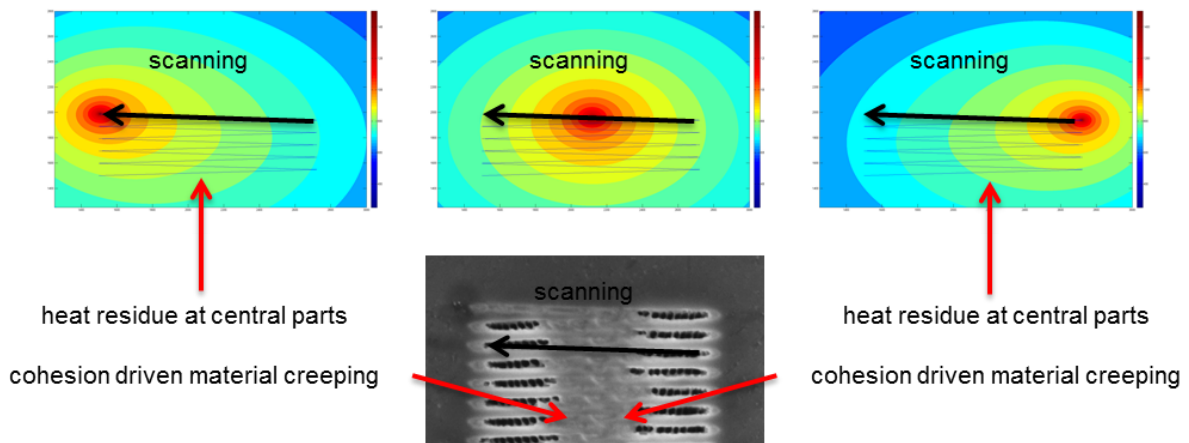


Figure 85: the three images above show simulation results for the zigzag pattern, where (from left to right) the beam is on the left, in the middle and on the right and the beam has moved through the indicated zigzag pattern. At the bottom there is an SEM image of a FIB-structured zigzag pattern. The creeping effect can clearly be seen.

4.2.5.4 Spiral-In Pattern

The idea behind a spiral like pattern lies in the fact that if a creeping phase follows the structuring beam a special set of parameters should be found which make this effect clearly visible. In those experiments a square was patterned, with constant PoPs in X and Y direction. The beam movement however is spiral-shaped from the outer frame to the centre. If the theory of the creeping effect holds, we should observe the creeping effect very clearly towards the centre of the resulting spiral-in square structure on an SC material.

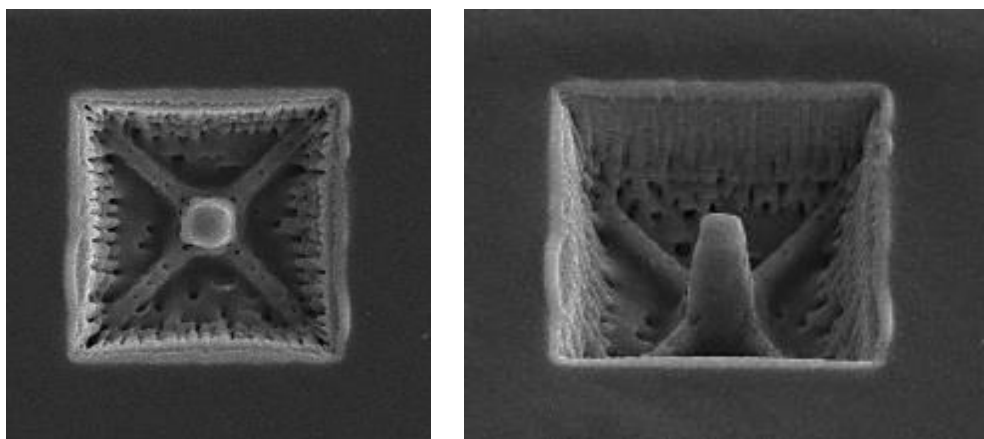


Figure 86: 5x5 μm square in PMMA patterned by spiral in patterns with 660 μs DT and 20 nm PoP in a single frame REG strategy. The left image shows a top view while the right image gives the same structure at a tilted angle.

Figure 86 shows the result of the spiral-in experiment on PMMA in a top view (left) and in tilted arrangement. As can be seen there is material remaining in the centre and in a cross from edge to edge. The last effect is a result of the pattern since those points experience a higher temperature because the beam changes its direction and modifies the material in the beam proximity stronger compared to straight lines in between. The results are also higher temperatures remaining where the scissioned material is pulled together because of cohesion forces. The second and even more important fact, however, is the central structure. Although the beam patterned till the very centre there is a very high structure remaining. This structure comes from the fact that the creeping phase follows the beam towards the centre more and more and results in a free standing structure of molten material which cools down after structuring.

This experiment is more or less a direct visualization of the creeping phase, which follows the beam and based on the continuous spiral movement without contact to the edges. It is even possible to observe the formation live during a DBM experiment. Please note, due to the spiral-in character, redeposition can be completely neglected for the formation of the central structure.

4.2.6 Raman and STA

The previous experiments which all had the morphological behaviour as their subject are in good agreement with the hypothesis of a creeping phase, and that we need to distinguish between two classes of polymers, when their behaviour during FIB processing is concerned. As there is no reason to reject our theories from a morphological point of view, we now go to the next step and see whether the theory also holds if we take a look at the chemical behaviour.

We decided to perform Raman measurements again, this time in more detail. We chose to perform a measurement over a DT sweep of a cross-linking (HDPE) and a scissioning (PMMA) polymer, once using a regular serpentine patterning strategy and once using the interlacing strategy with an ILD of 100 nm. The regular PoP equalled the final PoP and was 20 nm.

As described in section 2.3 the integral value is proportional to the number of bonds. Therefore, if what we stated during our morphological studies, namely that in a CL polymer more bonds (or links of another nature, like crystalline parts) are formed while the material is modified by the elevated temperatures in the proximity of the beam, whereas in the SC polymer bonds are rather broken under the same conditions, we should see a difference in the Raman integral according to the conceptual scheme in Figure 80. We expect that the CL polymer stays rather stable until the volatilizing regime is approached and exceeded, while we already expect to see degradation at medium temperature regimes for the SC polymer.

Even though we have already done Raman measurements of interlaced DT sweeps (see section 4.1.4) we decided to do those again, also in more detail. In this case we expect the signal to stay fairly constant if the theory of IL holds.

The Raman integral was again performed over a region of $2700\text{-}3000\text{ cm}^{-1}$, corresponding to the material characteristic CH_2 and CH_3 peaks. To check our theory the C-C peaks would have been more suitable, as we expect main chain scission for PMMA, however, this peak overlaps with many others and the background is very high in that wavenumber region. Therefore it's not possible to measure

these bonds directly and we chose to use the peaks we used in former experiments, which could easily be isolated.

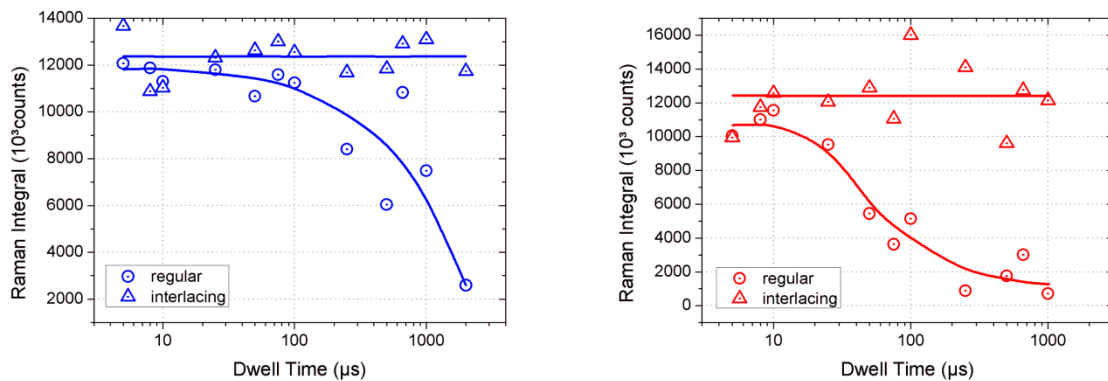


Figure 87: Raman integrals during DT sweeps for HDPE (left) and PMMA (right). Circles represent the values for regular patterning while triangles show patterns done with the IL strategy at an ILD of 100 nm. The (final) PoP used equalled 20 nm.

As can be seen in Figure 87, the results for REG patterns (circles) are in agreement with the suggested behaviour in Figure 80. The CL polymer (HDPE on the left) stayed stable until the volatilizing regime was reached indicated by strong decrease. In contrast, the signal of the SC polymer (PMMA on the right) starts to decrease right from the beginning and continuously approaches zero values. Please note the logarithmic scale. Also for the IL patterns our expectations were confirmed for both materials. In the investigated DT range the interlacing pattern keeps the material in a temperature regime, where it stays chemically stable. The use of the interlacing strategy seems to keep chemical degradation during the structuring of very challenging SC polymers at a minimum, close to the intrinsic limit.

This supports strongly the suggested mechanism difference between CL and SC polymers during FIB processing from a chemical point of view.

4.2.7 Second Conclusion – Chemical Processes as Major Influence

Morphological and chemical characterization via different experiments and simulations suggest strongly that we need to differentiate between two classes of polymers, depending on their tendency to increase or decrease their number of links during temperature / particle interaction. This division of materials in two classes, cross-linking and scissioning, in combination with the theory of gelation described in section 3.2 gives a good understanding of the behaviour of material during FIB processing. It becomes clear that if the number of links is high enough to form a network spreading over macroscopic dimensions, the material can be defined as a gel, will act rather solid-like and therefore be morphologically far more stable than a material that does not have enough links to form a macroscopic network (defined as a sol) and therefore is able to flow and act like a viscous liquid. The sol is mobile and governed by cohesive forces and the urge to minimize the surface energy, and if exposed to the elevated temperatures in the beam proximity will experience enhanced mobility and be subject to the creeping effect.

The model derived in this section can explain the often observed, rugged and irregular structures after FIB processing by experiments and simulations. However, a final aspect needs to be addressed concerning the cohesion tendencies at elevated temperatures and the IL patterning approach, which is discussed in the final part of this master thesis.

4.3 The SIL-Engine

Inspired by the advantages interlacing brings, the motivation to find a way to interlace ANY structure, independently of the shape, its size and the material used, arises. The idea to create a program that can interlace any bitmap or stream file is born. It was created using Matlab [30].

For various reasons we chose that the DTs and XY positions of points to pattern would be ordered and saved as lines in a matrix. Then the positions of those lines would be altered to change the patterning sequence. The resulting vector would be saved as a stream file, which can then simply be loaded by the microscope software which then controls the ion beam positioning directly.

There are two main demands to the strategy that should be kept in mind, and also be fulfilled, for any pattern:

1. Heat accumulation due to proximity effects should be avoided (see section 2.1.13).
2. Creeping effects should be avoided (see section 4.2.4).

Considering that ANY pattern should be interlaced, it is not enough to simply form a grid over the pattern as shown in Figure 18 and alter the sequence respectively for existing points. That is, because for sparse patterns it could happen that neighbouring points are again patterned consecutively, or within a too short time. A simplified example of such a case is shown in Figure 88 where the points to be patterned are indicated in grey while the classical interlacing segmentation is overlaid. While the image on the left gives the interlacing frame numbers and the point sequence within the frame (1.1, 1.2, ..., 2.1, 2.2, ...), the image on the right gives the final point sequence based on this segmentation. In this case only one point in the first frame (1.2) is found followed by two points in the second frame (2.2 and 2.3). In the final point sequence (right graphic) 1.2 and 2.2 are adjacent points in directly consecutive order. While the third point (2.3) in the final point sequence is at a sufficient distance from the previously patterned points, the fourth and fifth point are very close to points patterned within a short time. This eliminates the advantage of the IL approach and leads to heat accumulation problems as for REG patterns, or in very critical cases, even the creeping effect might occur. Therefore the patterning points histories' need to be checked! What we introduced in order to be able to do that is the critical radius (**CR**) and a refresh time (**RT**), which can be chosen by the user.

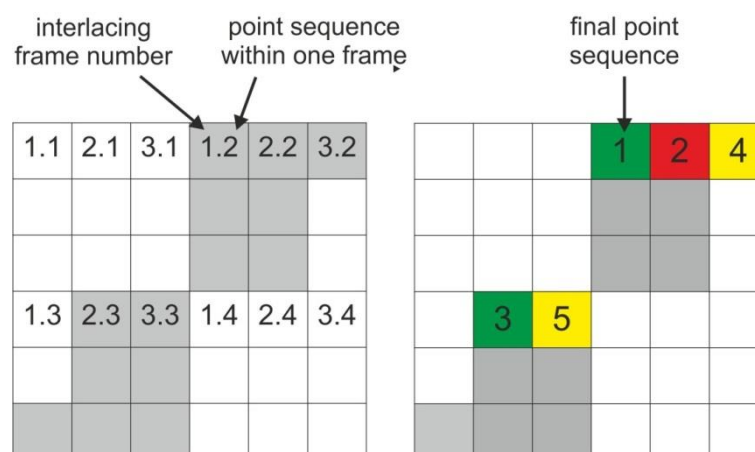


Figure 88: example for a pattern where neighbouring points are patterned consecutively even though the most simple interlacing segmentation is used. Points to pattern are indicated in grey. For explanation see details in the text.

The conversion program can be divided into two main parts. The first is the simple rearrangement of patterning points according to the basic IL strategy. During this process the history check takes place, and patterning points that don't fulfil the CR and RT criteria will be sorted out and treated later on. In the second part of the program, all points that have been sorted out will be sorted in again, in a way that the CR and RT criteria are fulfilled for all the points. The criteria make sure that the two main goals of the interlacing strategy (as mentioned above) are fulfilled.

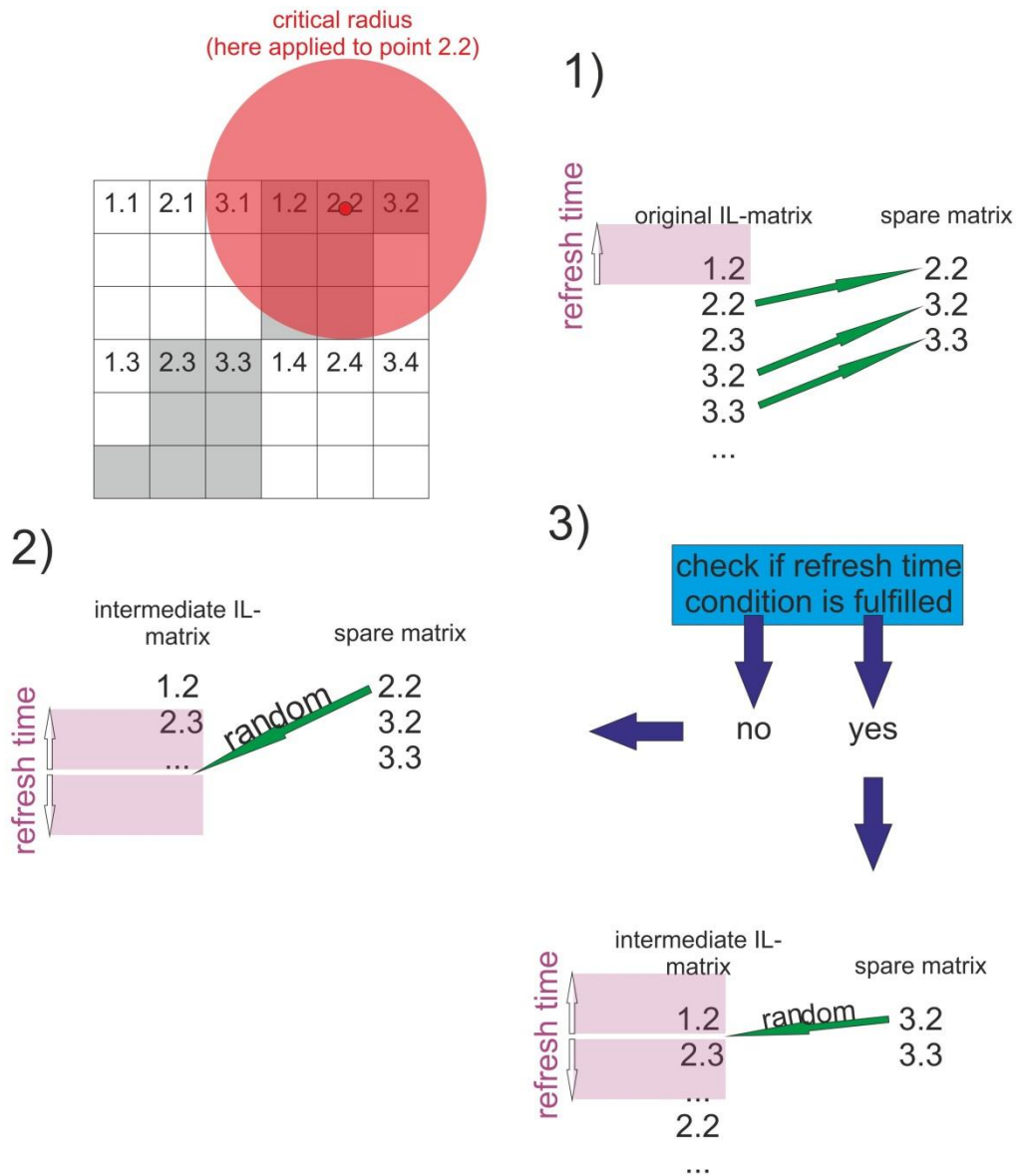


Figure 89: schematic of the history check and rearrangement process during smart interlacing processing.

What is checked in the program for a point to pattern is that within the RT no point has been patterned within the CR of previous points. To this coupled condition we will refer as the refresh time condition (RTC). In case this condition is not fulfilled the vector of DT and XY position of the point to pattern will be written into a spare matrix. After all the patterning points have been interlaced, the patterns from the spare matrix are sorted back into the output matrix point by point. Every point is

at first randomly positioned in the patterning sequence. Then the RTC is checked for both, points patterned in time steps before and after the point in question. If it is fulfilled in both cases, the point stays where it has been put, otherwise it will randomly be sorted to another position and the procedure is repeated for this point. This procedure is repeated until all the original points are in the final matrix, which will be printed as a stream file. This process is schematically shown in Figure 89. Since the algorithm contains a smart approach concerning the patterning history we named the strategy Smart InterLacing: **SIL**.

For the conversion of a bitmap into a smart interlacing stream file the input parameters that can be chosen by the user are:

- the bitmap file
- the magnification (needed for appropriate sizing)
- the interlacing distance
- the point pitch
- the dwell time corresponding to a blue value of 255 – all the other dwell times will be determined by linear interpolation
- the refresh time
- the critical radius

As an output two stream files are saved in the folder from which the program was started. The SIL stream file and a stream file containing the regular pattern in raster style for comparison.

For the conversion of already available stream files with any order (REG, IL, or others) the input parameters that can be chosen by the user are:

- the stream file
- the magnification (needed for appropriate sizing)
- the interlacing distance
- the refresh time
- the critical radius

In this case the output is only the SIL stream file, as the input file already represents the typical REG stream file.

The SIL-engine enables to interlace any stream file or bitmap and therefore allows a whole new prospect according the variety of applications for FIB structuring of soft matter.

Figure 90 shows a direct comparison of a transistor structure (top) and an inter-digital structure (bottom) once fabricated using REG patterning (left) and once using the SIL-engine. As it can be seen a dramatic improvement is clearly visible for a very critical PMMA sample. The structures on the left show blown up edges and a very uneven morphology at the ground, which makes these structures absolutely useless. Please note, the shown result is the best structure obtained after systematic variation of DT and PoP and therefore indicates the low performance of a classical REG approach. In contrast, the SIL patterned structure on the right shows a very flat morphology indicating the total absence of any creeping tendencies for this challenging SC material. Furthermore, the strongly improved morphological stabilities in terms of the absence of any blown up side wall and a still intact

central feature with less than 200 nm widths indicates the successful reduction of local temperatures due to proximity heating. The only remaining problem of the interlaced structures is that some little holes appear close to the edges. Currently a bachelor thesis is running at the FELMI which develops an edge proximity correction based on the results of this master thesis. The results clearly show that both proximity heating AND creeping effects can be avoided by using the SIL approach of a complex pattern.

With this selection of two demanding structures on a very challenging material (PMMA was practically considered not processible via FIB at all), it is clearly demonstrated how powerful the SIL approach is, which might open new possibilities for the structuring of critical materials.

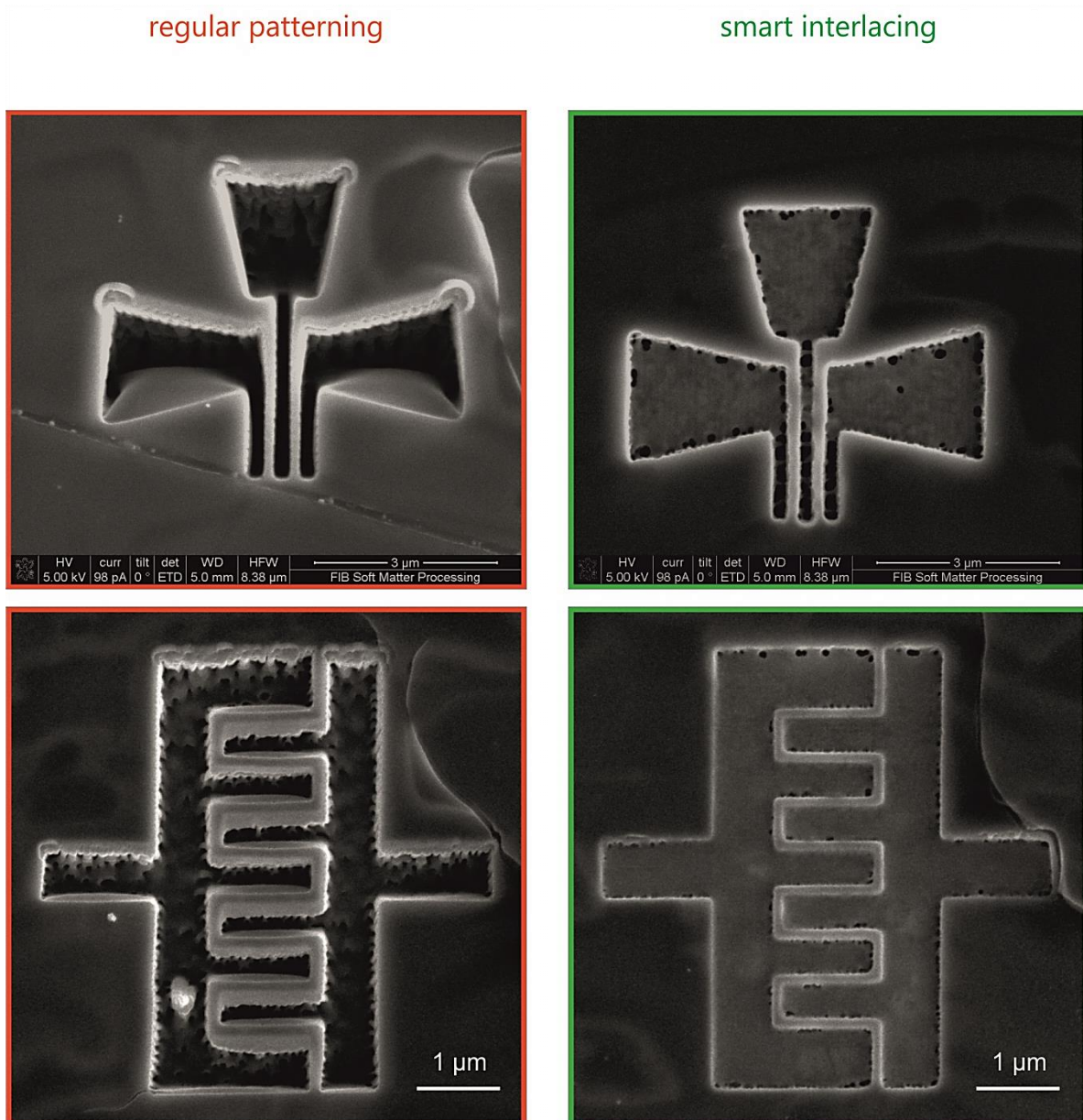


Figure 90: comparison of structures fabricated using regular patterning (left) and an interlaced stream file from the SIL-engine (right)

What gives the SIL engine its innovative character, is the fact that it enables the application of the SIL approach in combination with ANY stream file or bitmap file. The SIL approach strongly improves the

chemical and morphological stability even of very critical materials, as has been shown in this master thesis, and therefore enables the structuring of extremely critical materials in the first place. Therefore the SIL engine represents one of the first steps towards the use of the focused ion beam microscope for soft matter applications. It is now conceivable that in future the dual beam microscope with its versatile functionalities as an analysis or prototyping tool or as an instrument for TEM lamella preparation can also be used in combination with soft matter.

5 Summary and Outlook

The main goal of this master thesis was the correlation between material properties of different polymers and process parameters during focused ion beam (FIB) processing. The basis of this study was the successful introduction of an alternative patterning procedure for the reduction of local thermal stress: the interlacing (IL) strategy [15].

At the beginning of this thesis there was the reasonable assumption that the temperature induced effects during FIB processing are correlated to thermodynamic polymer properties in terms of melting points and / or volatilizing thresholds. The latter reflects that local temperatures are so high that polymer chains are decomposed in very short fragments, which can then volatilize. This is accompanied by the total loss of the pristine functionality of the polymer which often represents a knock-out criterion for FIB processes in combination with such low melting materials.

The study started with two classes of polymers, according to the degradation mechanism upon exposure to high temperatures: 1) cross-linking (CL) materials which form a rigid network; and 2) scissioning (SC) polymers which depropagate by a continuous loss of chemical bonds. Different polymers of both classes have been investigated with poly(methyl methacrylate) (PMMA) and high density polyethylene (HDPE) as strong representatives of SC and CL materials, respectively.

The first systematic FIB process parameter variation for regular and IL patterning strategies confirmed the massive reduction of local temperatures even for critical polymers such as PMMA and HDPE. Furthermore, the strongly improved chemical stability could be shown for IL strategies which revealed even better results compared to regular FIB processing at cryogenic temperature of -150 °C.

However, the results of those detailed and time intensive experiments did not show the expected correlation with the melting points and in particular with the volatilizing thresholds. Hence, it was obvious that another effect is strongly involved.

Therefore a closer look was taken at the obtained morphologies in dependency on the polymer classes (CL and SC). In particular, it was found that cross-linking materials show high morphological stabilities while scissioning polymers revealed special structures under certain conditions, which strongly reminded of liquid-like behaviour.

Based on these findings a hypothesis was deduced which predicts a mobile creeping phase for SC polymers as a result of the generation of smaller and smaller fragments during ion beam exposures which then become increasingly mobile. Furthermore, it was suggested that such a mobile material follows the ion beam movement as a result of high mobilities in combination with increased temperatures in the proximity of the moving ion beam.

Special experiments have been designed which could indeed prove a mobile phase which follows the ion beam during regular patterning strategies. The experiments have been supported by finite element and Monte Carlo simulations which revealed a temperature residue at areas where the mobile phase has been observed.

Detailed chemical analyses furthermore revealed the expected degradation behaviour for cross-linking and scissioning polymers during FIB processing from a chemical point of view.

The conclusions from these findings were that a simple interlacing approach, as introduced before, might be successful for some polymers but questionable for very challenging scissioning polymers.

Hence, a new interlacing strategy has been proposed which takes into account the unwanted heating effects during regular patterning but also the creeping phase and in particular the tendencies to follow the moving ion beam. In more detail, the improved strategy involves the patterning history in much more detail including thermodynamic peculiarities. Due to this self-adapting character we named this strategy Smart InterLacing: the SIL engine. Another advantage is that the smart approach allows the processing of any desired pattern, independent of its shape or size which was not possible with the original interlacing strategy.

In conclusion we have shown that FIB processing of soft materials depends not only on thermodynamic quantities which determine the total removal rates, but even stronger on chemical effects triggered by high temperatures. The knowledge about these effects allowed the specific adaption of the patterning strategy in two aspects: 1) local temperatures are strongly reduced, approaching the intrinsic (and unavoidable) temperatures caused by ion-matter single pulses; and 2) material related creeping effects reflecting the ion beam movement can be completely eliminated. This new strategy can be applied to any desired structure shape and is called Smart Interlacing or shortly the SIL engine.

As can be seen in Figure 91 by a direct comparison between regular patterns (left) and the SIL engine (right) the findings of this thesis might open new paths for FIB assisted structuring of even challenging materials like polymers or biomaterials.

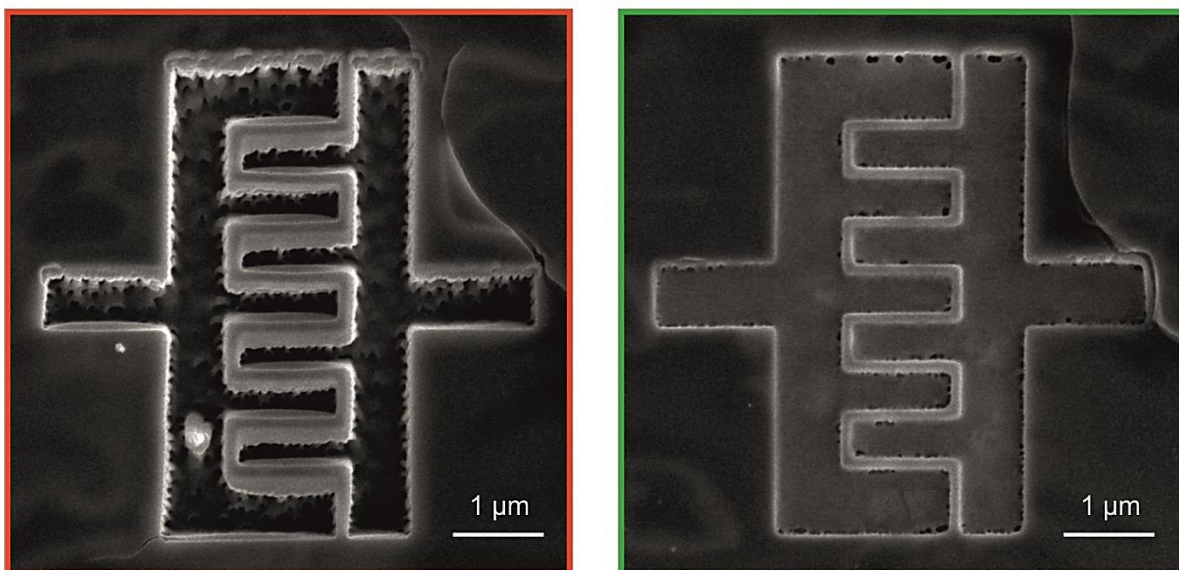


Figure 91: effect of smart interlacing (SIL) strategies on a scissioning polymer: while standard patterning is absolutely inadequate for such challenging materials (left), the SIL engine enables results with strongly improved morphologies (right) as well as increased chemical stabilities during FIB processing.

Follow up studies to this work have already been started at the FELMI and focus on an edge proximity correction to compensate for the final problems defined by pinhole formation at the side walls. Afterwards, the results will be used to improve the FIB based processing ranging from (3D) metrology of low melting materials (polymers, biomaterials, ...) over improved fabrication of ultrathin

TEM lamellas from critical samples towards innovative prototyping on biomaterials for the fabrication of functional (nano)structures or active devices such as sensors for gases and / or liquids.

6 Appendix

6.1 Appendix 1 - Matlab Code of the SIL-Engine - Bitmap Version

```

%SIL - Engine
%Angelina Orthacker
%Bitmap Version

% User info:
%1) The interlacing distance is supposed to be a multiple of the point
%   pitch.
%2) The minimum distance of 2 points for the refresh time calculations must
%   not be larger than half of the interlacing distance

clear all
close all

%get the data and all important parameters
file=uigetfile('*.bmp');
Mfile= imread(file);
Mf=Mfile(:,:,3);
[x,y]=find(Mf);

Mf_ind=sub2ind(size(Mf),x,y);
dt1=Mf(Mf_ind);

w=input('Please enter the dwell time corresponding to blue=255 in µs: ');
mag=input('Please enter the magnification in the small quadrant: ');
ild=input('Please enter the preferred interlacing distance in nm: ');
rtmin=input('Please enter the minimum refresh time in µs: ');
ild2=input('Please enter the minimum distance of two points for the refresh
time calc. in nm: ');
pop=input('Please enter the point pitch in nm: ');

dt1=double(dt1);
dt=dt1.*w./255;
dt=round(dt);
M=[dt,x,y]; %Matrix of dwell times and coordinates
M=double(M);

% sorting (so that the final positions are independent of the positions in
the original stream file)

[y2, iny]=sort(y);
x2=x(iny);
dt2=dt(iny);

[x3, inx]=sort(x2);
y3=y2(inx);
dt3=dt2(inx);

x=x3;
y=y3;

```

```

dt=dt3;
%end of sorting

lm=length(M);
mx=max(x);
my=max(y);

%finding the pixel distance
npix=65536;
pdx=97500000/mag/npix;

%finding the correct coordinates for the PoP
pf=round(pop./pdx);
xtest=x.*pf;
ytest=y.*pf;

if any([xtest;ytest])>65536, disp('Error: The pattern exceeds the maximum
number of pixels. Please choose a smaller point pitch or magnification.');
```

end

```

%data for regular file
Malt=[10.*dt,y.*pf,x.*pf];

%finding the interlacing number
iln=round(ild/pdx/pf); %/pf: to ensure the correct interlacing distance,
because the coordinates are multiplied with pf in the end

%% interlacing
Mxm=mod(x,iln);
Mym=mod(y,iln);

mv=zeros(size(M));
mv=[mv;0,0,0];
mvalt=mv;

mvt=mv;

count2=1;
count3=1;
sdt=rtmin+1;

% This loop sorts the matrix so that it is interlaced.
% It also checks whether from one frame to the next the refresh time
% condition is fulfilled. If not, every single point is checked.
% Points that don't fulfill the condition are cut out of the matrix and
% written in a spare matrix. The following points are shifted up, so that
% no empty lines are in the matrix.

for k=0:iln-1
    for l=0:iln-1
        ax=Mxm==l;
        ay=Mym==k;
        am=ax.*ay; %logical matrix representing the current interlacing frame

        v=dt(logical(am));
```

```

vx=x(logical(am));
vy=y(logical(am));

count=count2;
count2=count2+sum(logical((v)));

mv1=[v,vx,vy];
mv2=mv1(logical(v),:);

%test interlacing matrix
mvt(count:count2-1,:)=mv2; %new interlaced matrix

%%distance check

v1=length(mv2(:,1));
ind=count-1;

if sdt<rtmin, %check whether refresh time is fulfilled by last frame
for n=1:v1
    ind=ind+1;
    xrt=mvt(logical(flipud(cumsum(flipud(mvt(1:ind-1,1)))<rtmin)),2);
%coordinates of points which have been patterned within the refresh time
    yrt=mvt(logical(flipud(cumsum(flipud(mvt(1:ind-1,1)))<rtmin)),3);
%coordinates of points which have been patterned within the refresh time

    d=sqrt((mvt(ind,2)-xrt).^2+(mvt(ind,3)-yrt).^2).*pdx; % distance
of points which have been patterned within the refresh time and point to
pattern

    if any(d<=ild2) % check whether any of the points to pattern is
within the critical radius
        mvalt(count3,:)=mvt(ind,:); % write point to pattern in
alternative matrix
        mvt(ind:count2-1,:)=mvt(ind+1:count2,:); %eliminate point from
interlaced matrix and shift following points up
        count3=count3+1;
        count2=count2-1;
        ind=ind-1;

    end

end

end

end

sdt=sum(mvt(count:count2-1,1)); % sum over dts of the frame

end
end

lmvalt=sum(logical(mvalt(:,1)));
lmvt=sum(logical(mvt(:,1)));

```

```

% extra dt after last point, so that the point can also be sorted in at
% the end
mvt(lmvt+1,:)=[rtmin+1,100000,100000];

%% reintroducing points that have been sorted out

%this loop randomly chooses a new position for each of the points in the
%spare matrix. For every point it checks whether the refresh time
%condition is fulfilled for points patterned before and afterwards. This
%processes will be repeated until a suitable position is found for the
%point in question. Then it is performed for the next point.

    for n=1:lmvalt

        d=0;
        while any(d<=ild2)
            r=ceil(rand(1)*(lmvt+1)); %random numbers for sorting

            xrt=mvt(logical(flipud(cumsum(flipud(mvt(1:r-1,1)))<rtmin)),2);
            %coordinates of points which have been patterned within refresh time
            yrt=mvt(logical(flipud(cumsum(flipud(mvt(1:r-1,1)))<rtmin)),3);
            %coordinates of points which have been patterned within refresh time

            xrt2=mvt(logical(flipud(cumsum(mvt(r:lmvt+1,1))<rtmin)),2);%coordinates of
            points which will be patterned within refresh time

            yrt2=mvt(logical(flipud(cumsum(mvt(r:lmvt+1,1))<rtmin)),3);%coordinates of
            points which will be patterned within refresh time

            d1=sqrt((mvalt(n,2)-xrt).^2+(mvalt(n,3)-yrt).^2); % distance of
            points which have been patterned within refresh time and point to pattern
            d2=sqrt((mvalt(n,2)-xrt2).^2+(mvalt(n,3)-yrt2).^2); % distance of
            points which have been patterned within refresh time and point to pattern
            d=[d1;d2].*pdx;

        end
        mvt(r+1:lmvt+2,:)=mvt(r:lmvt+1,:);
        mvt(r,:)=mvalt(n,:);
        lmvt=lmvt+1;

    end
    % end reintroducing points that have been sorted out

    %now the smartly interlaced matrix is finished.

%% preparation of output and output
    mv=mvt(1:end-1,:);
    mvx=mv(:,3);
    mvy=mv(:,2);
    mv(:,2)=mvx.*pf;
    mv(:,3)=mvy.*pf;
    mv(:,1)=mv(:,1).*10;

    figure(1)

```

```

plot(mv(:,2),-mv(:,3),'.')
figure(2)
plot(Malt(:,2),-Malt(:,3),'.')

%output
mv=mv.';
Malt=Malt.';

Mt1='s';
Mt2=1;
Mt3=length(mv);

fid = fopen('newfile.str','w');
fprintf(fid,'%s16 \r\n', Mt1);
fprintf(fid,'%i \r\n', Mt2);
fprintf(fid,'%i \r\n', Mt3);
fprintf(fid,'%i %i %i \r\n',mv);
fclose(fid);

fid2 = fopen('regfile.str','w');
fprintf(fid2,'%s16 \r\n', Mt1);
fprintf(fid2,'%i \r\n', Mt2);
fprintf(fid2,'%i \r\n', Mt3);
fprintf(fid2,'%i %i %i \r\n',Malt);
fclose(fid2);

```

6.2 Appendix 2 - Matlab Code of the SIL-Engine - Stream File Version

```

%SIL - Engine
%Angelina Orthacker
%Stream File Version

% User information:
%1) The interlacing distance is supposed to be a multiple of the point
%   pitch.
%2) The minimum distance of 2 points for the refresh time calculations must
%   not be larger than half of the interlacing distance

clear all
close all

file=uigetfile('*.str');
Mfile= importdata(file, ' ', 3);
M=Mfile.data;
sp=M(1,:);
ep=M(end,:);
M=M(2:end-1,:);

mag=input('Please enter the magnification in the small quadrant: ');
ild=input('Please enter the preferred interlacing distance in nm: ');
rtmin=input('Please enter the minimum refresh time in µs: ');
ild2=input('Please enter the minimum distance of two points for the refresh
time calc. in nm: ');

```

```

dt=M(:,1);
x=M(:,2);
y=M(:,3);

%sorting (so that the final positions are independent of the positions in
the original stream file)
[x2, inx]=sort(x);
y2=y(inx);
dt2=dt(inx);

[y3, iny]=sort(y2);
x3=x2(iny);
dt3=dt2(iny);

x=x3;
y=y3;
dt=dt3;
%end of sorting

lm=length(M);
mx=max(x);
my=max(y);

%finding the pixel distance
npix=65536;
pdx=97500000/mag/npix;

%finding the interlacing number
iln=round(ild/pdx);

% interlacing
Mxm=mod(x,iln);
Mym=mod(y,iln);

% This part was introduced to increase the speed of the program. It makes
% sure that the double loop that creates the interlacing pattern does not
% run through empty loops.
b=0:iln-1;
bx=zeros(size(b));
by=bx;

for kb=b
    bx(kb+1)=any(Mxm==kb) .* (kb+1);
end
bx=bx(logical(bx))-1;

for kb=b
    by(kb+1)=any(Mym==kb) .* (kb+1);
end
by=by(logical(by))-1;

%end of part for increasing speed

mv=zeros(size(M));
mv=[mv;0,0,0]; % for the DT-check with random
mvalt=mv;

```

```

sdt=rtmin+1; %for the first loop.
count2=1;
count3=1;

% This loop sorts the matrix so that it is interlaced.
% It also checks whether from one frame to the next the refresh time
% condition is fulfilled. If not, every single point is checked.
% Points that don't fulfill the condition are cut out of the matrix and
% written in a spare matrix. The following points are shifted up, so that
% no empty lines are in the matrix.

for k=by
    for l=bx
        ax=Mxm==l;
        ay=Mym==k;
        am=ax.*ay; %logical matrix representing the current interlacing frame

        v=dt(logical(am));
        vx=x(logical(am));
        vy=y(logical(am));

        count=count2;
        count2=count2+sum(logical((v)));

        mv1=[v,vx,vy];
        mv2=mv1(logical(v),:);

        %test interlacing matrix
        mvt=mv;
        mvt(count:count2-1,:)=mv2;

        %distance check

        vl=length(mv2(:,1));
        ind=count-1;
        if sdt<rtmin, %check whether refresh time is fulfilled by last frame
            for n=1:vl
                ind=ind+1;
                xrt=mvt(logical(flipud(cumsum(flipud(mvt(1:ind-
1,1)))./10<rtmin)),2); %coordinates of points which have been patterned
within the refresh time
                yrt=mvt(logical(flipud(cumsum(flipud(mvt(1:ind-
1,1)))./10<rtmin)),3); %coordinates of points which have been patterned
within the refresh time

                d=sqrt((mvt(ind,2)-xrt).^2+(mvt(ind,3)-yrt).^2).*pdx; % distance
of points which have been patterned within the refresh time and point to
pattern

                if any(d<=ild2), % check whether any of the points to pattern is
within their critical radius
                    mvalt(count3,:)=mvt(ind,:); % write point to pattern in
alternative matrix
                    mvt(ind:count2-1,:)=mvt(ind+1:count2,:);%eliminate point from
interlaced matrix and shift following points up
                    count3=count3+1;

```

```

        count2=count2-1;
        ind=ind-1;

    end

end

end

    sdt=sum(mvt(count:count2-1,1)); % sum over dts of the frame
    mv=mvt;

end

end

lmvalt=sum(logical(mvalt(:,1)));
lmvt=sum(logical(mvt(:,1)));
% extra dt after last point, so that the point can also be sorted in at
% the end
mvt(lmvt+1,:)= [rtmin+1,100000,100000];

%% reintroducing points that have been sorted out

%This loop randomly chooses a new position for each of the points in the
%spare matrix. For every point it checks whether the refresh time
%condition is fulfilled for points patterned before and afterwards. This
%processes will be repeated until a suitable position is found for the
%point in question. Then it is performed for the next point.

    for n=1:lmvalt

        d=0;
        while any(d<=ild2)
            r=ceil(rand(1)*(lmvt+1)); %random numbers for sorting

            xrt=mvt(logical(flipud(cumsum(flipud(mvt(1:r-
1,1)))./10<rtmin)),2); %coordinates of points which have been patterned
within refresh time
            yrt=mvt(logical(flipud(cumsum(flipud(mvt(1:r-
1,1)))./10<rtmin)),3); %coordinates of points which have been patterned
within refresh time

            xrt2=mvt(logical(flipud(cumsum(mvt(r:lmvt+1,1))./10<rtmin)),2);
%coordinates of points which have been patterned within refresh time
            yrt2=mvt(logical(flipud(cumsum(mvt(r:lmvt+1,1))./10<rtmin)),3);
%coordinates of points which have been patterned within refresh time

            d1=sqrt((mvalt(n,2)-xrt).^2+(mvalt(n,3)-yrt).^2);% distance of
points which have been patterned within refresh time and point to pattern
            d2=sqrt((mvalt(n,2)-xrt2).^2+(mvalt(n,3)-yrt2).^2);% distance of
points which have been patterned within refresh time and point to pattern
            d=[d1;d2].*pdx;

        end

        mvt(r+1:lmvt+1,:)=mvt(r:lmvt,:);

```

```
mvt(r,:) = mvalt(n,:);
lmvt = lmvt + 1;

end

% end reintroducing points that have been sorted out

% now the smartly interlaced matrix is finished.
%% preparation of output and output
mv = mvt(1:end-1,:);

figure
plot(mv(:,2), -mv(:,3), 'r.')

%output
mv = mv.';
sp = sp.';
ep = ep.';

Mt = char(Mfile.textdata);
Mt1 = Mt(1);
Mt2 = str2double(Mt(2));
Mt3 = str2double(Mt(3,:));

fid = fopen('newfile.str', 'w');
fprintf(fid, '%s \r\n', Mt1);
fprintf(fid, '%i \r\n', Mt2);
fprintf(fid, '%i \r\n', Mt3);
fprintf(fid, '%i %i %i \r\n', sp);
fprintf(fid, '%i %i %i \r\n', mv);
fprintf(fid, '%i %i %i \r\n', ep);
fclose(fid);
```

References

- [1] Courtesy of Dr. Harald Plank, Institute for Electron Microscopy and Nanoanalysis, Graz University of Technology, Austria, **2013**.
- [2] J. Mayer, L.A. Giannuzi, T. Kamino, J. Michael, *MRS Bulletin*, **2007**, 32, 400.
- [3] I. Utke, P. Hoffmann, J. Melngailis, *J. Vac. Sci. Technol. B*, **2008**, 26, 1197.
- [4] I. Utke, S. Moshkalev, P. Russel, *Nanofabrication using focused ion and focused electron beams*, Oxford series on nanomanufacturing, New York, **2012**.
- [5] M. Schaffer, J. Wagner, B. Schaffer, M. Schmied, H. Mulders, *Ultramicroscopy*, **2007**, 107, 8, 587; **ii)** M. Schaffer, H. Schröttner, J. Wagner, *Microscopy and Microanalysis*, **2008**, 14, 2, 2008, 982; **iii)** M. Schaffer, J. Wagner, *Microchimica Acta*, **2008**, 161, 3-4, 421.
- [6] L. Reimer, *Scanning Electron Microscopy*, Springer, **1998**.
- [7] J. Goldstein, *Scanning Electron Microscopy and X-Ray Analyses*, Springer, **2003**.
- [8] D. Drouin, A.R. Couture, D. Joly, C. Tastet, V. Aimez, R. Gauvin, *Scanning*, **2007**, 29, 402.
- [9] PdD Thesis by Dr. Meltem Sezen, Institute for Electron Microscopy and Nanoanalysis, Graz University of Technology, Austria, **2009**.
- [10] L.A. Giannuzi, F.A. Stevie, *Introduction to focused ion beams: instrumentation, theory, techniques, and practice*, Springer, New York, USA, **2005**.
- [11] J. Orloff, M. Utlaut, L. Swanson, *High Resolution Focused Ion Beams*, Kluwer Academic/Plenum Publishers, New York, **2002**.
- [12] FEI Company, The Netherlands.
- [13] C.A Volkert, A.M. Minor, *MRS Bulletin*, **2007**, 32, 389.
- [14] SRIM (Stopping and Range of Ions in Matter) software at www.srim.org
- [15] R. Schmied, B. Chernev, G. Trimmel, H. Plank, *RSC Advances*, **2012**, 2, 6932.
- [16] R. C. García, *Amplitude modulation atomic force microscopy*, Weinheim, Chichester: Wiley-VCH; John Wiley, **2010**.
- [17] A. Seidl, *Properties and Behavior of Polymers*, John Wiley and Sons, **2011**.
- [18] E.H. Lee, G.R. Rao, L.K. Mansur, *LET effect on cross-linking and scission mechanisms of PMMA during irradiation*, Radiation Physics and Chemistry, **1999**, 55, 293.
- [19] R. Clough, *High-energy radiation and polymers: A review of commercial processes and emerging applications*, Nuclear Instruments and Methods in Physics Research B, **2001**, 185, 8.

- [20] R. Jones, *Soft Condensed Matter*, Oxford University Press, **2002**.
- [21] S. Tamboli, S. Mhaske, D. Kahe, *Crosslinked Polyethylene*, Indian Journal of Chemical Technology, **2004**, 11, 853.
- [22] J. Mark, *Physical Properties of Polymers Handbook Second Edition*, Springer, **2007**.
- [23] www.alfa.com
- [24] A. French, A. Thompson, B. Davis, *High-Purity Discrete PEG-Oligomer Crystals Allow Structural Insight*, Angew. Chem. Int. Ed., **2009**, 48, 1248 .
- [25] W. Wanga, X. Yang, Y. Fang, J. Ding, J. Yan, *Preparation and thermal properties of polyethylene glycol/expanded graphite blends for energy storage*, Applied Energy, **2009**, 86, 1479.
- [26] www.dupont.com
- [27] M. Marín, A. Jiménez, J. López, J. Vilaplana, *Thermal Degradation of Ethylene (Vinyl Acetate) Kinetic analysis of thermogravimetric data*, Journal of Thermal Analysis, **1996**, 47, 247.
- [28] B. Lee¹, J. Z. Liu, B. Sun, C. Shen, G. Dai¹, *Thermally conductive and electrically insulating EVA composite encapsulants for solar photovoltaic (PV) cell*, EXPRESS Polymer Letters Vol.2, **2008**, 5, 357.
- [29] private communication with FEI
- [30] Matlab Software Release 2010b